Atomic-scale characterization and control of metal-organic templates and photosensitizers on surfaces

Thèse n° 5884 (2013)
présenté le 23 Juillet 2013
à la Faculté des Sciences de Base
Laboratoire de Science à l'Échelle Nanométrique
Programme Doctoral en Physique
École Polytechnique Fédérale de Lausanne

pour l'obtention du grade de Docteur ès Sciences
par

Christopher Seiji Kley

acceptée sur proposition du jury:

Prof. Romuald Houdré, président du jury
Prof. Klaus Kern, directeur de thèse
Prof. Anna Fontcuberta i Morral, rapporteur
Prof. Harold Zandvliet, rapporteur
Prof. James O'Shea, rapporteur

Lausanne, EPFL, 2013

To Judith

Abstract

Striving for the advancement of current solar energy converters such as dye-sensitized solar cells (DSSCs) as well as the development of novel heterogeneous catalysts for chemical energy conversion, this thesis focuses on three main objectives.

The first part of this thesis is dedicated to the design and construction of a new type of low-temperature scanning tunneling microscope (STM) which fulfills following criteria: (i) precise tip z-approach, (ii) lateral sample positioning with (sub-)micrometer precision, (iii) simple in-situ tip exchange, (iv) optical access for controlling the sample position and irradiating the sample with light, (v) multiple electrical sample access for in-situ transport and back-gate functionalities and (vi) use of versatile sampleholders for different substrates. The construction of additional system components as well as the STM wiring to a new liquid helium bath cryostat is described. In addition, the system performance properties are demonstrated.

In the second part of this thesis, the assembly of the rod-like 4,4'-di-(1,4-buta-1,3-diynyl)-benzoic acid (BDBA) and iron atoms into extended two-dimensional metal-organic coordination networks (MOCNs) on Au(111) and Ag(100) surfaces with insensitivity to intrinsic substrate defects is reported. Independent from the chosen substrate and its surface symmetry, the MOCNs grow continuously over multiple surface terraces through mutual inphase structure adaptation of network domains at step edges as well as on terraces. The adaptability of the MOCNs is mainly ascribed to the high degree of conformational flexibility of the butadiynyl functionality of the ligand. Despite their flexibility, the MOCNs exhibit considerable robustness against annealing at high temperatures. Furthermore, the interaction of nickel atoms and clusters with the butadiyne metal-organic templates on Au(111) and Ag(100) surfaces is investigated by means of STM. It is shown that nickel (Ni) atoms can be incorporated in the metal-organic matrix without loosing its structural integrity. The metal substrate plays a crucial role in the interaction of Ni atoms with the metal-organic host networks. On Au(111), Ni clusters are spatially limited to the network cavity size while decorating the phenyl rings. In contrast, on Ag(100) the metal-organic template imposes the nucleation of Ni atoms within the topmost substrate layer underneath the network pattern. In both cases, clusters consisting of a few metal atoms with an areal density of 4×10^{13} cm^{-2} can be obtained that are stable upon annealing up to 450 K. Additionally, the Ni decorated MOCNs can be utilized for binding additional molecular units into the network cavities.

The third part of this work is dedicated to the atomic-scale investigation of the structural and electronic properties of the photosensitizer N3 (cis-di(thiocyanato)-bis(2,2'-bipyridyl-4,4'-dicarboxylate) ruthenium(II)) and its anchoring ligand BINA (2,2'-bipyridyl-4,4'-dicarboxylic acid) on TiO_2 anatase (101). First, the preparation of atomically well-defined TiO_2 anatase surfaces using natural TiO_2 bulk crystals is reported. Subsequently, the in-situ N3 dye deposition via electrospray ion beam deposition is demonstrated. STM and STS studies in UHV at 5 K provides direct access to the molecule-substrate interface at the atomic level. The local structure of N3 molecules is probed with single molecule sensitivity revealing multi-conformational N3 binding geometries on the oxide surface. It is shown that the electronic properties of the N3 dye strongly depend on its adsorption geometry making specific dye adsorption geometries more favorable in terms of higher charge injection efficiencies. Furthermore, the STM studies reveal the formation of supramolecular N3 dye assemblies. The N3 studies are complemented with STM investigations of the N3 anchoring ligand BINA thermally evaporated on TiO_2 anatase (101). The observation of multiple adsorption configurations of the BINA ligand on the TiO_2 substrate is correlated to the multi-conformational N3 binding geometries. These experimental findings are supported by extensive density functional theory based calculations. Additionally, the N3 dye is resolved with submolecular resolution on Au(111). STS studies reveal vibronic modes supporting N3 coordination via its sulphur groups to the gold surface. Different possible N3 binding geometries are compared for both the TiO_2 oxide and metal surfaces.

Keywords *Scanning tunneling microscopy, scanning tunneling spectroscopy, molecular self-assembly, supramolecular architectures, multi-component systems, dye-sensitized solar cell, titanium dioxide, photosensitizer, electrospray ion beam deposition, density functional theory, ultra high vacuum*

Zusammenfassung

Der erste Schwerpunkt der vorliegenden Arbeit liegt in der Konstruktion eines Tieftemperatur-Rastertunnelmikroskops (RTMs), das folgende Systemanforderungen erfüllt: (i) präzise Spitzenannäherung, (ii) laterale, Sub-Mikrometer genaue Probenpositionierung, (iii) einfacher in-situ Spitzenwechsel, (iv) optischer Zugang zur Kontrolle der Probenposition und zur Lichteinkopplung, (v) mehrfacher elektrischer Probenkontakt für Transportmessungen sowie Back-Gate Anwendungen, (vi) variables Probenhalterdesign für unterschiedliche Substrate. Neben der Beschreibung des RTM-Aufbaus wird die Konstruktion zusätzlicher Systemkomponenten sowie die Verkabelung des RTMs an einen neuen Flüssig-Helium Kryostaten dargestellt. Im Anschluss werden die Systemeigenschaften spezifiziert.

Im zweiten Teil der Arbeit wird die Realisierung von ausgedehnten zwei-dimensionalen metall-organischen Netzwerken von stäbchenförmigen Liganden und Eisen Metallatomen auf Ag(100) und Au(111) Oberflächen mittels RTM untersucht. Die Netzwerke zeigen eine ungewöhnlich hohe Toleranz und Anpassungsfähigkeit gegenüber intrinsischen Substratdefekten und Stufenkanten sowie zwischen zusammenwachsenden Domänengrenzen. Dabei wachsen die Netzwerke kontinuierlich über Substratstufenkanten, ohne die Gitterstruktur zu unterbrechen. Die wechselseitige Anpassung von Netzwerkdomänen an den Stufenkanten sowie auf Oberflächenterassen wird auf die Alkynylgruppe im Liganden zurückgeführt. Diese gestattet die Einnahme vieler verschiedener Adsorptionsgeometrien des Liganden sowie die Verbiegung des linearen Moleküls für die Bildung der energetisch bevorzugten Fe-Carboxylat Bindungen. Trotz dieser Eigenschaften sind die Netzwerke bis zu einer Temperatur von 450 K thermisch robust. Die Ergebnisse zeigen das Potential von metall-organischen Verbindungen, mesoskalig geordnete Netzwerke auf Oberflächen zu bilden, ohne durch intrinsische Defekte limitiert zu sein. Desweiteren wurden die Netzwerke auf Au(111) und Ag(100) als Templat für die Einbindung von Ni Atomen verwendet. Die Ni Atome können in die Netzwerke integriert werden, ohne deren strukturelle Integrität zu beeinträchtigen. Das Substrat spielt dabei eine entscheidende Rolle. Im Falle von Au(111) werden die Benzengruppen dekoriert, während auf der Ag(100) Oberfläche Ni an die Butadiynylgruppe bindet. Auf Au(111) sind die Clustergrössen durch die Grösse der Kavitäten des Netzwerkes limitiert. Auf

Ag(100) wachsen zudem Ni Cluster unterhalb des Netzwerkes und innerhalb der ersten Silber-Substratschicht. Auf diese Weise erhält man eine hohe Dichte von kleinen Clustern mit einer sehr hohen thermischen Stabilität bis mindestens 450 K. Zusätzlich bilden die Ni Atome in den Netzwerkkavitäten Andockstellen für die Einbindung weiterer molekularer Einheiten. Dies ermöglicht die gezielte Synthese hierarchisch aufgebauter Multikomponentensysteme auf Oberflächen.

Der dritte Schwerpunkt dieser Arbeit liegt in der Untersuchung der geometrischen und elektronischen Eigenschaften des Farbstoffsensibilisators N3 (cis-di(thiocyanato)-bis(2,2'-bipyridyl-4,4'-dicarboxyl) Ruthenium(II)) sowie des Farbstoffliganden BINA (2,2'-bipyridyl-4,4'-dicarboxyl Säure) auf TiO_2 Anatase (101). Zu Beginn wird die Präparation atomar reiner TiO_2 Anatase Oberflächen unter Verwendung natürlich gewachsener TiO_2 Kristalle beschrieben. Daraufhin wird die Deposition des N3 Farbstoffes mittels Elektrospray Ionisierung (ESI) demonstriert. RTM und Rastertunnelspektroskopie (RTS) Studien in Ultrahochvakuum bei 5 Kelvin ermöglichen die Untersuchung der lokalen elektronischen Struktur der N3 Moleküle auf molekularer Ebene. Es wird gezeigt, dass die N3 Moleküle in verschiedenen Konformationen auf dem Substrat adsorbieren und die elektronischen Eigenschaften des N3 Farbstoffes sehr stark von seiner entsprechenden Adsorptionsgeometrie abhängen. Spezifische Adsorptionsgeometrien können dabei höhere Ladungsträgerinjektionsraten begünstigen. Desweiteren wird die Ausbildung supramolekularer N3 Farbstoff Aggregate gezeigt. Ergänzt werden die Studien am Farbstoff N3 durch RTM Untersuchungen des Farbstoffliganden BINA, der durch Sublimation auf TiO_2 Anatase (101) aufgebracht wurde. Die Beobachtung verschiedener BINA Adsorptionsgeometrien auf dem TiO_2 Substrat wird mit den multi-konformalen Bindungsgeometrien der N3 Moleküle in einen Zusammenhang gebracht. Die experimentellen Ergebnisse werden mittels auf Dichtefunktionaltheorie basierenden Methoden simuliert. Zusätzlich wird der Farbstoff N3 auf Au(111) auf seine geometrischen und elektronischen Eigenschaften hin untersucht. RTS Studien zeigen vibronische Moden in den entsprechen Tunnelspektren, was auf eine Anbindung der N3 Moleküle über deren Schwefelgruppen auf die Goldoberfläche hindeutet. Im Anschluss werden die verschiedenen N3 Bindungsgeometrien für die beiden Substrate TiO_2 Anatase (101) und Au(111) verglichen.

Schlüsselwörter *Rastertunnelmikroskopie, Rastertunnelspektroskopie, molekulare Selbstassemblierung, supramolekulare Anordnungen, Multi-Komponenten Systeme, Farbstoffsensibilisierte Solarzellen, Titandioxid, Farbstoffsensibilisator, Elektrospray Ionenstrahl Deposition, Dichtefunktionaltheorie, Ultrahochvakuum.*

Abbreviations

ATR-FTIR	Attenuated Total Reflectance Fourier Transform Infrared Spectroscopy
BDBA	4,4'-di-(1,4-buta-1,3-diynyl)-benzoic acid
BINA	2,2'-bipyridyl-4,4'-dicarboxylic acid
DFT	Density Functional Theory
DSSC	Dye-Sensitized Solar Cell
ES-IBD	Electrospray Ion Beam Deposition
ES	Electrospray
HOMO	Highest Occupied Molecular Orbital
LDOS	Local Density Of States
LUMO	Lowest Unoccupied Molecular Orbital
MMO	Methane monooxygenase
MOCN	Metal-Organic Coordination Network
MOF	Metal-Organic Frameworks
N3	Cis-di(thiocyanato)-bis(2,2'-bipyridyl-4,4'-dicarboxylate) ruthenium(II) complex
NEXAFS	Near-Edge X-ray Absorption Fine Structure
RF	Radio Frequency
RKKY	Ruderman-Kittel-Kasuya-Yosida
SCID	Soft Cluster-Induced Desorption
STM	Scanning Tunneling Microscopy
STS	Scanning Tunneling Spectroscopy
TiO_2	Titanium Dioxide
TOF	Time-Of-Flight
UHV	Ultra High Vacuum
XAS	X-ray Absorption Spectroscopy
XPS	X-ray Photoelectron Spectroscopy
XRD	X-Ray Diffraction
2D	Two-Dimensional

Contents

Introduction

Nanotechnology literally comprises any technology on a nanometer scale that has applications in the macroscopic world. It encompasses the production and application of physical, chemical, and biological systems at dimensions ranging from individual atoms or molecules to submicron sizes, as well as the integration of the resulting nanostructures into larger systems. Science and engineering in nanotechnology promises breakthroughs in areas such as advanced materials and manufacturing, sustainable energy, medicine, biotechnology and information technology. Over the last decade, a highly interdisciplinary field has evolved where a clear-cut line between the classical disciplines of science cannot be drawn anymore. Among these various disciplines, surface science assumed an outstanding role. Particularly in the fields of catalysis and solar-energy converters, numerous fundamental processes can only be understood by investigating interfacial processes and properties at the atomic level. A major breakthrough that contributed to the rapid evolution of surface science was the invention of scanning tunneling microscopy (STM) in 1981 by Binnig and Rohrer.[1,2] Nowadays, the STM technique emerged to a key tool in nanoscale science since it provides a unique spatial resolution of (semi-)conductive surfaces at the air, vacuum or liquid interface. Furthermore, detailed chemical and electronic information can be obtained by spectroscopic methods.[3,4] So far, numerous studies have demonstrated the diverse applications of the STM technique which resulted for example in the exploration of local electronic properties of atoms,[5] collective electronic behaviour on surfaces,[6–9] geometry of molecular organizations and supramolecular assemblies,[10–14] chiral agglomerations,[15–17] local magnetic properties,[18,19] pathways of chemical reactions[20–22] and catalytic functionality.[23]

In surface science, the continuous advancement of characterization tools is of paramount importance to stay at the forefront of investigating distinguished materials and interfaces at the atomic level. As described in the following, particularly titanium dioxide emerged over the last decade as a highly promising material with diverse applications in important technological areas. Striving for the investigation of nanoscale phenomena at the molecule-oxide interface of dye-sensitized solar cells (DSSCs) inherently necessitated the first integral part of this thesis: the design and construction of a new type of low-temperature STM. Based on this STM, two main research directions were followed in the present work: (i) fabrication and characterization of extended metal-organic coordination networks (MOCNs) on metal surfaces with insensitivity to intrinsic substrate defects as well as its functionalization by catalytic active metal atoms and (ii) atomic-scale investigation of the structural and electronic properties of the photosensitizer N3 (cis-di(thiocyanato)-bis(2,2'-bipyridyl-4,4'-dicarboxylate) ruthenium(II))[24] and its anchoring ligand BINA (2,2'-bipyridyl-4,4'-dicarboxylic acid) adsorbed on TiO_2 anatase (101).

The first research direction of this thesis aims at the realization of extended and catalytically active two dimensional (2D) MOCNs. In supramolecular chemistry, complex functional structures and components as ubiquitously found in nature can be created by a hierarchical assembly scheme.[25,26] A large entity is composed of smaller, relatively simple units assembled by a self-directed and hierarchical order of specific interactions between the different subunits. Creating complex structures out of smaller units is a formidable reverse engineering problem that requires the detailed knowledge of the involved processes and interactions. Over the last years, surface-confined MOCNs have demonstrated great potential for diverse applications.[27] Molecular networks assembled on surfaces[28] were tested for their suitability to serve as host-guest systems[29] and as templates to steer the adsorption and organization of secondary ligands[30] and metal atoms.[31,32] Specific functions and properties can be introduced to these networks in two steps. First, a robust network is constructed featuring suitable lattice structure, porosity and well-defined anchoring sites. In the second step, functional units such as catalytic active metal centers or secondary ligand molecules are incorporated at a higher organizational stage.[33,34] This bottom-up approach allows much higher feature densities compared to classical top-down nanostructuring methods. A particular and unique feature of the 2D-MOCNs is the presence of low-coordinated metal centers offering multiple functional properties which depend on the specific coordination environment. In a variety of natural enzymes, metal ions such as iron, nickel and manganese embedded in organic structures of proteins form catalytically active centers which perform important biological conversion processes.[35] Figure 0.1 shows a high-resolution STM image of a 2D-MOCN consisting of iron atoms and the rod-like ligand BDBA (4,4'-di-(1,4-buta-1,3-diynyl)-benzoic acid) on Au(111) (see Chapter 3). As indicated, the coordinatively unsaturated di-iron metal centers in the MOCN strongly resemble the reaction centers of natural enzymes such as the methane monooxygenase which is capable of oxydizing C-H bonds in alkanes and

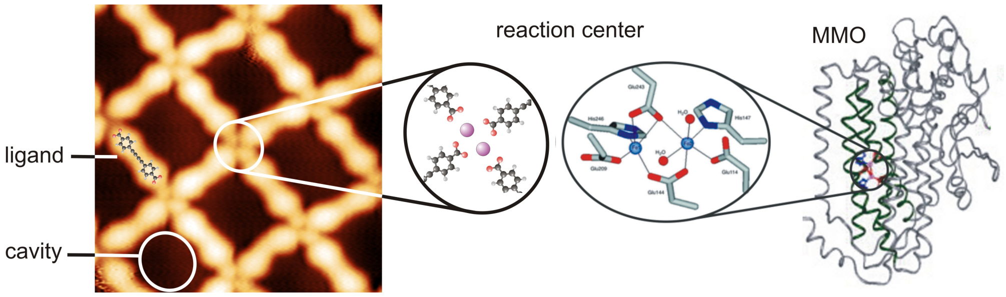

Figure 0.1: STM image of a two-dimensional metal organic coordination network consisting of iron atoms and the rod-like ligand BDBA (4,4'-di-(1,4-buta-1,3-diynyl)-benzoic acid) on Au(111). The network is characterized by the organic ligand, the cavities and the di-iron binding motif. The coordinatively unsaturated metal centers strongly resemble natural enzymes such as the methane monooxygenase (MMO) which is capable of oxydizing C-H bonds in alkanes and activating oxygen.

activating oxygen.[36,37] This similarity between low-coordinated metal centers in 2D-MOCNs and catalytically active sites in biological systems makes MOCNs attractive candidates for realizing functional catalytic structures. One basic requirement for the realization of multicomponent systems is the design of stable and mesoscale primary network structures. The network formation strongly depends on the intermolecular forces and competes with the coupling and constraints imposed by the supporting surface. Over the last decade, phenomena like error-correction, self-selection and read-out of pre-programmed molecular interactions have been studied in multicomponent MOCN systems on surfaces.[30,38,39] However, the realization of such MOCNs was spatially limited by intrinsic surface defects, e.g. step edges and dislocations, as well as by the strong interaction of the adlayer components with the underlying support. Achieving procedures to pattern also rough and imperfect surfaces would be greatly beneficial for the realization of mesoscale and robust MOCNs. Furthermore, there are still plenty of open questions concerning the catalytic functionalization of such MOCNs which need to be adressed when striving for bioinspired heterogenous catalysts for chemical energy conversion.

The second research direction of this thesis represents the atomic-scale investigation of the structural and electronic properties of the photosensitizer N3 and its anchoring ligand BINA adsorbed on TiO_2 anatase (101). These days, oxide surfaces have emerged as one of the most fascinating materials. Particularly, the low-cost and widely available titanium dioxide (TiO_2) represents one of the most studied metal oxides. It constitutes a promising material with versatile applications in important technological areas[41–43] ranging from (photo)catalysis,[44–51] gas sensors,[52,53] coatings,[54–56] batteries,[43,57] to air purification[54,58] and degradation of environmental pollutants.[59,60] Moreover, TiO_2 plays a crucial role in a number of electrochemical devices for solar energy conversion, particularly in dye-sensitized solar cells.[60–67] Since the first report of a 7 % efficient cell in 1991, DSSCs have received a tremendous amount of attention and emerged as a new class of solar conversion devices. Confirmed record efficiencies are now 11.2 % for small cells and 9.9 % for submodules, and low-cost production methods enable manufacturing of DSSCs for a variety of possible applications. DSSCs possess a number of advantages compared to present c-Si, CdTe, and CIGS devices, even though these other technologies have higher cell and module efficiencies (see Figure 0.2). DSSCs can be manufactured using roll-to-roll processing without vacuum or high temperature resulting in low embodied energy with expected energy payback periods of less than one year. DSSCs can be made light in weight and flexible by deposition on plastic substrates or metal foils. They contain primarily nontoxic, earth-abundant materials and exhibit considerable performance in diverse lighting conditions including high angle of incidence, low light intensity and partial shadowing which makes them also potential candidates for building-integrated applications. Given this high number of advantages - which factors hinder DSSCs from providing already today a technically and economically viable alternative to present day pn-junction photovoltaic devices?

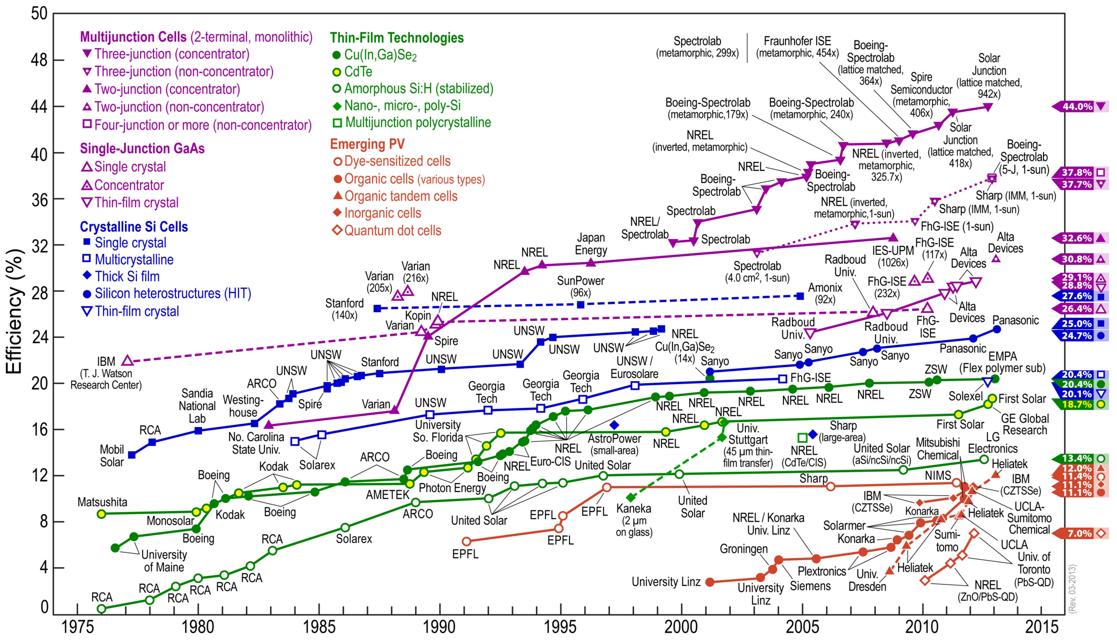

Figure 0.2: Laboratory best cell conversion efficiencies for various photovoltaic technologies over the past four decades. Despite a general upward trend, major breakthroughs in the efficiency of dye-sensitized solar cells are still necessary for making these devices a viable alternative to present day pn-junction photovoltaic cells. (Image source: NREL[40])

In comparison to its inorganic competitors, DSSCs still lack efficiency and lifetime that are significantly lower compared to c-Si and CdTe devices (see Figure 0.2). Hence, the most direct competitor at present are amorphous Si cells for low-cost and low-power markets. The great challenge now lies in finding materials, module architectures, and manufacturing processes that provide optimal combinations of high efficiency, long term stability, and low cost. Each of these criteria presents different scientific and engineering challenges. From the perspective of engineering, efficient ways must be found especially for robust high-throughput manufacturing methods and extremely well sealed cell structures to prevent electrolyte leakage and moisture ingress.

The other great challenge constitutes the development of new photosensitizers, redox couples and photoanodes. However, breakthroughs in increasing DSSC efficiencies are primarily hindered by a deficient understanding of the fundamental processes which occur at the molecular level in DSSCs. These devices consist of a mesoporous TiO_2 layer on a transparent conducting glass coated with a charge-transfer dye to sensitize the film for light harvesting. The key processes in DSSCs comprise: (i) photoexcitation of the dye followed by (ii) electron injection into the conduction band of the TiO_2 substrate and (iii) subsequent dye regeneration by a redox electrolyte resulting in a photocurrent (see Chapter 4). One of the most efficient photosensitizers prevalently coated on the TiO_2 films of DSSCs is the N3 dye. The ruthenium polypyridyl complex is chemically attached to TiO_2 nanoparticles by designated anchor groups. Most importantly, the charge injection efficiency and consequently the overall photovoltaic performance of DSSCs strongly depends on the specific dye adsorption geometry on the TiO_2 substrate. Hence, tremendous efforts have been made over the last two decades to elucidate details of specific dye binding configurations.

Despite great theoretical and experimental efforts, no conclusive understanding of the structural and electronic properties of dye molecules adsorbed on TiO_2 surfaces has been achieved so far at the atomic level. In particular, the precise N3 adsorption geometry is currently highly controversially debated and profound uncertainty exists about the relationship between the photosensitizer's adsorption structure and the respective electronic characteristics. Moreover, the proposed supramolecular interaction between dye molecules lack experimental evidence. The lack of experimental evidence at the molecular level is primarily caused by major difficulties in successful sample preparation. Achieving fundamental understanding of the dye-TiO_2 interface would be greatly beneficial for providing chemists with specific design rules enabling the synthesis of optimized photosensitizers for maximum charge injection efficiencies and low recombination rates in DSSCs.

In the present thesis, the previously described challenges are adressed by means of scanning tunneling microscopy and spectroscopy methods combined with density functional theory (DFT) based calculations. The chapters of this thesis are organized as follows:

Chapter 1 gives a brief introduction into the theoretical background of scanning tunneling microscopy and spectroscopy methods. This is followed by the description of the sample preparation procedures employed for the realization of the presented MOCNs. Further, the electrospray ion beam deposition (ES-IBD) technique which was used to bring the thermally fragile N3 dyes onto the TiO_2 anatase (101) surface is specified.

Chapter 2 reports on the design and realization of the new scanning tunneling microscope operating in ultra high vacuum at 5 K. Details about both the integral parts of the STM unit and the cabling to the new liquid helium bath cryostat are presented. In the following, the construction of various additional new system components such as a manipulator head, an optical microscope or an UHV transfer suitcase unit will be described. Subsequently, the performance properties of the STM are presented.

Chapter 3 reports on the study of metal-organic coordination networks on metal substrates. In the first step towards the hierarchical assembly of extended functional MOCNs, the self-assembly and metal coordination of the rod-like organic ligand BDBA on gold, silver and copper surfaces is described. First, the adsorption conformations of the bare ligand are discussed. Afterwards, this chapter reports on the realization of self-assembled metal-organic coordination networks which grow continuously over multiple surface steps showing a high degree of insensitivity and adaptability to intrinsic surface defects. Finally, the chapter reports on the utilization of the surface confined MOCNs as templates to steer the adsorption and organization of catalytically active nickel atoms and clusters as well as secondary ligands for the assembly of multicomponent functional architectures.

Chapter 4 reports on the study of the geometric and electronic properties of the photosensitizer N3 on TiO_2 anatase (101) surfaces by means of scanning tunneling microscopy and spectroscopy methods in UHV. The unique method of electrospray ion beam deposition was employed to deposit the thermally fragile photosensitizer N3 onto the anatase substrate which is most relevant in DSSCs. The observation of multi-conformational N3 binding geometries revealed on TiO_2 anatase (101) is discussed and associated with the significant variations of the respective electronic properties which were probed with single molecule sensitivity. Furthermore, this chapter reports on the formation of N3 dye assemblies on the anatase surfaces that are potentially stabilized by supramolecular interactions. In addition, STM studies of the N3 anchoring ligand BINA are correlated to the multi-conformational N3 binding geometries. Addtional studies of the N3 dye on Au(111) surfaces are presented and the experimental findings supported by extensive density functional theory based calculations.

At the end, a summary and conclusion of the experimental and theoretical findings presented in this thesis will be given and promising future experiments presented.

1 Theoretical and experimental basics

This chapter gives a brief introduction into the theoretical background of scanning tunneling microscopy and spectroscopy methods. Subsequently, the experimental sample preparation procedures employed for the realization of metal-organic coordination networks are described. Furthermore, the technique of electrospray ion beam deposition which was used to bring the thermally fragile photosensitizer N3 onto the TiO_2 anatase (101) surfaces is specified.

1.1 Scanning tunneling microscopy

The technique of scanning tunneling microscopy was invented by Binnig and Rohrer in 1981 enabling both unprecedented three-dimensional surface imaging with spatial resolution at the atomic scale and manipulation of individual atoms.[2] Based on their original design, many variations of probe-based microscopes have been developed, such as atomic force microscopy (AFM), spin polarized scanning tunneling microscopy (SPSTM) and scanning near field optical microscopy (SNOM). STM measurements are not limited to UHV, but can also be performed in air, water and various other liquid or gas environments and at temperatures ranging from near zero kelvin to a few hundred degrees centigrade. The basic operational principle of a STM is shown in Figure 1.1a. A sharp metallic tip is moved in three dimensions along the sample via an x,y,z piezoelectric translator that is calibrated to move a precise distance when a given amount of voltage is applied. If the tip is positioned 5 - 10 Å above a conductive or semiconductive sample, the wavefunctions of both the tip and sample conduction electrons overlap. Consequently, provided that an additional bias voltage (10 mV - 10 V) is applied as indicated in Figure 1.1a, a tunneling current in the nanoampere range (0.1 - 5 nA) can be detected between the sample and the tip. The probability of electron tunneling through the barrier

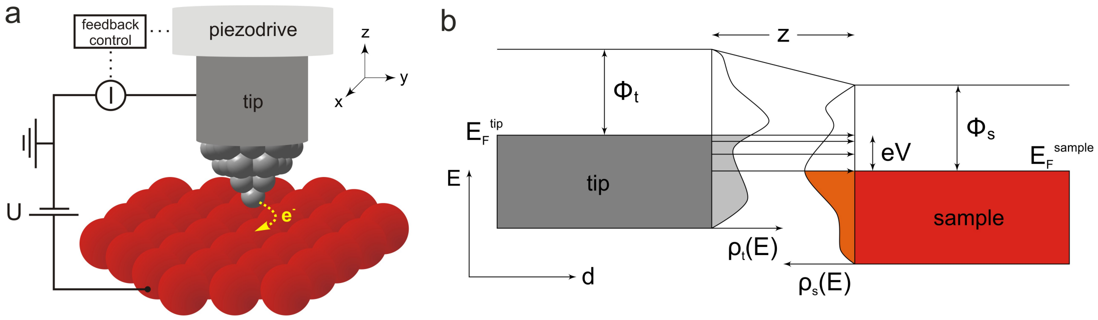

Figure 1.1: (a) Schematic illustration of a scanning tunneling microscope. (b) Potential energy diagram of a tip-sample tunneling barrier at positive sample bias voltage. Electrons tunnel from occupied states of the tip into unoccupied states of the sample.

between tip and sample decreases exponentially with the width of the barrier, so that the tunneling current mainly flows across the last atom at the tip apex and the surface area directly below. Thus, this technique allows vertical and lateral atomic resolution of the underlying surface. The STM can be operated in either the constant current or the constant height mode. In the constant current mode, a feedback loop adjusts the height of the tip to keep the tunneling current constant. Hence, the displacement of the tip given by the voltage applied to the piezoelectric drive yields a topographic map of the surface. Alternatively, in constant height mode, the tip is scanned across the surface at constant height and voltage while the tunneling current is monitored. Figure 1.1b shows the potential energy diagram of a tip-sample tunneling barrier. At positive bias voltage, the electrons tunnel from occupied states in the tip into unoccupied states of the sample. As indicated by the density of horizontal arrows, the current per energy unit decreases with energy since lower lying states decay faster into the vacuum barrier region. In order to calculate the tunneling current between tip and sample, commonly the Tersoff-Hamann[68,69] model is employed which applies Bardeen′s preeminent quantitative theory[70] to STM. Assuming a spherical tip geometry, it provides a relation between the tunneling current I(V) and the local density of states (LDOS) of the tip $\rho_t(\epsilon)$ and of the sample $\rho_s(\epsilon, x, y)$, the latter one also depending on the tip position above the surface (Figure 1.1b). Both tip and sample are supposed to be in thermal equilibrium at temperature T. The tunneling current I(V) between tip and sample at bias voltage V can then be approximated by

$$I(V,T,x,y,z) \propto \int_{-\infty}^{\infty} dE \rho_s(E,x,y)\rho_t(E{-}eV)\mathcal{T}(E,V,z)\left[f_\rho(E-eV,T) - f_z(E,T)\right], \tag{1.1}$$

where x and y characterize the lateral tip position on the sample and z stands for the tip-sample distance. $f_\rho(E-eV,T)$ and $f_z(E,T)$ are the Fermi distribution functions of tip and sample at temperature T and energy E, V is the applied bias voltage between tip and sample. $\mathcal{T}(E,V,z)$ denotes the transmission matrix of the tunneling gap given by[70]:

$$\mathcal{T}(E,V,z)=\exp\left(-2z\sqrt{\frac{m_e}{\hbar^2}(\Phi_\mathrm{s}+\Phi_{rmt}-2E+eV)}\right), \tag{1.2}$$

with the electron mass m_e and the work functions Φ_s and Φ_t of sample and tip, respectively. The features in the LDOS of tip and sample are broadened by the Fermi functions in the order of $\sim$ $\mathrm{k_BT}$. However, the temperature broadening of the spectra can be neglected if the investigated spectroscopic features have a width $\Gamma \gg \mathrm{k_BT}$. In this case, the Fermi function reduces to a step function which yields for eq. 1.1:

$$I(V,x,y,z)\propto\int\limits_0^{eV}dE\rho_s(E,x,y)\rho_t(E-eV)\mathcal{T}(E,V,z). \tag{1.3}$$

At V$\ll$ Φ_t and V$\ll$ Φ_s, $\mathcal{T}(E,V,z)$ (eq. 1.2) can be approximated by

$$\mathcal{T}(z)=\exp\left(-2z\sqrt{\frac{m_e}{\hbar^2}(\Phi_s+\Phi_t)}\right). \tag{1.4}$$

Hence, the tunneling current I(V) (eq. 1.1) can be rewritten as:

$$I(V,x,y,z)\propto\mathcal{T}(z)\int\limits_0^{eV}dE\rho_s(E,x,y)\rho_t(E-eV). \tag{1.5}$$

To note, this model is only valid in the limit of both low temperatures and low bias voltages and for a weak coupling between tip and sample. In (eq. 1.5), the prefactor describes the exponential z-dependence of the tunneling current and the integral factor describes the contribution from the LDOSs of the sample and the tip to the tunneling current. Thus, scanning tunneling microscopy gives convoluted information of the real surface contour and the electronic configuration of the sample and tip system.

In the constant height mode, the resulting current image can be directly calculated from (eq. 1.1). Alternatively, in the constant current mode, topographic images can be derived from (eq. 1.1) by setting the current to a constant $\mathrm{I_0}$ and adjusting the tip-sample distance z in the transmission coefficient $\mathcal{T}$ (eq. 1.2). Assuming small bias voltages V and constant current I_0, the following analytical expression can be derived for z:

$$z(V,x,y) = z_0 + \frac{1}{2\sqrt{\frac{m_e}{\hbar^2}(\Phi_s(x,y)+\Phi_t)}} \log \frac{\int\limits_0^{eV} dE \rho_s(E)\rho_t(E-eV,x,y)}{I_0}. \tag{1.6}$$

Spectroscopic information on ρ_s can be extracted from the variation of the tunneling current I with the sample bias voltage V. Experimentally, the tip is positioned at distance z over the sample, subsequently the feedback loop is opened and the tunneling current is measured dependent on the bias voltage V at constant z. Using eq. 1.5, the tunneling current can directly be calculated. Since I and hence the constant-current image involve an integral over a range of electron energies, its derivative dI/dV is commonly used to unravel spectroscopic information. Assuming that the LDOS of the tip ρ_t and the transmission coefficient $\mathcal{T}$ are independent of the voltage V, the dI/dV signal can be approximated by

$$\frac{dI}{dV} \propto \rho_s(eV)\rho_t(0). \tag{1.7}$$

This equation shows that the dI/dV signal is proportional to the LDOS at the position of the tip for small bias voltages at low temperature and with a tip of high spatial resolution and no strong features in its LDOS ρ_t. From this, the differential conductance can be calculated. In order to increase the signal-to-noise ratio, typically the dI/dV-signal is recorded using a lock-in amplifier where the bias voltage signal is modulated with an AC signal.

1.2 Sample and tip preparation

This section describes the experimental methods used for the preparation of samples on metal substrates (see Chapter 3). In addition, the basic principles of the electrospray ion beam deposition technique are introduced. The preparation of TiO_2 surfaces is described separately in Chapter 4.

Metal crystal preparation

In this work, noble single metal crystals of gold, silver and copper were employed. The commercially obtained crystals (supplier: MaTek GmbH) are circularly shaped with a diameter of 7 mm and thickness of 3 mm. Typically, the orientational misfit of the crystals is better than 0.1° and their surfaces are mechanically polished with a roughness lower than 30 nm.

The cleaning procedure for the metal crystals consists of repeated cycles of Ar^+ sputtering (ion energy 1000 eV, incidence angle 90°, $\sim 2\ \mu$A ion beam measured on the sample, 10 min) and annealing at 800 K (pressure below 3×10^{-9} mbar, 10 min). By this procedure, atomically clean and flat surfaces with terrace widths of about 80 nm are obtained.

Electron-beam heating evaporation of metals

Iron and nickel atoms, which are used for the preparation and functionalization of metal-organic coordination networks (see Chapter 3), were deposited onto the metal substrates using separate electron-beam heated evaporators (supplier: Omicron GmbH, type: EFM-3). Before deposition, the metal evaporators were carefully degassed. Typically, the deposition flux was in the range of 1 - 3 % of a monolayer per minute.

Organic molecular beam epitaxy

Both the BDBA and BINA molecules employed in this work (see Section 3 and 4.4) were deposited in UHV by organic molecular beam epitaxy from a resistively heated quartz crucible. During deposition, the crucible was held at the sublimation temperature of 560 K and 522 K, respectively. Typically, the pressure in the UHV preparation chamber did not exceed 3.0×10^{-9} mbar during the deposition.

Tip preparation

STM measurements presented in Chapter 3 were performed using home-made electrochemically etched tungsten tips. After transfer into the UHV system, they were treated by field emission and prepared on a clean Au(111) surface. However, working on TiO_2 surfaces (see Chapter 4), STM measurements turned out to be most stable when electrochemically etched Pt-Ir(80-20)-tips (supplier: Agilent GmbH, type: N9801A) were used. In this case, the tip preparation consists of two steps: firstly, the tip is annealed at ~ 600 K for 10 minutes in UHV. In the next step, the tip is treated by field emission and subsequently prepared on a clean Au(111) surface for topographical imaging and spectroscopy.

1.3 Electrospray ion beam deposition

Samples of quality suitable for scanning probe microscopy are typically fabricated on a single crystalline surfaces. Vapour condensation of sublimated atoms or molecules offers a controlled, contamination free deposition, which can however not be applied to large organic molecules, which are often not volatile and only decompose upon heating. In this context, the electrospray ion beam deposition (ES-IBD) technique allows the deposition of large, thermally fragile and non-volatile molecules onto solid surfaces in UHV and its feasibility has been demonstrated for complex molecular structures.[71–75] The photosensitizer N3 studied in this work (see Section 4.3) also undergoes thermal decomposition before it sublimates and consequently cannot be deposited onto the substrates of interest via thermal evaporation. In this work, the unique ES-IBD technique was employed for the gentle deposition of intact N3 dye molecules onto TiO_2 anatase (101) and Au(111) surfaces.

Figure 1.2 illustrates the schematic setup of the ES-IBD system. The basic principle of the ES-IBD is the electrospray effect where a liquid is dispersed into an aerosol by applying a high electric field.[76] The home build setup shown in Figure 1.2 consists of an ES ion source at ambient pressure and six differential pumping stages, that reduce the pressure from 0.1 mbar to UHV (10^{-11} mbar). The utilization of ion optics, current detection and mass spectrometry results in complete control over all experimental parameters, most importantly the chemical composition and the amount of deposited material. ES-IBD setups typically resemble ES mass spectrometers with features added that are needed for the controlled ion beam deposition, i. e. additional deposition chambers and sample holders.

The spray needle (ES, see Figure 1.2) is fed with N3 solution of 10^{-4} mol/l in ethanol. The source is operated in negative ion mode, applying a high voltage of +4.2 kV to the metalized front-end (high-pressure side) of the capillary. The ions created in the electrospray pass the glass capillary and expand with the carrier gas into the first pumping stage. The dc-voltages applied to the metalized back-end (low-pressure side) of the capillary and the ion funnel define the declustering potential V_{decl}. The declustering potential is a measure for the intensity of the collisions of the ions with the neutral background gas, which is used to break apart cluster ions or create molecular fragments. Usually V_{decl} is in the range of 100 - 400 V. The following pumping stages are equipped with various ion optics for collimation, mass-selection and focusing of the ion beam. In the first stage (IF), a radio frequency (rf) ion funnel (1MHz, 330V) bundles the ions expanding into vacuum into a compact cloud that is passed to the next chamber (0.01mbar).

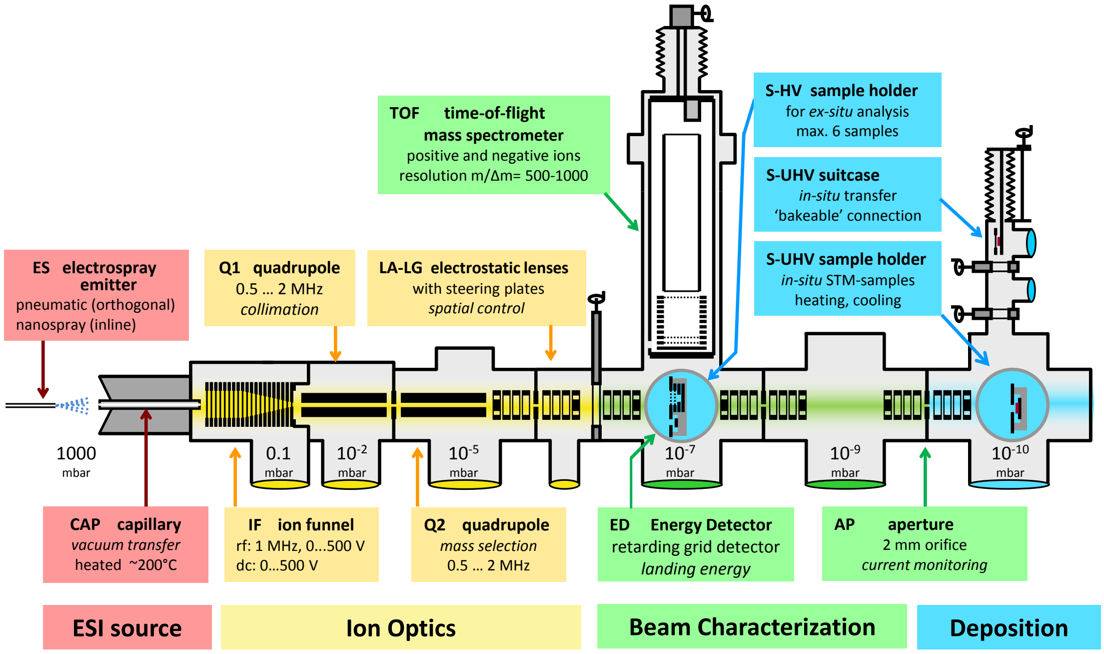

Figure 1.2: Schematic setup of the electrospray ion beam deposition system.

There, a quadrupole (Q1) operated in rf-only mode (0.5 - 2 MHz, 50 - 200 V_{ac}) collimates the ion beam by collisional cooling. In the third pumping stage at 10.5 mbar another rf-quadrupole (0.5 - 2 MHz, 50 - 500 V_{ac}) is used as a mass selective ion guide (Q2). Further downstream electrostatic lenses with included steering plates (LA-LG) pass the ion beam through 2 mm diameter apertures, which serve as separators between the pumping stages and can be used for current monitoring, when aligning the ion beam. A linear, orthogonal extraction, time-of-flight mass spectrometer (TOF) is mounted on a z-travel in the fourth pumping stage and can be retracted from the beam axis if not in use. The instrument can detect positive and negative ions and has a resolution of m/Δm = 300, which is sufficient to confirm the intactness of a molecular species. Three different sample holders are mounted in the 4th, 5th, and 6th pumping stage. The sample is placed behind an aperture in a shield electrode - both connected electrically for current measurement and the applying of voltages. Well defined electric fields can be generated that accelerate or decelerate the beam without major disturbance to the focusing, which allows to control the deposition energy. In addition the current measurement offers precise control of the flux and coverage. The high vacuum sample holder (S-HV sample holder) in the TOF chamber is used for deposition of samples for ex-situ analysis as well as for exact measurements of the beam energy with an integrated retarding grid detector. A vacuum suitcase (S-UHV suitcase) containing a fully functional ion beam deposition sample holder can be mounted at the fifth pumping stage. Here samples from the low temperature scanning tunneling microscope operated at 1 K can be introduced for deposition at 10^{-9} mbar. Finally, also in the 6th pumping stage a sample stage is mounted, which is used to coat substrates intended for in-situ analysis with the connected STM. To avoid any contamination at the surface the N3 ion beams were mass selected using the quadrupole in the 3rd pumping stage. To further ensure the intact deposition the ion beams were decelerated by applying an appropriate voltage to the sample. The kinetic energy was measured at values of 35 - 50 eV and the bias at the sample was set to 30 - 45 V respectively, which lead to deposition energies of 5 eV. During the deposition the ion current was monitored, which allows a precise adjustment of the molecular coverage. After a desired coverage has been deposited, the sample is transferred in situ into the STM - either directly or via the vacuum suitcase.

2 Realization of a new 5 K scanning tunneling microscope

As a prerequisite for experiments presented in this work, a new type of low temperature scanning tunneling microscope operating in UHV at 5 K was realized. The STM fulfills following criteria: (i) precise tip z-approach, (ii) lateral sample positioning with (sub-)micrometer precision, (iii) simple in-situ tip exchange, (iv) optical access for controlling the sample position and irradiating the sample with light, (v) multiple electrical sample access for in-situ transport and back-gate functionalities and (vi) use of versatile sampleholders for different substrates. This STM provides a basis for future experiments on various substrates including graphene to which a backgate voltage can be applied. The optical sample access further allows for investigations of light-induced and photon-emission processes (see Conclusions and Perspectives).

This chapter first describes the UHV system into which the STM unit was integrated. As a second point, the mechanical and electrical connection to a new helium bath cryostat is specified in more detail. Subsequently, the design and realization of the STM unit itself as well as additional system components will be introduced. At the end of this chapter, the performance of the STM is demonstrated.

2.1 Design, construction and setup

2.1.1 UHV system

The UHV system, into which the new STM unit was integrated, consists of a preparation and an analysis chamber. These chambers are separated by a plate valve as illustrated in Figure 2.1. The preparation chamber is equipped with standard surface preparation tools (e.g. an ion gun for the sputtering of samples, gas dosing equipment) and a quadrupole mass-spectrometer for the analysis of rest gases. Moreover, several evaporators for metals and organic molecules are available. The sample can be positioned in both UHV chambers by a linear transfer manipulator. A load-lock unit, installed at the preparation chamber, enables the transfer of both samples and STM tips between ambient and UHV condition and the mounting of a UHV transport suitcase (see Section 2.1.4). In both the preparation and the analysis chamber, a sample storage magazine, for maximum four samples respectively, is integrated. In the analysis chamber, the STM unit is mounted to a liquid helium bath cryostat (Figure 2.2) which is surrounded by a liquid nitrogen shield. The base pressures in the preparation and the analysis chamber are lower than 3×10^{-10} mbar and 6×10^{-11} mbar, respectively. The whole UHV system is installed on an optical table which is decoupled from external vibrations by one active and one passive damping stage. Furthermore, a second passive damping stage decouples the liquid helium bath cryostat from the liquid nitrogen shield cryostat.

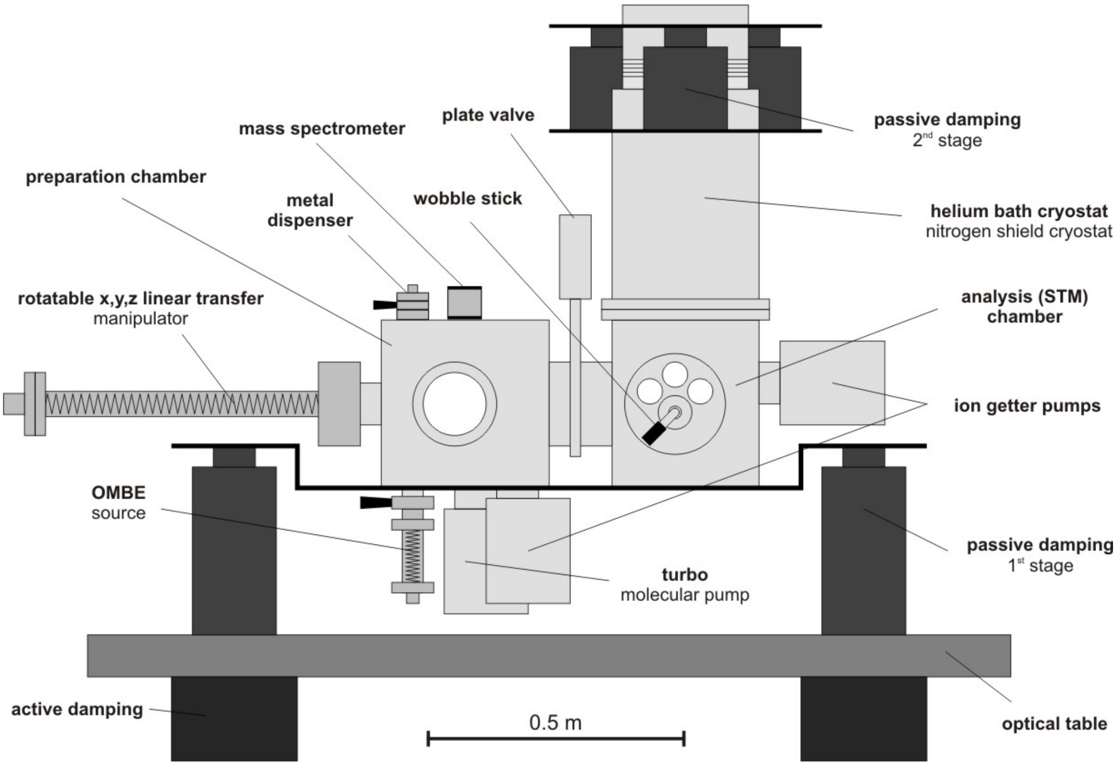

Figure 2.1: Schematic view of the UHV 5 K scanning tunneling microscopy setup consisting of the preparation chamber equipped with standard surface preparation tools and the analysis chamber containing the STM unit.

2.1.2 Helium cryostat

Within the framework of developing the STM unit (see Section 2.1.3) and integrating it into the UHV system described before, the existing liquid helium bath cryostat was replaced by a new one which is shown in Figure 2.2a. The typical STM operation temperature is aimed at maximal 5 K.

The cryostat top plate comprises UHV compatible BNC- and multipin-feedtrough connectors, a common electrical grounding plate and a burst disc. In order to ensure the STM operation temperature of 5 K, all cables and wires connected to the STM unit are thermalized at different temperature levels of the cryostat. Further, a cable thermalization unit was designed and integrated as shown in Figure 2.2b. For the current and z-electrode signals, shielded phosphor bronze wires (supplier: Lake Shore Cryotronics Inc., type: CC-SC) were employed. Further, shielded stainless steel coaxial cables (supplier: Lake Shore Cryotronics Inc., type: CC-SS) with a low thermal conductivity were used for bias and sample contacts. The shieldings of these sensitive signal cables are electrically not interrupted along the whole connection to the STM unit. On the other hand, non-shielded manganin wires in twisted pair-/quad-configuration (supplier: Lake Shore Cryotronics Inc., type: WDT-36, WQT-36) were used for the less sensitive xy-electrodes of the scanning piezo, the xy-shear actuators, the two temperature sensors and the heating diode (see Section 2.1.3). For the attocube coarse approach, a thicker manganin wire was chosen since the maximum wire resistance should not exceed 10 Ohms for ideal operation.

2.1.3 STM unit

Figure 2.3a schematically illustrates the design of the STM unit which consists of an approach-scanning unit (indicated in blue) and a sample translation stage (indicated in green/yellow). The STM is machined out of gold-plated, UHV compatible oxygen free phosphor bronze. It is mounted modularly to the liquid helium bath cryostat as shown in Figure 2.3b and 2.3c, respectively. Detailed views of the STM components are depicted in Figure 2.4.

In this home-designed STM version, a highly stable tip-approach is achieved using a commercial coarse-motion piezo z-stage (supplier: Attocube Systems AG, type: ANPz101) which is mounted to the STM base plate (Figure 2.3a). The scanning piezo, a lead zirconate titanate ceramic tube (supplier: EBL Products Inc., type: EBL #3), is glued (supplier: Polytec PT GmbH, type: Epo-Tek E4110/H71) into

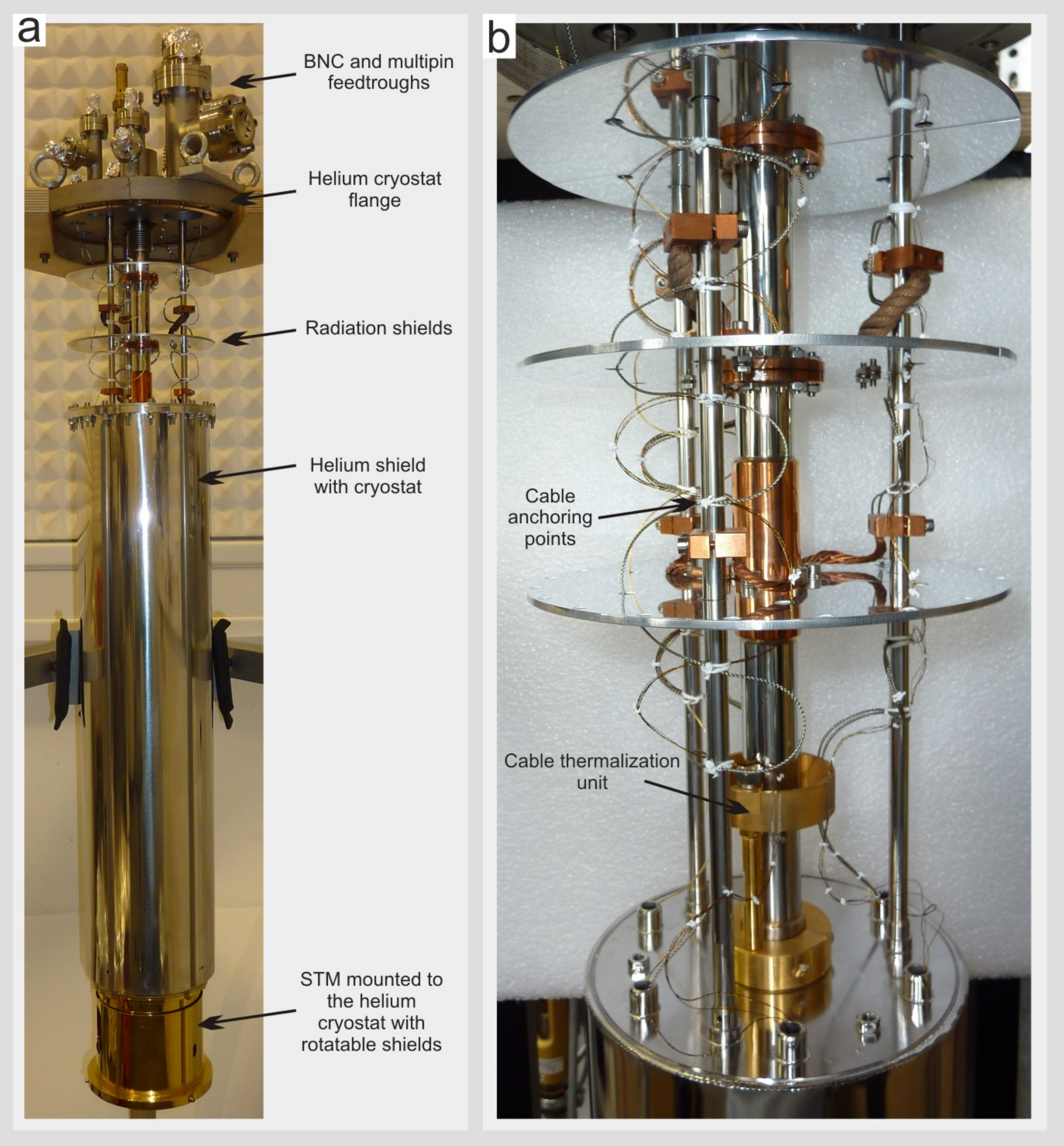

Figure 2.2: The new liquid helium bath cryostat to which the STM unit is connected. (a) From top: UHV cable feedthroughs, helium cryostat top flange, radiation shields, helium pot with radiation shield and STM unit surrounded by a rotatable shield. (b) Zoom-in image of the top part of the liquid helium bath cryostat. All cables and wires are thermalized at different anchoring points including a home-built cable thermalization unit.

a sapphire plate on top of the attocube z-stage (Figure 2.4a). Both the coaxial cables for z-electrode and current (see below) are guided through this sapphire plate in order to reduce the mechanical strains on the scanning piezo. The tip can be easily screwed into the tipholder (Figure 2.6 a) which is made of magnetic

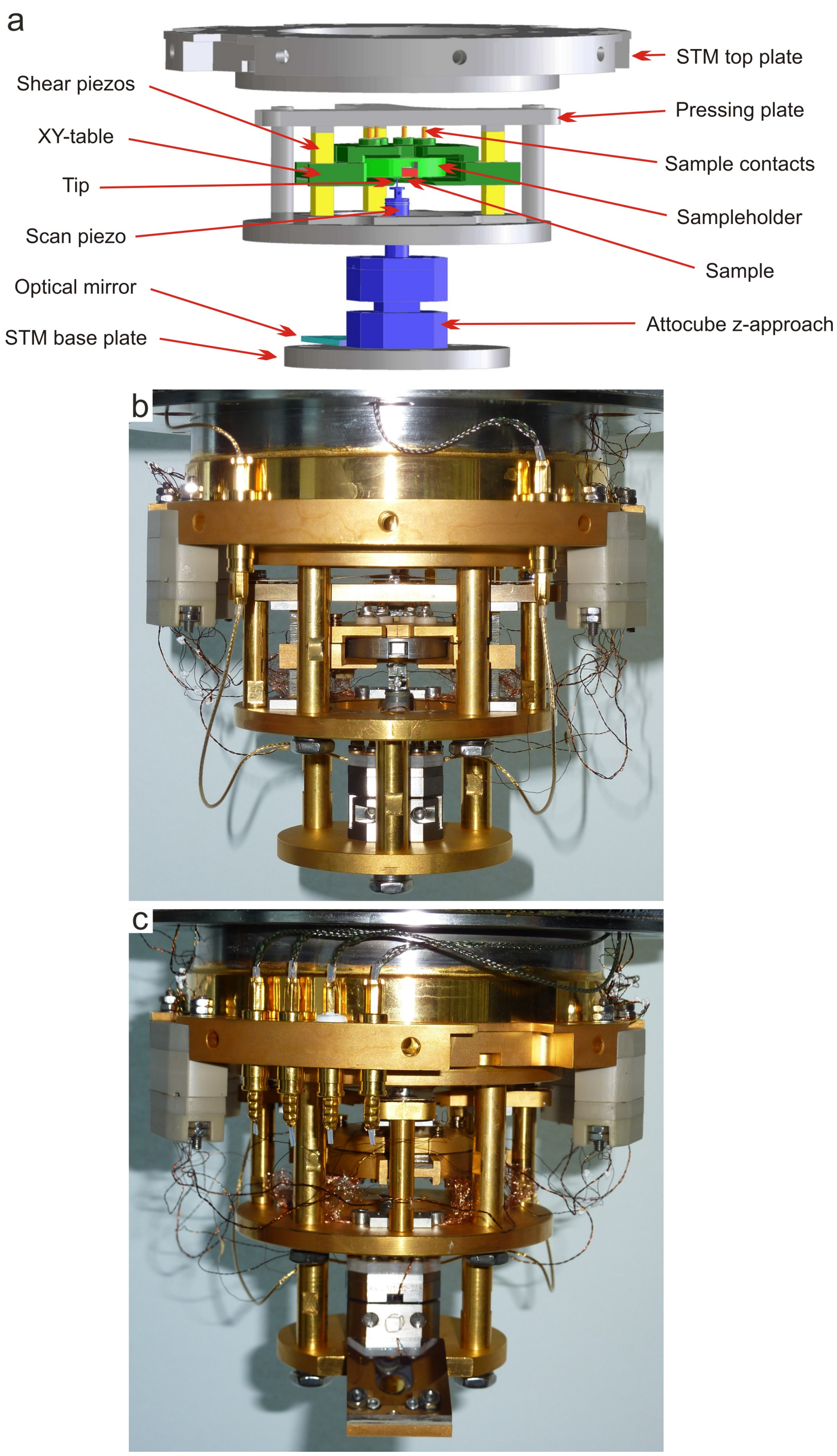

Figure 2.3: The new 5 K STM. (a) Schematic overview of the STM unit consisting of the approach-scanning unit (blue) and sample slip-stick translation stage (green/yellow). Image of the front side (b) and back side (c) of the STM unit which is mounted to the liquid helium bath cryostat.

stainless steel. The tipholder is inserted into a magnetic receptacle which is glued to the scanning piezo (Figure 2.4b). The optical access to the sample is realized using an UV-enhanced aluminium-coated flat mirror (supplier: Melles Griot GmbH, type: Oauv-Mfg-50003M-C) held by two copper-beryllium springs on a mirror plate (Figure 2.4c). The whole approach-scanning unit is mechanically connected to the sample translation stage via three metal rods.

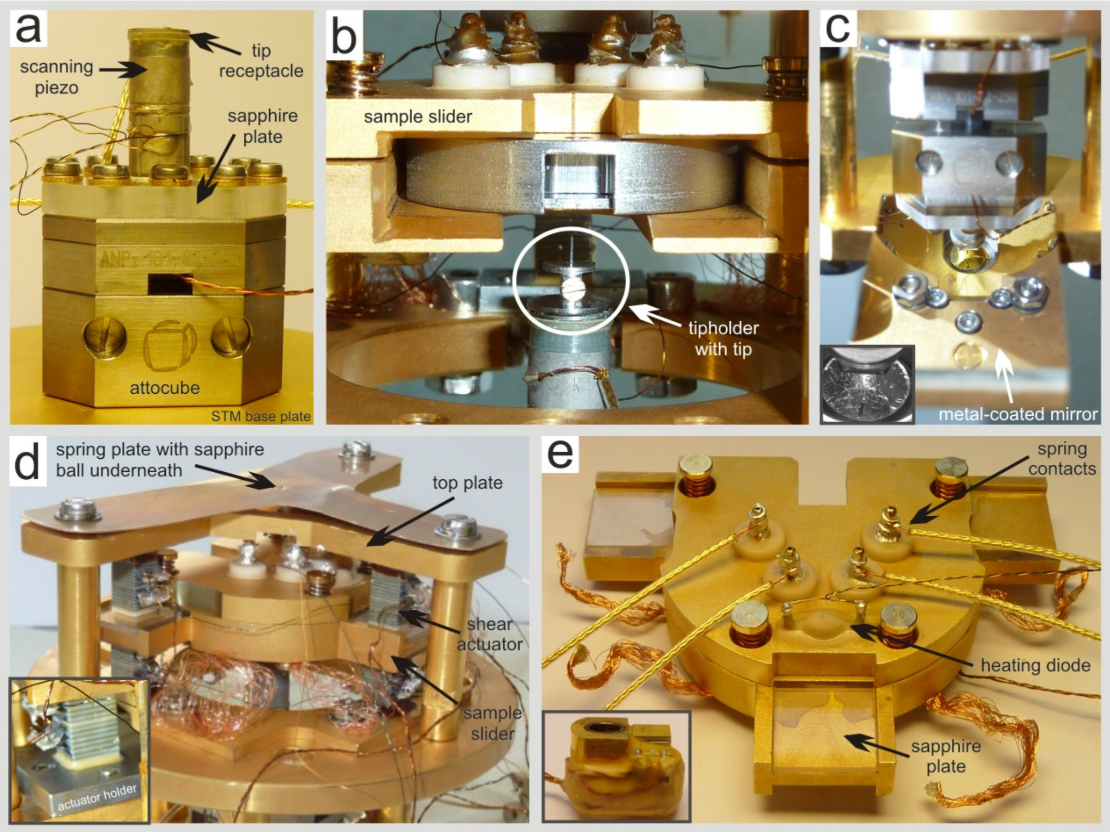

Figure 2.4: (a) Attocube coarse-motion piezo z-stage mounted onto the STM base plate. The scanning piezo and magnetic tip receptacle are assembled on top of a sapphire plate. (b) Tip screwed into the tipholder approaches from below the sample which is kept in the sample slider. (c) Optical sample access via a metal-coated mirror. The inset shows a CCD-camera image of the tip / Au(111) sample during approach. (d) Sample translation stage with sample slider pressed by a spring plate and a sapphire ball with adjustable frictional force in between the six xy-piezoelectric shear actuators. Surfaces in frictional contact are made of planar sapphire plates allowing lateral slip-stick motion. One side of the actuators is glued into molybdenum holders (see inset). (e) Sample slider with four separate electrical sample contacts, integrated heating diode and copper braids for optimized sample thermalization. The sampleholder is fixed via four pressing springs. The inset shows the Cernox temperature sensor mounted to the bottom side of the sample slider via a thermalization unit.

The sample translation stage shown in Figure 2.4d consists of the sample slider (Figure 2.4e) and the lateral sample positioning system (indicated in yellow in Figure 2.3a). The sampleholder, inserted into the sample slider, is electrically accessed via four isolated spring contacts (Figure 2.4e, supplier: Feinmetall GmbH, type: F70611B130G150ST). Further, a heating diode (supplier: Vishay, type: BZT03C200) is integrated into the sample slider to allow in-situ sample heating. The sample temperature is measured by a Cernox thin film resistance cryogenic temperature sensor (supplier: Lake Shore Cryotronics Inc., type: CX-1050-SD-HT-P) which is mounted at the bottom side of the sample slider via a thermalization unit (inset Figure 2.4e). The thermalization of the sampleholder is optimized by flexible copper braids which connect the sample slider to the STM body. A second temperature sensor is mounted to the STM top plate.
The precise lateral positioning of the sample slider both in x- and y-direction is based on the principle of inertial slip-stick step motion[77] using six xy-piezoelectric shear actuators terminated with Al_2O_3 (supplier: PI Ceramic GmbH, type: PAXY + 0048). As a first step, the shear piezos are accelerated rapidly over a short period of time so that the inertia of the sample slider overcomes static friction. The sample slider remains nearly nondisplaced. Subsequently, the shear piezos move back to their initial position slowly enough that the sample slider sticks to the shear piezos and makes a net step. As shown in the inset of Figure 2.4d, the shear actuators are glued on one side into a molybdenum holder to maximize the mechanical stability and match thermal dilation parameters. All surfaces exhibited to frictional contact are made of planar sapphire plates. The constant frictional force is adjusted via choosing the right diameter of the sapphire ball sitting in between the spring plate and the sample stage top plate (Fig. 2.4d). The x-/y-displacement of the sample slider is restricted by three rods enabling sample positioning in the range of ± 5 mm. This setup typically allows displacement steps down to 1 μm.
In the STM unit, shielded phosphor bronze wires were used for the signals of current and z-electrode. For bias and sample contacts, unshielded phosphor bronze cables were used. In a similar way to the cryostat cabling, non-shielded cryogenic wires in twisted pair-/quad-configuration were used for the xy-electrodes of the scanning piezo, the xy-shear actuators, the two temperature sensors, the attocube coarse approach and the heating diode. To allow easy removal of the STM from the helium cryostat, the cables are attached via SMB connectors (supplier: Allectra GmbH, type: 245-CON-SMB(-F)) and multi-pin plugs (supplier: Allectra GmbH, type: 360-PPO-2.4) to the STM top plate.

2.1.4 System components

In this section, the design of new home-built system components which were necessary for the STM setup is described.

Sampleholders for various substrates

Three different sampleholders are designed to accommodate various types of samples, particularly (a) metal crystals, (b) natural single oxide crystals and (c) graphene samples as depicted in Figure 2.5. All sampleholders are machined out of molybdenum due to its mechanical stiffness, heat resistance and UHV compatibility. As shown in Figure 2.5a, metal crystals are kept isolated from the sampleholder by sapphire rings and are electrically accessed by contact wires (for bias and thermocouple) which are pressed between the sample and sapphire ring. The suitably cut natural TiO_2 anatase single crystals (see Chapter 4) are pressed into a molybdenum base plate. The electrical contacts are integrated into the molybdenum plate and isolated from the sampleholder by a sapphire ring (Figure 2.5b). In addition, also sampleholders for graphene samples were prepared. For example, a CVD graphene sample on silicon oxide can be glued onto a sapphire base plate which fits into the sampleholder (Figure 2.5c). The graphene sheet can be electrically contacted via bonding wires.

Tip exchange mechanism

Working with metal oxide surfaces necessitates regular tip exchanges. To this end, a reliable and simple in-situ tip exchange mechanism is realized as shown in Figure 2.6a. For changing the tip, the tip exchange slider is put into the sample

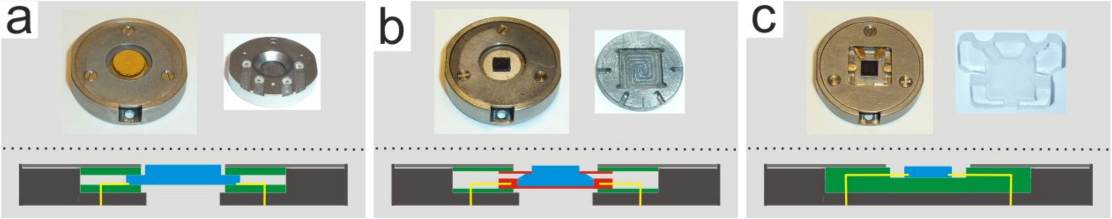

Figure 2.5: Schematic view and image of sampleholders for (a) metal crystals, here Au(111) (bottom / top side) (b) natural single crystals, here TiO_2 anatase (101) with molybdenum base plate and (c) backgated substrates, here CVD-graphene on silicon oxide with sapphire base plate. (black: sampleholder, grey: top-plate, blue: sample, green: sapphire plate, red: molybdenum plate, yellow: electrical contacts)

slider. Subsequently, after positioning the tipholder (Figure 2.6a) into the exchange slider, it can be removed by retracting the magnetic tipholder receptacle using the attocube piezo z-stage. A CCD-camera snapshot of the tip exchange procedure is shown in Figure 2.6 a.

New manipulator head

To accommodate the designed sampleholders, a new manipulator unit needed to be realized. The manipulator head shown in Figure 2.6b is machined out of oxygen free copper and mounted on a rotatable manipulator in the preparation chamber (Figure 2.1). The sampleholder is kept in the manipulator head by a molybdenum plate which is pressed to the manipulator body via heat-resistant springs (supplier: Gutekunst+Co. KG, type: D-041A). Four contact rods, isolated via sapphire plates from the manipulator body and pressed by tempered springs onto the sampleholder contacts, allow electrical sample access (e.g. for applying high voltages and for temperature read-out). A tungsten filament allows the annealing of the sample at up to 1200 K by electron bombardment. Free space has been left to add additional components such as a tip sputtering unit to the manipulator head.

Optical system

The optical system consists of a microscope zoom-system and a monochrom light-sensitive CCD camera (Figure 2.6c, supplier: EHD Imaging GmbH, type: Zoom 125 system (2.0X TV-tube, zoom 125 w/iris, 15mm fine focus, 0.25 X aux. lens, flat flange mount, UK1156M CCD camera)) placed outside the UHV chamber. A special optic holder was designed to enable precise positioning in x-/y-/z-direction to allow the focusing on a desired sample spot. The optical path passes a standard UHV viewport and the STM mirror with a total working distance of 310 mm. In this system, the field of view can be tuned from 1.48×1.97 mm^2 to 18.46×24.62 mm^2 with a numerical aperture of 0.025 and a theoretical resolution of 14 μm. Further, an optical fibre holder is installed to allow sample light irradiation (e. g. using a laser). The rotatable helium and nitrogen shields of the STM unit are modified to feature closable holes that allow optical sample access (inset Figure 2.6c).

Sample transport suitcase

The in-situ sample transfer between the UHV STM and the electrospray ion beam deposition system (see Section 1.3) is realized using an UHV vacuum suitcase. As shown in Figure 2.6d, it consists of a sample transfer rod, an ion pump, a getter pump, a pressure control and a battery unit as power supply for mobile transport. The front unit (Figure 2.6d top) was designed and constructed to accommodate the new type of sampleholder and is made out of stainless steel. The sampleholder inserted in the suitcase is held by four springs integrated into the front unit and one centered top spring. The sample is grounded to the front unit body by top spring contacts. On the bottom side, an electrically isolated blend is installed for the ESI deposition (see Section 1.3). The UHV transport suitcase base pressure is typically lower than 3.0×10^{-10} mbar.

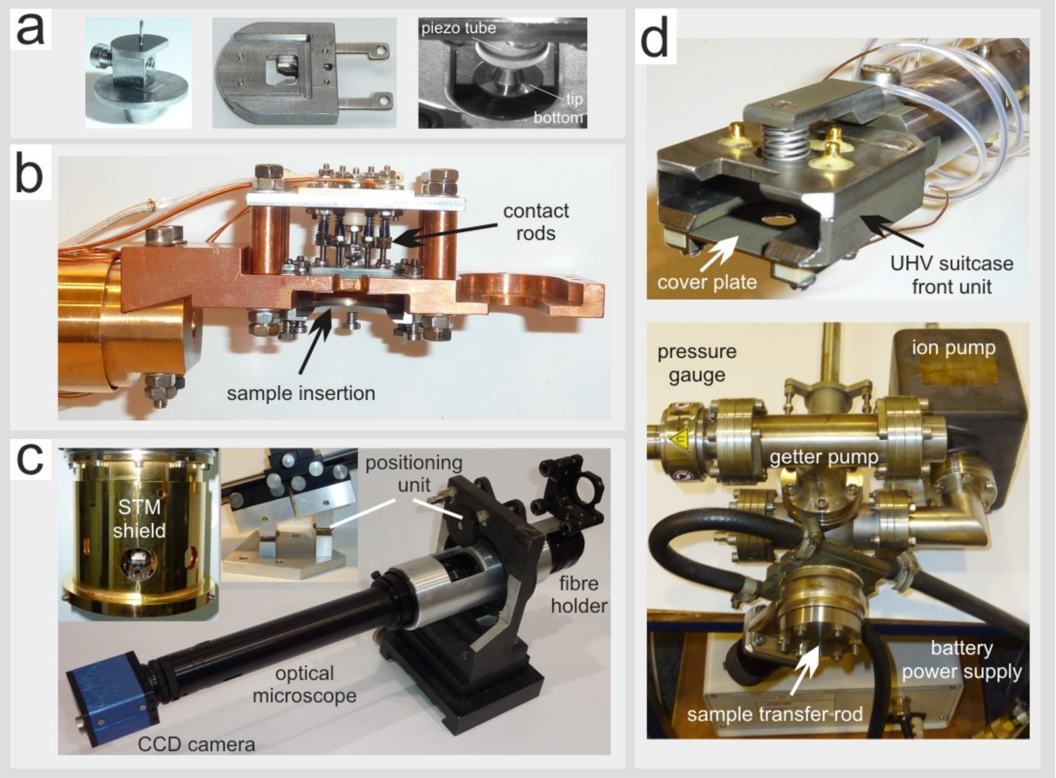

Figure 2.6: (a) Tipholder with tip, tip exchange slider and CCD-camera snapshot of the tip exchange procedure. (b) New manipulator head for sample and tip preparation (e. g. annealing, sputtering). (c) Optical system consisting of a microscope zoom-system, a CCD-camera and an optical fibre holder with precise x-/y-/z-positioning unit. STM shields are modified with closable holes enabling optical access. (d) Top: newly designed suitcase front unit to accommodate the sampleholders. Bottom: mobile UHV transport suitcase with ion pump, ion getter pump, pressure control and battery power supply.

2.2 System performance

The performance of the new STM was tested on the Au(111) surface which is well suited for topographic and spectroscopic characterization.[78,79] Here, the Au(111) substrate was cleaned following the procedure described in Section 1.2. The STM measurements were performed in constant current mode at 5 K using a chemically etched tungsten tip. No filtering procedures were applied for the recorded data.

Topography

Figure 2.7a shows a STM topography image of the clean Au(111) surface which is characterized by large, atomically flat terraces separated by monoatomic steps of ∼ 2.4 Å height. The prominent herringbone superstructure resulting from the $22\text{x}\sqrt{3}$ reconstruction is clearly visible. A corrugation amplitude of ∼ 0.2 Å can be derived from the corresponding linescan which matches well with values found

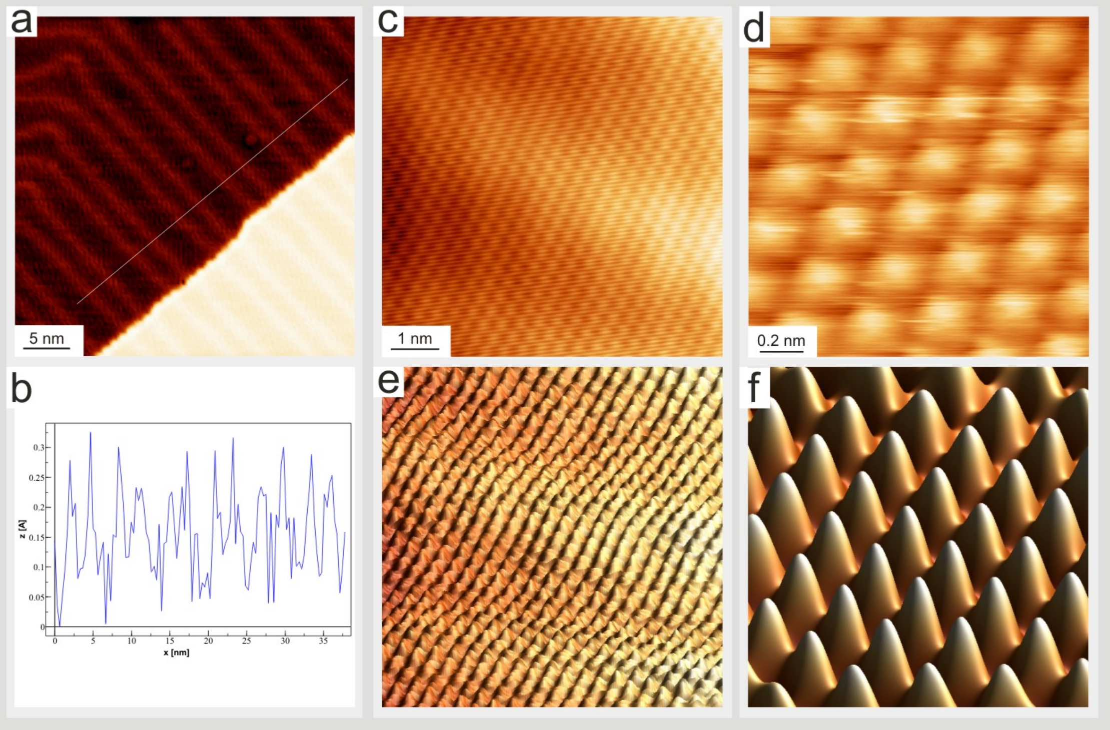

Figure 2.7: Constant current STM images of the reconstructed Au(111) surface measured at 5 K. (a) Overview of the stepped Au(111) surface (1.0 V, 1.0 nA, 5 K), (b) linescan along direction indicated in (a), enlarged STM images revealing (c) herringbone structure with atomic substrate resolution (0.1 V, 5.0 nA, 5 K) and (d) atomic substrate resolution (0.1 V, 30 nA, 5 K). (e) and (f) 3D views of (c) and (d), respectively.

in previous studies.[78] Analysis of linescans shown in Figure 2.7b result in a peak to peak z-noise of $\sim$ 4.9 pm. Figure 2.7c and d show high-resolution STM images of the atomically resolved Au(111) substrate.

Spectroscopy

Figure 2.8a shows a differential tunneling current spectra measured on Au(111). The measured gold surface state onset of -0.5 eV below the Fermi energy is in good agreement with well-known values from STS[79] and photoemission[80] studies. Figure 2.8b shows the distance-voltage characteristics (z(V)-spectrum) of Au(111). The image-potential states are identified at 5.3, 7.0, 7.8, 8.4 and 9.0 V. Here, the typical features are the large width of the n=1 state and the shoulder at about 3.6 V.

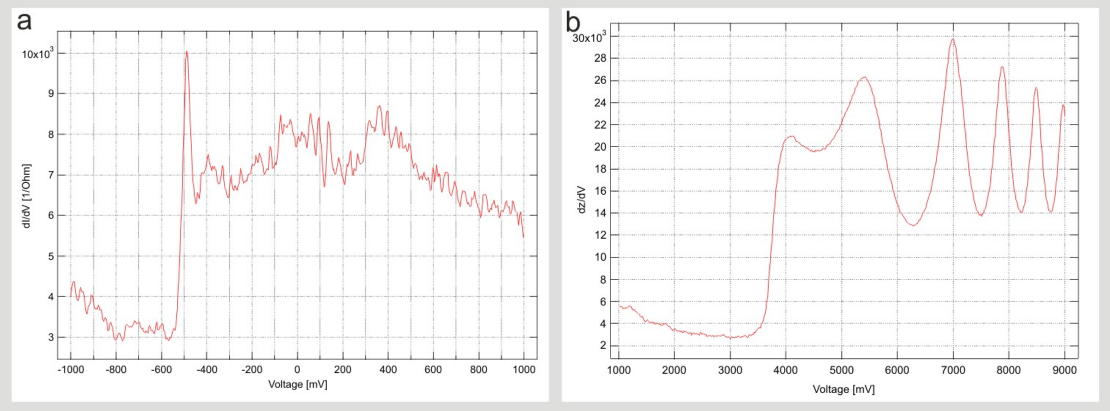

Figure 2.8: Electronic characterization of the Au(111) surface at 5 K. (a) dI/dV-spectrum with the surface state at - 0.5V. (b) Potential image characteristics.

In conclusion, the z-stability and spectroscopic performance comply with state of the art microscopes working at liquid helium temperatures. Its high performance stability has been proved over the last two years.

3 Patterning and functionalization of metal surfaces

The first part of this chapter reports on the realization of self-assembled metal-organic coordination networks (MOCNs) which grow continuously over multiple surface steps showing a high degree of insensitivity and adaptability to intrinsic surface defects. The second part of the chapter reports on the utilization of these surface confined MOCNs as templates to steer the adsorption and organization of catalytically active nickel atoms and clusters as well as secondary ligands for the assembly of multicomponent functional architectures.

3.1 Highly adaptable 2D-MOCNs

Supramolecular assembly of surface-confined 2D-architectures is a topic of intense research with potential applications in surface patterning,[28,81,82] catalytic model systems,[37,83] molecular electronics, and spintronics.[84,85] In particular, surface assisted metal-coordination bonding allows the synthetic bottom-up fabrication of molecular architectures of well-defined geometry with specific functional properties. Many examples of diverse metal-organic coordination networks with tunable sizes and topologies,[86] suitable for host-guest chemistry,[87,88] and regular arrays of spin centers[89] were demonstrated. Moreover, 2D metal-organic superlattices with a high degree of structural order up to the micrometer range were reported.[90] Recently, on-surface covalent polymer networks have gained increasing attention as a route to pattern surfaces with molecular adlayers due to their high thermal and chemical stability.[91–97] However, in contrast to MOCNs, the structural control of polymer networks is limited by the presence of radical and highly reactive intermediates during the assembly process and the exclusion of error correction in the irreversible formation of covalent bonds. MOCNs, on the other hand, show self-selection and error correction as demonstrated by a heteroleptic bonding motif due to the specific

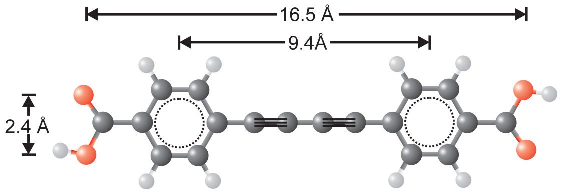

Figure 3.1: Chemical structure of the 4,4’-di-(1,4-buta-1,3-diynyl)-benzoic acid with carboxylic and alkynyl functionalities (H, white; C, gray; O, red).

binding of the ligands to the metal centers.[86] Apart from separated examples of graphene and hexagonal boron nitride layers, one common obstacle of both MOCNs and polymer networks is the limitation of the mesoscale ordering imposed by substrate step edges. Recently, the assembly of several hundred nanometer long one-dimensional molecular chains driven by hydrogen bonds showing crossing over step edges was observed on one specific substrate and surface symmetry.[29,98] However, 2D-MOCNs were not observed to show insensitivity to native surface steps and defects.

Here we address the challenge of designing 2D-MOCNs that overcome the limitations imposed by surface steps. To this end, we have synthesized the rod-like ligand 4,4’-di-(1,4-buta-1,3-diynyl)-benzoic acid BDBA[99–101] which is schematically depicted in Figure 3.4. The BDBA constitutes a rod-like multitopic ligand comprising a high degree of π-electron density within its molecular structure. Sample preparation and characterization were conducted in two ultrahigh vacuum systems equipped with a home-built variable temperature and a low-temperature scanning tunneling microscope. STM data were recorded in constant current mode after the sample was cooled to room temperature or 5 K, respectively. The base pressure of both systems is better than 3×10^{-10} mbar. Single crystal Cu(100), Ag(100) and Au(111) surfaces were prepared by repeated cycles of Ar^+ sputtering and annealing at 800 K (see Section 1.2).

3.1.1 BDBA on Cu(100), Ag(100) and Au(111)

The BDBA molecule was first thermally evaporated onto Cu(100). The results obtained by means of variable temperature scanning tunnelling microscopy are shown in Figure 3.2a. On Cu(100), substrate induced conformational changes of the organic ligand with strong molecular relaxations on the Cu(100) surface were observed. Here, the BDBA alkynyl groups bind strongly to the metal substrate leading to a partial sp^2-hybridization of the alkynyl carbon atom and thus to the observed molecular bending. As depicted in Figure 3.2b - 3.2d, the size of these

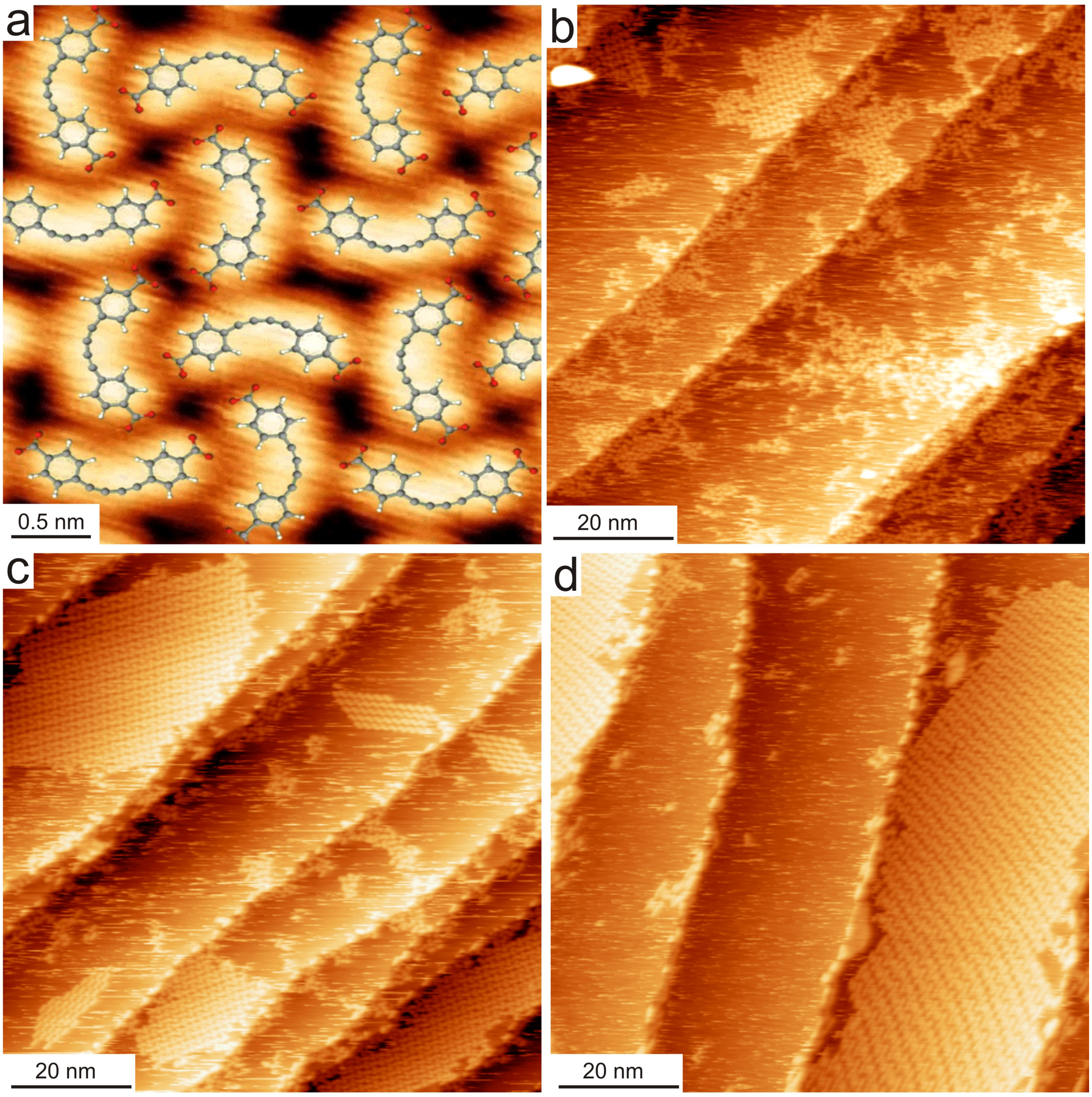

Figure 3.2: (a) BDBA molecular domain on Cu(100). The molecules are clearly bended upon adsorption. The BDBA domains grow in size with increasing substrate annealing temperature of (b) 350 K, (c) 400 K and (d) 450 K.

molecular domains increases with higher annealing temperatures.

Upon room temperature deposition on Ag(100) surface, BDBA molecules form large domains consisting of close-packed linear chains parallel to the surface principal directions (Figure 3.3a). Within a chain the molecules potentially bind to each other via complementary carboxylic hydrogen bonds.[102] Adjacent rows potentially interact by attractive carboxyl-phenyl hydrogen bonds and van-der-Waals forces. Annealing of the BDBA / Ag(100) system at temperatures above 430 K leads to the reorganization of the molecules into a chiral chevron pattern (Figure 3.3b) similar

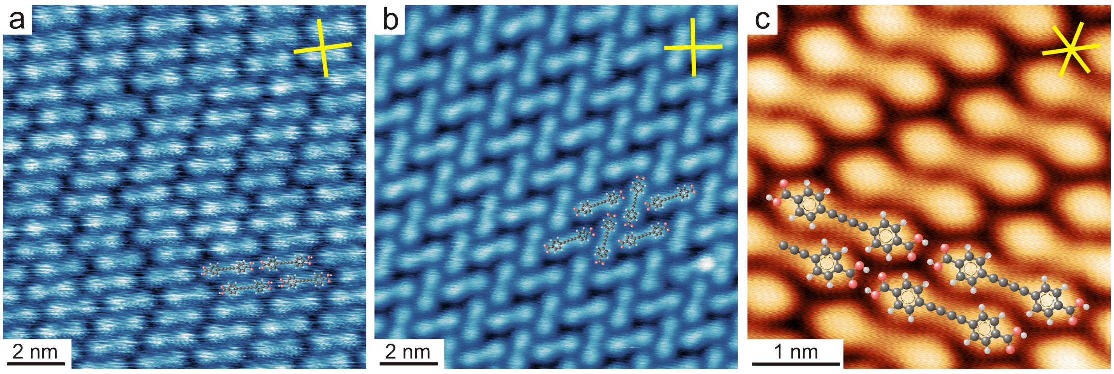

Figure 3.3: STM images of the molecular phases of BDBA on (a,b) Ag(100) and (c) Au(111) surfaces. At room temperature domains form where the molecules align parallel to the chains (a,c). After annealing above 430 K on Ag(100) BDBA deprotonates and a structure transition occurs (b). Yellow lines mark the close-packed directions of the surface. (Image parameters: (a) - 1.2 V, 0.2 nA, 297 K; (b) - 1.3 V, 0.2 nA, 297 K; (c) 0.8 V, 0.3 nA, 297 K).

to the structure observed in Ref. 103. We ascribe this to the thermally induced deprotonation of the carboxylic acid groups.[104] Here, the strong carboxylate-phenyl ionic hydrogen bonding[104] and the carboxylate-carboxylate repulsion govern the overall appearance of the observed structure. The BDBA molecules are stable up to 500 K, beyond this temperature only disordered polymer-like features are observed.

On the Au(111) surface, only the linear BDBA phase was found even after annealing the sample at 450 K (Figure 3.3c). The measured periodicity of 19.6 Å within the molecular chains is lower compared to the Ag substrate (20.2 Å). Since adjacent carboxylic acid groups are closer together (O-HO distance is 3.8 Å for Ag and 3.1 Å for Au), stronger hydrogen bonding between the molecules within the chains is expected. On both surfaces the BDBA was always imaged as a straight and elongated protrusion even after deprotonation on the Ag surface.

3.1.2 BDBA-MOCNs on Au(111) and Ag(100)

The MOCN preparation method applied in this work is illustrated in Figure 3.4. Accordingly, BDBA was deposited continuously from a quartz crucible heated to 560 K in a time range of 7 - 9 minutes (t_{BDBA}) on the metal substrate. During the deposition the substrate was kept at an elevated temperature in the range of 450 - 460 K. Iron atoms were simultaneously deposited from an electron-beam heated evaporator in homogeneously distributed 7 - 9 intervals of 20 - 30 seconds (t_{Fe})

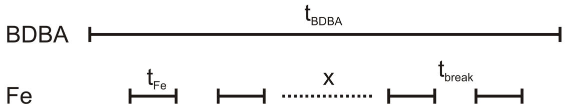

Figure 3.4: Illustration of the applied MOCN preparation scheme. Continuous BDBA deposition for t_{BDBA} = 7 - 9 minutes at substrate temperatures of 450 - 460 K. Fe deposition distributed homogenously in 7 - 9 intervals of 20 - 30 seconds with equal deposition breaks (t_{break}).

interrupted by time intervals t_{break} where the shutter of the metal evaporator was closed. After completing the BDBA and Fe deposition, the substrates were kept at 450 - 460 K for three minutes and subsequently cooled down to room temperature with $\sim$ 0.5 K/s. As a result, regular MOCNs with metal-to-molecule concentration ratios of 1:1 were obtained while the formation of disordered or locally unsaturated network parts was rarely observed. Regular networks were also observed when molecule and metal deposition were carried out consecutively. While network adaption to terrace steps and at network domain boundaries were still observed the overall quality of the network formation improved when both constituents were deposited simultaneously.

Figure 3.5a and 3.5c depict two representative STM images with 2D-MOCNs on Au(111) and Ag(100) surfaces, respectively. The network formation is controlled by the metal-to-molecule concentration ratio as described before. At the employed Fe:BDBA ratio of 1:1, fully reticulated network structures form comprising iron dimers at the network nodes as demonstrated in Figure 3.5b. At each network node four BDBA molecules coordinate with their carboxylate groups to Fe adatoms in two different modes. Two BDBA molecules bridge the diiron unit symmetrically while each of the other two axial ligands forms bidentate bonds to one Fe atom of the dimer. An asymmetric configuration with monodendate axial ligands was also observed. Similar networks and binding motifs were reported in previous works on Fe-carboxylate coordination systems.[33,105–107] However, in contrast to previous findings the orientation of the Fe dimers shows a mixed phase of parallel and alternating arrangements with no strict periodicity. Rarely, highly regular sections of the BDBA-Fe MOCN on Au(111) were observed as shown in Figure 3.6. In this case, the adjacent iron atom dimers (Fe-Fe spacing $\sim$ 3.6 Å) show a parallel orientation. At each network node four BDBA molecules coordinate with their carboxylate groups to Fe adatoms in two different modes. Two BDBA molecules bridge the diiron unit symmetrically while the other two ligands form axial bonds to the Fe dimer.[11,106,108] The majority of the axial linkers bind with two oxygen atoms to an Fe adatom, but an asymmetric configuration with only one oxygen atom binding to the Fe adatom is also observed occasionally. The resulting MOCN

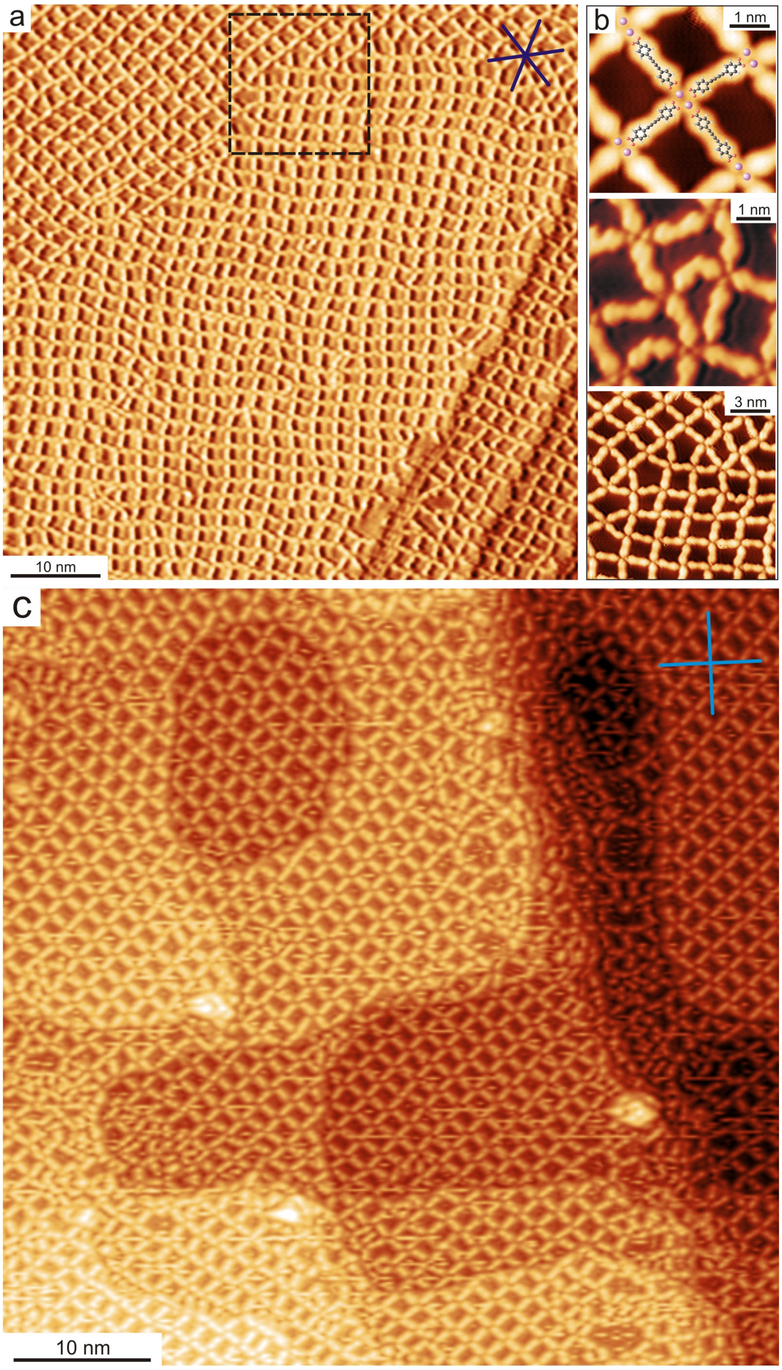

Figure 3.5: Representative STM images of BDBA-Fe MOCNs. The close-packed substrate directions are indicated by blue crosses. (a) Au(111). Individual network domains adapt both at surface steps and on terraces. (b) The left image shows a regular network with the central di-iron binding motif. The middle image shows ligands in a bent configuration. The right image shows the mutual adaptation of two domains on the same terrace. The conformational adaptation of the molecules and the formation of irregular triangular and pentagonal network structures can be observed (Au(111), 5 K, -0.6 V, 0.3 nA). (c) Ag(100). The MOCN is formed over multiple step edges of various shapes and adapts to subtle substrate variations (297 K, -0.9 V, 0.08 nA).

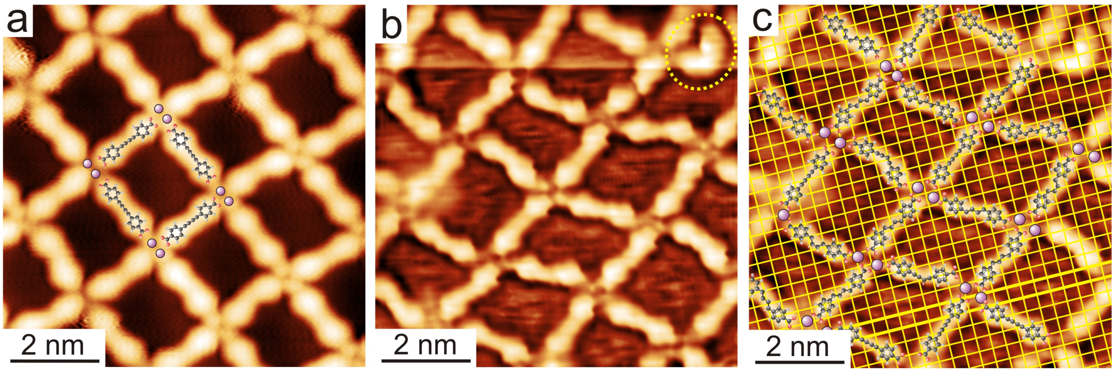

Figure 3.6: (a) High-resolution STM topography of a BDBA-Fe MOCN on Au(111) (-0.6 V, 0.3 nA, 5 K). A tentative model is superposed. (b) BDBA-Fe network on Ag(100) (0.8 V, 0.3 nA, 5 K). The ligands appear in different conformations as illustrated in the tentative model in (c).

can be characterized by a rectangular unit cell as indicated in the tentative model in Figure 3.6a. Figure 3.6b illustrates the ligand adaptability within the MOCN. The BDBA molecules exhibit different conformations in the BDBA-Fe MOCN on Ag(100), e.g., strongly bent ligands were observed as highlighted in Figure 3.6b. In Figure 3.6c, a tentative model is given for the observed BDBA-Fe network. Apart from the conformational degree of freedom of the BDBA ligand, the iron atoms appear to have variable positions relative to the substrate lattice and presumingly adapt their orientations to enable the MOCN formation.

Apart from the similarities of the local structural details of the networks with other Fe-carboxylate systems, the BDBA-Fe MOCNs exhibit a high insensitivity to step edges of various shapes and orientations, i.e., the network extends over surface steps without breaking the network integrity. At the step edges, BDBA-Fe domains originating from adjacent surface terraces mutually adapt in-phase resulting in the extension of the network structure over multiple surface steps (cf. Figure 3.5a and 3.5c). The Fe dimer orientation, spacing, and local ligand arrangement exhibit a broad range of geometries that becomes apparent in Figure 3.5b. The BDBA is capable of undergoing internal conformational changes as demonstrated in the middle and right image of Figure 3.5b. Here, several ligands are strongly bent while coordinating to iron atoms in the network. In addition, network triangles and pentagons can be identified at the domain interfaces. The strong variations of the ligand adsorption geometry deviating from the high-symmetry directions of the underlying surface are accompanied by a high degree of flexibility at the coordination centers of the network.[86] These highly irregular transition structures of the ligand as well as the flexibility of the coordination bonding enable the mutual adaptation of BDBA-Fe domains growing on the same terrace with different orientations.

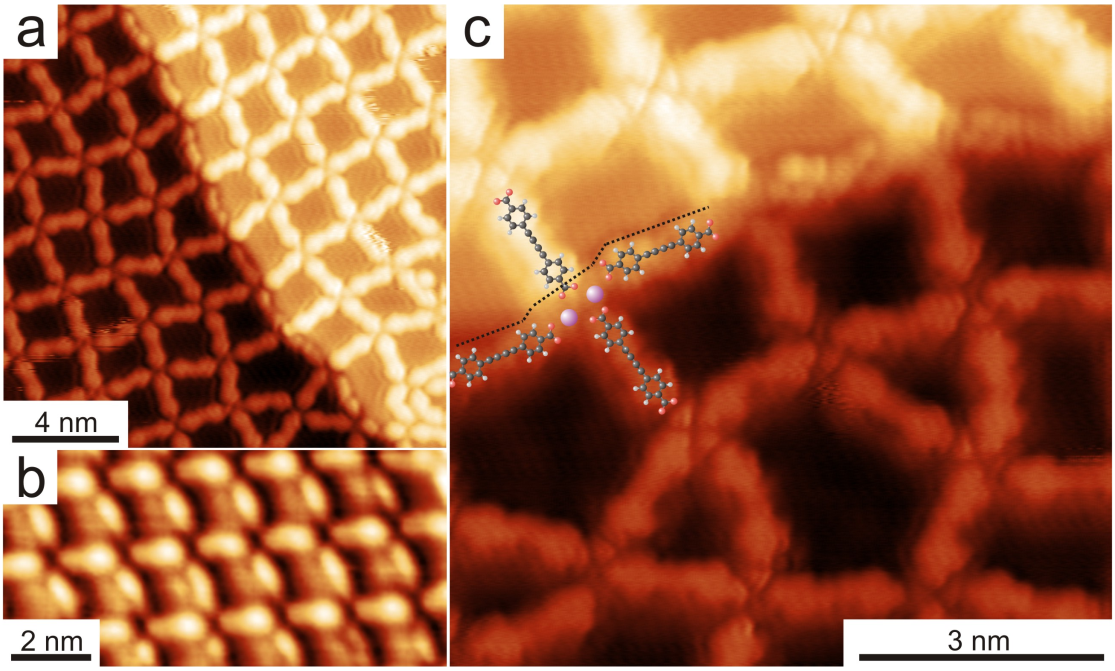

Figure 3.7: High-resolution STM topographs of BDBA-Fe MOCNs. (a) Fully reticulated network crossing a Au(111) step (5 K, 0.8 V, 0.7 nA). The domains at the lower and upper terrace mutually adapt and merge in-phase at an irregularly shaped step edge. Iron dimer centers were resolved except at the direct step edge region. (b) Continuous BDBA-Fe network on a rugged Ag(100) surface (5 K, -0.9 V, 0.5 nA). (c) BDBA-Fe at a Au(111) step edge (5 K, 0.8 V, 0.3 nA). The submolecular resolution exhibits the configurational degree of freedom of the edge molecules.

Both, the flexibility of the metal-ligand bond and the conformational freedom of the molecules result in an overall fully reticulated network that lacks strict 2D periodicity. In contrast to the metal-ligand bond flexibility found in heteroleptic MOCNs[86] the error tolerance and adaptability of the presented homoleptic network are a consequence of the high flexibility of the chemisorbed ligands and shows, in contrast to former works, also high insensitivity to step edges as presented in the following.[33,86,105,106]

Figure 3.7 demonstrates in more detail the flexibility and adaptability of the BDBA molecules at Au(111) and Ag(100) step edges. Figure 3.7a shows an MOCN extending over a step edge. BDBA decorates the step edge with its long axis oriented along the step direction at the lower side of the step. Ligand molecules of adjacent terraces point to a common network node across the step edge with the upper ligand apparently extending over the step. The variations in the apparent heights of the ligands in the STM images in Figure 3.7a and 3.7c indicate that the step molecules can adopt different configurations. We interpret this observation as

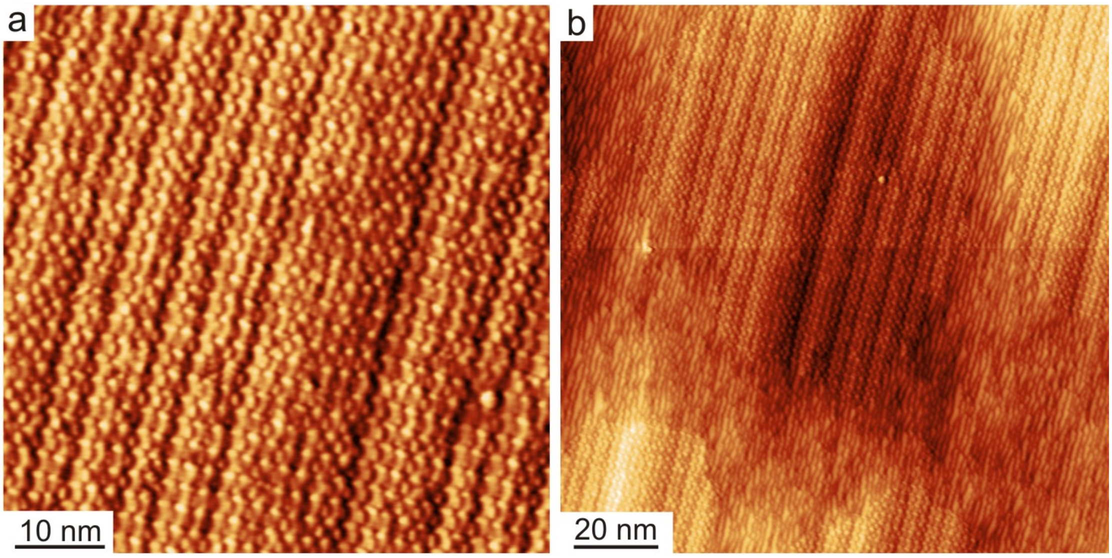

Figure 3.8: (a, b) STM images of a single domain and an overview of BDBA-Fe networks on Ag(100) (5K, 0.5V, 1nA). Terraces appear to be restructured for the accommodation of an integral number of BDBA molecules which each coordinating to iron dimers. Between the network domains the surface is very rough consisting of many small nanometer sized terraces.

the molecules' ability to reside flat at the lower side of the step or, when closer to the step, to adopt a tilted or bent configuration. Figure 3.7b illustrates the ability to form continuous networks on a rugged Ag(100) surface. A fully reticulated MOCN extending over multiple steps was observed. However, it is likely that during the network formation the steps are reconstructed on the Ag(100) surface. Figure 3.8 shows BDBA-Fe network domains on a rugged area of the Ag(100) surface. In addition to the data shown in Figure 3.7d, also terraces with a width of two and more crossing BDBA ligands were observed. The area between the domains is very rough comprising many irregular nanometer sized terraces. The MOCN formation process appears to strongly reshape the area under the network which is indicated by the presence of larger sized terraces and straight terrace steps. With an increasing number of BDBA ligands accommodated on each terrace, the internal flexibility of the whole MOCN increases and consequently the network adaption to the substrate becomes more and more dominant. Most processes concerning Ag atoms on Ag(100) surfaces (e. g. diffusion, vacancy formation, ...) have an activation energy below 0.5 eV, so they are easily activated even at room temperature. To optimize the formation of mesoscale MOCNs, the influence of particular crystallographic surface terminations of the substrates on the ability of both surface reshaping and network adaption needs to be further studied.

As demonstrated above, the BDBA exhibits a high degree of conformational and orientational flexibility. The ability of the BDBA to assume different adsorption geometries including strongly bent and titled configurations is ascribed to its butadiyne backbone. In general the sp bonded alkynyl structure exhibits only limited bond angle flexibility. However, the asymmetric interaction of the orthogonal π-orbitals with the surface may lead to a partial rehybridization including higher sp^n orbitals, thus altering the 180° bond angle. A potential charge transfer to the π^* orbital could effectively lower the bond order of the alkyne carbon atoms. On the other hand, in the absence of Fe atoms the pristine BDBA molecule does not exhibit variations from its rod-like shape. In this case, neither intramolecular bending nor strong adsorption site variation were observed on both Ag(100) and Au(111) surfaces (see before).[109] The estimated binding energy for Fe-carboxylate networks in similar 2D configurations amounts to about 1.2 eV per bond.[34] We reason that the energy gain from the coordination bond formation overcompensates the energy expense for the bending of the molecules, thus enabling the adaptation ability of the network.

The position and orientation of the Fe dimers and ligands relative to the substrate lattice is determined by the dominant BDBA-Fe coordination. The network structure exhibits a broad range of nonequivalent adsorption sites and orientations for both the iron dimers and ligands. This is a result of many different possible bonding and adsorption configurations that are energetically accessible. These observations are in contrast to Fe-carboxylate networks with rigid polyphenyl ligands, where the network orientation, molecular adsorption, and the position of the iron atoms is well determined with only little structural variations.[34, 105, 107] However, the use of a less rigid 2-fold coordination motif can result in highly flexible 1D chains.[97] The statistical analysis of the ligand orientations within the MOCNs on Au(111) and Ag(100) is presented in Figure 3.9. It shows a BDBA-Fe network on Au(111) used for analyzing the BDBA orientations that were measured in two different ways: the first direction is defined by the center-to-center axis of the two corresponding BDBA phenyl rings and the second direction is defined by the node-to-node axis between the diiron centers. The result is presented in Figure 3.9b. The mean ligand orientation forms an angle of about 14° with the surface principal direction marked in red in Figure 3.9a. Furthermore, the histogram shows a relatively broad distribution of the ligand orientations. Due to the possible ligand bending upon the coordination to iron atoms, the angular distribution of the ring-to-ring directions (indicated in red and black in Figure 3.9b) is somewhat broader compared to the node-to-node directions. Figure 3.9c further shows a BDBA-Fe MOCN on Au(111) used for the Fourier analysis of the mean ligand orientation (Fourier scheme shown in Figure 3.9e). The broad spots in the Fourier transformed image (Figure 3.9d) yield a ligand orientation range of about 25° in accordance with the statistical analysis (Figure 3.9b) where the width of the angle distribution for the node-to-node direction amounts to 25-30°. In the Fourier image also small dots appear close to the center that are due to the herringbone reconstruction of the underlying Au(111) surface. The surface reconstruction has no apparent effect on the BDBA-Fe network growth. For the BDBA-Fe network on Ag(100) shown in Figure 3.9f, the ligand orientation deviates approximately 45-50° from the surface unit vector indicated in red. These observations show that, in contrast to a large number of previously observed systems, the underlying substrate lattice does not strictly define the ligand orientations within the obtained MOCNs.

The crossing of the network structure at the step edges follows predominantly one motif as indicated by the tentative model of the local configuration superposed in Figure 3.7c. Two axial ligands are generally adsorbed directly parallel at the step edge. The two molecules perpendicular to the step form bridging bonds to the Fe dimer with the upper ligand extending somewhat over the terrace step which is enabled by the flexibility of the ligand backbone. In previous work ditopic rodlike dicarboxylic acids also extend with the carboxyl moiety over the step edge. In that case however, the carboxylic acid remained protonated forming hydrogen bonded molecular chains with no metal adatom involved in the bonding.[92] Here, we can rule out the possibility of protonated molecules by the presence of reactive Fe metal adatoms and thermally induced deprotonation of the carboxylic group upon annealing. The in-phase crossing of surface steps was not observed for related Fe-polyphenyl carboxylate networks, which we ascribe to the low flexibility of these ligands.[33,86,87,105–107] The variations in the Fe dimer configurations are inherently linked to their imaging by STM. Even under suitable tip conditions, parts of the MOCN with visible iron dimers coexisted with network parts where the iron could not be resolved. We ascribe this to local electronic differences due to different coordination geometries. In this context, the iron centers were not resolved in the direct step edge region. However, we expect the presence of iron dimers in the coordination nodes at the lower side of the step edges from the analysis of the ligand arrangement and distances. At the step edge, the metal-ligand bond distances for both the bridging and axial molecules are in accordance with corresponding distances found on surface terraces (further analysis see below).

In the absence of iron atoms, i.e., in the molecular phase of BDBA, this bonding motif and step edge crossing was never observed, neither on terraces nor at step edges of Ag(100) and Au(111) surfaces (see before). The necessity of iron atoms indicates that neither silver nor gold adatoms are incorporated in the MOCN nodes. In comparison to the hydrogen-bonded one-dimensional molecular chains,

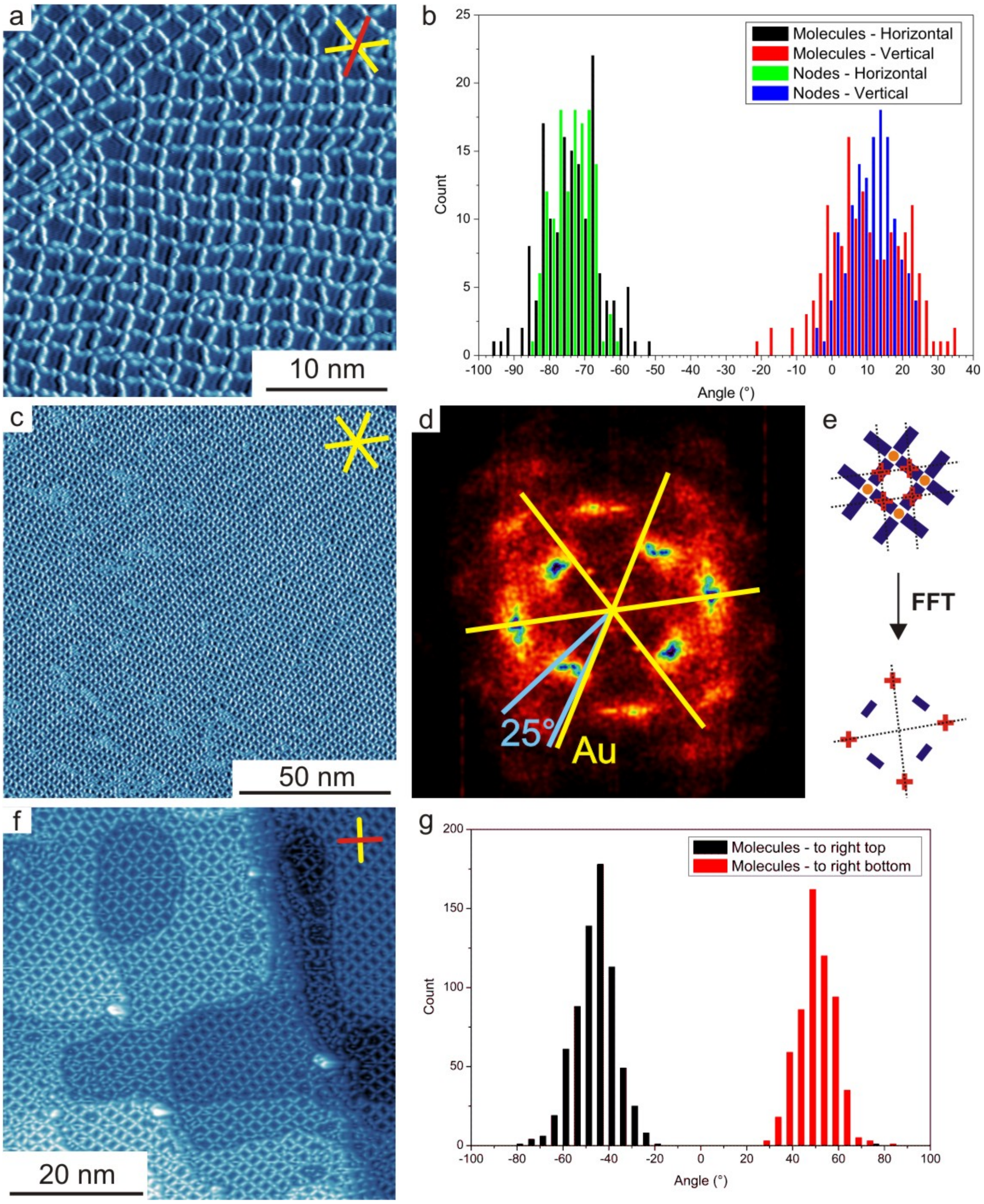

Figure 3.9: (a) STM topography of the BDBA-Fe MOCN on Au(111) used for the statistical analysis of the ligand orientation relative to the red substrate direction (5K, -0.6V, 0.3 nA). (b) Histogram of the ligand orientation in (a) obtained in two ways: center-to-center axis of the BDBA phenyl rings and node-to-node axis between the diiron centers. (c) BDBA-Fe MOCN used for Fourier analysis (d) of the network growth direction on Au(111) (5K, -0.6V, 0.3 nA). Following Fourier transformation (e) the ligand angle distribution amounts to 25°. (f) BDBA-Fe MOCN on Ag(100) (297 K, -0.9V, 0.08 nA) with the ligand orientation statistically analyzed in (g).

density functional theory calculations show that the binding energy is dominated by hydrogen bonds with interaction strengths larger than the inclusion of substrate adatoms or step atoms.[92] With respect to metal-ligand interactions this supports the incorporation of iron atoms in the coordination nodes and the exclusion of surface adatoms in the nodes.

It is interesting to see the behavior of the structures at different stoichiometric Fe:BDBA ratios. The fully reticulated iron dimer motif (Fe:BDBA ratio 1:1) resolved on both Ag(100) and Au(111) surfaces is consistent with coordination motifs observed in previous works, in which iron atoms and carboxylate ligands were employed.[11,33,106] We performed in depth STM studies of the MOCNs and its coordination centers also at metal-to-ligand concentration different from 1:1. Upon co-deposition of BDBA with lower amount of iron (Fe:BDBA ratio 2:3) on Ag(100), double-row Fe-BDBA network structures were obtained as presented in Figure 3.10. The BDBA molecules within the rows are bound together by coordination bonds to single iron atoms, which are clearly resolved in Figure 3.10b. The Fe atoms in those double-row structures are positioned off the central chain axis of the rows and are stabilized by perpendicularly arranged bridging BDBA molecules. Within the double rows, the molecules in neighbouring rows are presumably bound together by phenyl-carboxylate hydrogen interaction as in the case of the molecular linear BDBA phase. Increasing the Fe:BDBA ratio over 1:1 results in the formation of iron clusters (not shown) on Ag(100). On Au(111) at the same low Fe:BDBA ratio, the double row networks were not observed. Instead, fully reticulated BDBA-Fe single row networks coexisted with the pure molecular phase described before. At a Fe:BDBA ratio higher than 1:1, the single row BDBA-Fe networks coexisted with a completely new phase (Fe:BDBA ratio $\sim$ 2:1) which is depicted in Figure 3.11. Large domains were formed with molecules arranged side by side in extended rows. The high-resolution image (Fig. 3.11b) reveals that molecules in neighbouring rows are bound together by coordination bonds via iron atoms, which are, however, barely visible. In addition, we presume that the parallel alignment of molecules within the rows is due to incorporation of additional Fe adatoms since the shape of the molecules bends slightly from a perfect rod-like shape.

As no binding motifs similar to network nodes shown in Figures 3.6, 3.10, and 3.11 were observed for the pure molecular systems on both substrates, the incorporation of substrate adatoms (i.e. Ag and Au) in the network coordination nodes is very unlikely. The incorporation of Fe dimers in the coordination nodes (Fe:BDBA ratio 1:1) at the surface step edges seems highly probable by further analysis of the metal-ligand bond distances. The measured phenylphenyl distance of two axial BDBA ligands across the coordination node is (15.1 ± 0.2) Å, which fits with

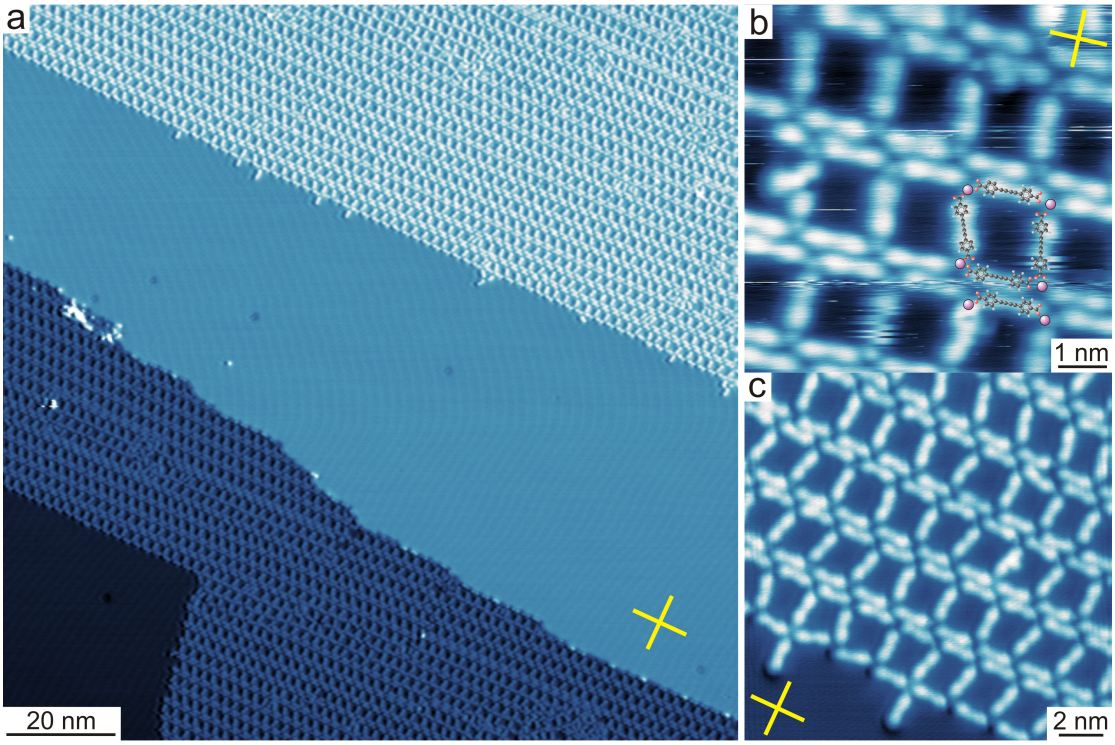

Figure 3.10: (a) STM image of an overview of the double row Fe-BDBA network on a Ag(100) surface and close views with structure model (b,c). The close-packed substrate directions are indicated by yellow crosses. (Image parameters: a) 0.7 V, 1.0 nA, 5 K; b) -0.8 V, 0.05 nA, 297 K; c) 0.2 V, 1.0 nA, 5 K)

the corresponding distance of (15.2 ± 0.2) Å measured on surface terraces. In comparison, the phenyl-phenyl distance of two bridging ligands is (11.1 ± 0.2) Å and the phenyl-phenyl distance of hydrogen bonded BDBA molecules is (10.0 ± 0.2) Å, i.e. much smaller than the one observed at the step edge. The BDBA molecules are predominantly orientated perpendicular to the step edges. This lower variability in the observed angles is a typical feature of coordination node bridging ligands. On the Ag surface, the energetically optimal position of iron atoms is to be embedded in the first substrate layer. In order to form coordination bonds, the iron atoms need to be raised to adatom position. At the step edge, the situation is half way in between and favorably the iron atoms are directly attached to the step edges. A similar argument would hold also on Au(111) where the Fe adatoms preferably nucleate at the elbow sites of the herringbone reconstruction and the step edges.

Upon thermal activation during the MOCN formation process the Ag(100) surface morphology appears to be reconstructed in certain areas (cf. Figure 3.7b).[110] On each terrace a single BDBA molecule coordinates with its carboxylate groups to

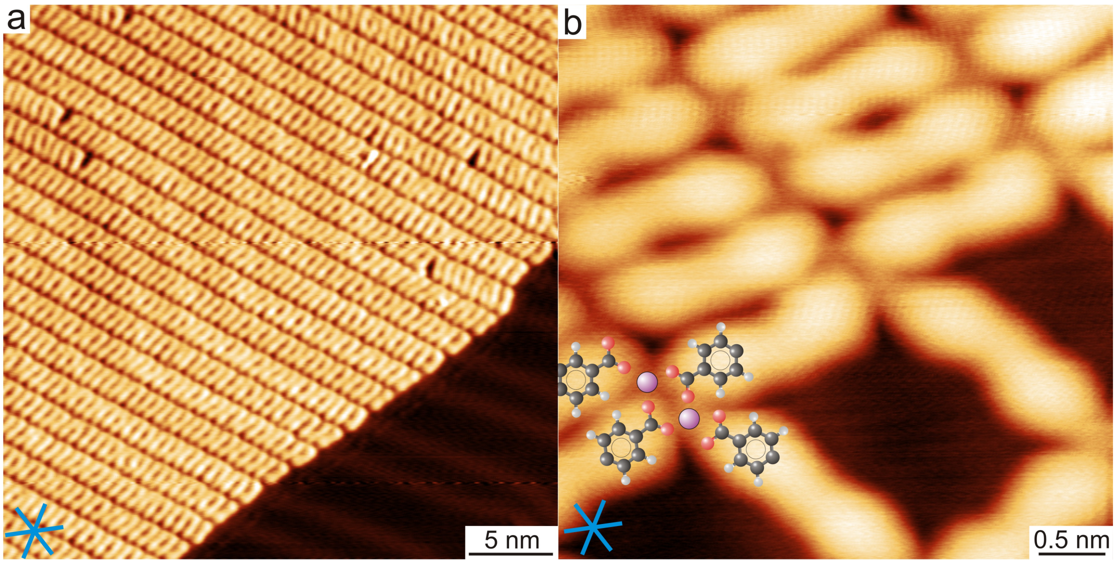

Figure 3.11: (a,b) STM images of the Fe rich phase on Au (111). The underlying substrate orientation is marked by blue stars. (Image parameters: a) 1.0 V, 0.5 nA, 5 K; b) 0.5 V, 1.0 nA, 5 K)

iron dimers at opposite steps. Although this configuration is only rarely observed, the terraces appear to be modified for the accommodation of one molecule. The metal-ligand interactions are hereby combined with the surface reshaping (see before). It is worth noting that the MOCNs on both Au(111) and Ag(100) surfaces are robust against annealing to at least 490 K.

In conclusion, we have demonstrated the self-assembly of extended metal-organic coordination networks, which grow continuously over multiple surface steps showing a high degree of insensitivity and adaptability to intrinsic surface defects. This is enabled by the conformational flexibility of the butadiyne backbone forming bond angles far from ideal, hence conferring a high degree of error tolerance to the ligand molecules. Our findings are valid on both silver and gold substrates with different surface symmetries. Further, the MOCNs are distinguished by their considerable thermal robustness. The high degree of substrate error tolerance of the MOCNs enables the realization of large-scale 2D-MOCNs. Particularly, our findings open up the way to pattern also rough and imperfect surfaces, e.g., small crystallites, with regular and thermally stable metal-organic structures. These MOCNs with high surface coverage can be further functionalized for diverse applications by making use of the butadiynyl moieties for the selective binding of guest species.

3.2 Functionalization of 2D-MOCNs

The self-assembly protocols developed in the field of supramolecular chemistry are widely employed to engineer complex molecular architectures and materials with tailored properties.[25,26,111–117] In particular, bulk metal-organic frameworks (MOFs) and other porous compounds are highly versatile materials[31,32,116–118] that can be utilized, e.g., for gas storage[119] or heterogeneous catalysis.[120] Only recently, the interest has shifted also toward MOF films, thereby expanding and enhancing their applicability to membrane separators, chemical detectors, optical applications, and quartz crystal microbalance devices.[121,122] In the two-dimensional limit, metal-organic architectures as well as hydrogen-bonded networks confined to single-crystal metal surfaces have been intensively studied for gaining fundamental insights into the substrate governed self-assembly phenomena[27,82,123] as well as to investigate their potential in the fields of surface patterning,[124] catalysis,[37] and organic-based magnetism.[89]

Functionality in materials is often achieved by incorporating particular molecular or inorganic components into the framework that do not necessarily serve as building blocks in the primary structure (see Introduction)). At surfaces, molecular networks were tested for their suitability to serve as host-guest systems[81] and as templates to steer the adsorption and organization of secondary ligands[124] and metal atoms and clusters.[125,126] However, the thermal stability of the latter proved to be challenging. Further, the metal decorated networks and templates have so far not been used to incorporate ligand molecules at a second stage of organization.

Here, we demonstrate the selective incorporation of Ni atoms and clusters into two-dimensional metal-organic templates on Ag(100) and Au(111) surfaces that allows to coordinate additional molecules into the open structure. The host coordination network self-assembles from bifunctional ligands (BDBA, Figure 3.1) and Fe atoms and provides a robust and flexible matrix.[127] Scanning tunneling microscopy reveals the selective interaction of Ni atoms with the Fe-BDBA network. Depending on the substrate, Ni atoms decorate either the benzene rings (Au) or the butadiyne moiety (Ag) of the ligand, while the network remains thermally stable up to 450 K. The striking difference in the Ni binding behavior reveals that besides selective Ni-ligand interactions also the substratedependent Ni atom diffusion processes play a role in the network functionalization. The incorporation of additional ligands into the network cavities coordinating to Ni atoms enables the assembly of robust architectures at different organizational stages.

All experiments have been carried out in two separate UHV chambers (base pressure $\sim 2 \times 10^{-8}$ Pa) hosting a home-made variable-temperature STM and a low-temperature STM (5 K) and standard tools for preparation of well-defined metal surfaces. Clean Ag(100) and Au(111) surfaces were prepared by cycles of Ar^+ sputtering and annealing to 800 K, followed by a slow substrate cooling to room temperature. The metal-organic networks were prepared by simultaneous deposition of Fe atoms and BDBA molecules on the substrate held at 450 K.[127] The BDBA molecules were deposited by thermal evaporation from a quartz crucible held at the temperature of 560 K and metal atoms using a standard e-beam evaporator (see Section 1.2) at a flux current of 1 nA. During the deposition (5 - 15 min) the pressure was lower than 2×10^{-7} Pa. Ni atoms were deposited by a second e-beam evaporator on the substrate held at room temperature (300 - 305 K). The samples were then directly transferred to the respective STM. The STM images were acquired either at room temperature or 5 K using electrochemically etched tungsten tips with a sample bias in the range from - 1.0 to + 1.2 V and tunneling currents ranging from 0.06 to 1.0 nA.

In Section 3.1, the formation of extended Fe-BDBA coordination networks on both Ag(100) and Au(111) surfaces was demonstrated, showing a high degree of structural flexibility and adaptability. In this section, the BDBA-Fe MOCNs were prepared in the same way. As shown before, the iron atoms interact exclusively with the carboxylate oxygen atoms leaving the butadiyne moiety virtually free, which serves as anchoring sites for transition metal atoms with high π-electron affinity, e.g., Ni. The Ni atoms can be utilized to bind additional ligands and functional units to the host network. Further, low-valent Ni atoms are potential active sites for CO_2 conversion.[128]

3.2.1 Ni decoration of Fe-BDBA on Au(111)

Figure 3.12 presents STM images of the Fe-BDBA network on Au(111) after subsequent nickel deposition at room temperature followed by cooling to 5 K. The BDBA ligands appear as dumbbell-like protrusions with an apparent height of 1.51 ± 0.04 Å at the benzene ring and 1.31 ± 0.04 Å at the center of the molecule, which is independent of the applied bias voltages (from -1.0 to +1.2 V). Upon Ni deposition the following features are identified in the STM images: (1) decoration of the benzene rings and (2) partial or complete filling of the network cavities.

The blue circle in Figure 3.12a marks a small protrusion at the benzene rings with an apparent height in the range 1.9 - 2.1 Å. The high-resolution image depicted in Figure 3.12b and the averaged line profile (blue) in Figure 3.12c reveal a small asymmetry with respect to the long axis of the ligand. The somewhat larger features (marked by a green square in Figure 2a) have an apparent height of 2.2 - 2.5 Å, and their appearance extends from the benzene ring further to the center or over the entire molecule. The corresponding line profile (green) is shown in Figure 3.12c. We attribute all of these analyzed features to the presence of Ni atoms and small clusters which bind to the organic backbone of the network (see below).

Figure 3.12d shows a high-resolution image of a filled cavity, which apparent height of 2.0 - 2.6 Å at the center is close to the apparent height of Ni clusters on the bare Au(111). The position of the filled cavities correlates with the elbow sites of the herringbone reconstruction, which remains intact under the network as shown in Figure 3.13. It shows STM images of a Fe-BDBA network together with the bare Au(111) surface. On the clean Au(111) surface, Ni clusters aggregate in the vicinity of elbow sites of the herringbone reconstruction.[129] The positions of the

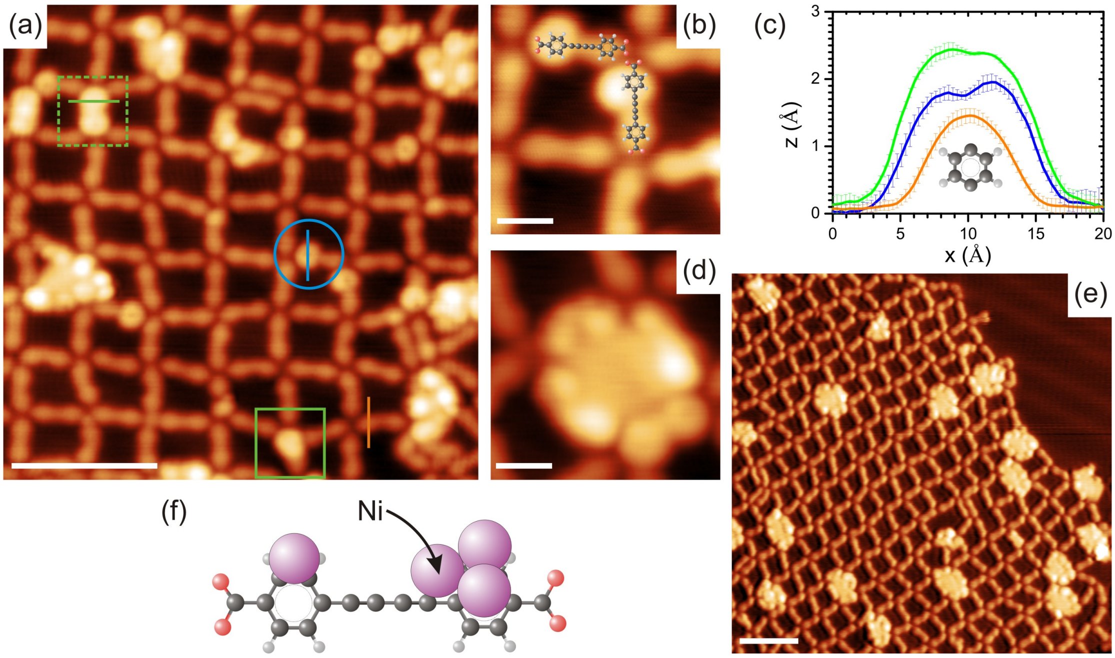

Figure 3.12: Representative STM images acquired after Ni deposition at 300 K on the Fe-BDBA network on Au(111). (a) Typical Ni-induced features near the benzene rings (blue circle, solid square) or entire BDBA (dotted square) are highlighted. (b) High-resolution image of the decorated benzene rings with superimposed BDBA model. (c) The average profiles (with 1σ error bars) corresponding to the line colors in (a). (d) High-resolution image of a filled cavity. (e) Upon annealing to 385 K only the filled cavities remain. (f) Model of possible binding sites of the Ni atoms to BDBA. Acquisition parameters: -0.2 V, 1 nA, 5 K (a, b) and +0.5 V, 1 nA, 5 K (d, e). Scale bars: 5 nm (a, e) and 1 nm (b, d).

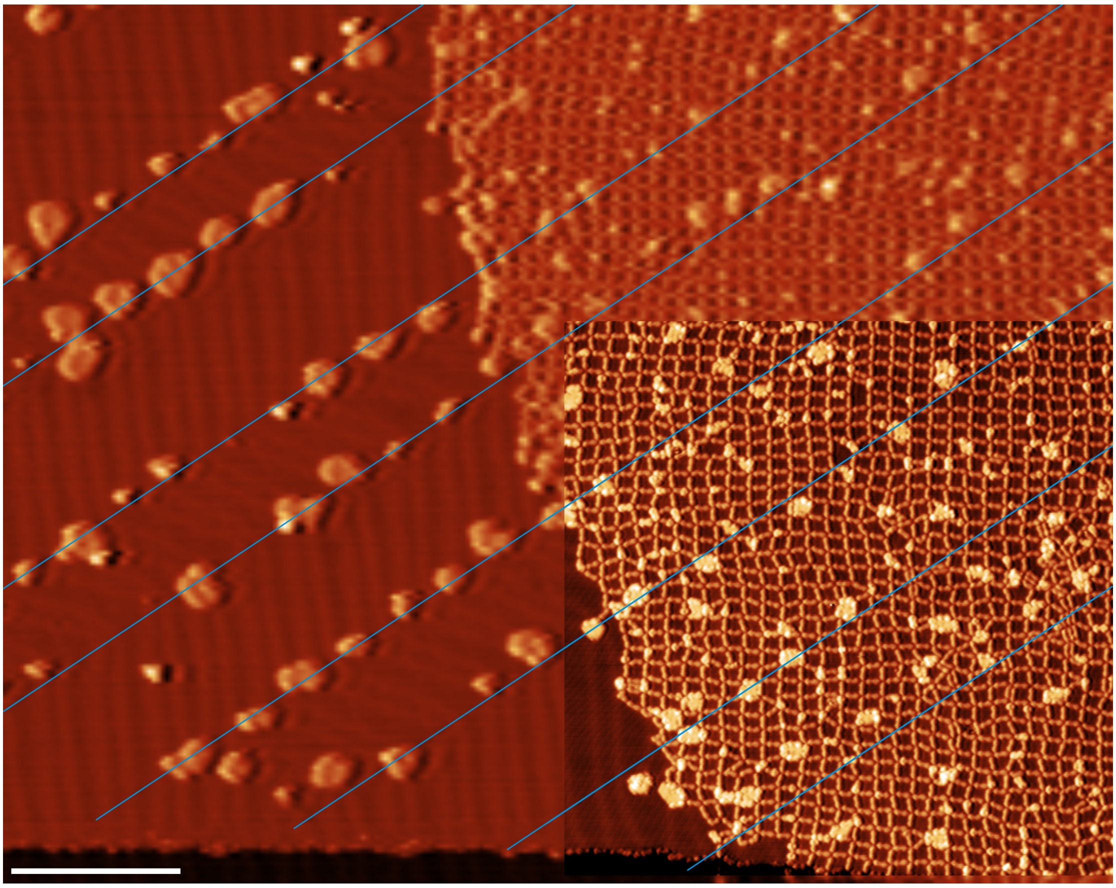

Figure 3.13: Superposed overview and high-resolution STM images showing Ni clusters that aggregate at elbow sites of the Au(111) herringbone reconstruction on the bare surface and within the Fe-BDBA network. Acquisition parameters: +0.5 V, 1 nA, 5 K (overview) and -0.2 V, 1 nA, 5 K (inset); Scale bar 20 nm.

elbow sites are marked by the lines in Figure 3.13.

Annealing to 385 K leads to the removal of the small features at the organic backbone, and only completely filled cavities remain within the networks (Figure 3.12e). After this treatment, the filled cavity interior shows a uniform height that corresponds to the formation of Ni islands with a height of monatomic Ni layer (2.1 - 2.4 Å).

3.2.2 Ni decoration of Fe-BDBA on Ag(100)

The incorporation of Ni atoms into the Fe-BDBA network on Ag(100) after deposition at room temperature followed by sample cooling to 5 K is illustrated in Figure 3.14. The apparent height of the pristine BDBA ligand on the Ag(100) surface is

1.01 ± 0.01 Å at the benzene ring and 0.93 ± 0.01 Å at the center. The following changes upon Ni deposition are observed: (1) lowering of the central part of the BDBA molecule, (2) appearance of protrusions near the ligands, and (3) filling of the network cavities.

The red circles in Figure 3.14a mark a large fraction of BDBA molecules (termed ω-BDBA) that display a bias-independent apparent height of 0.88 ± 0.07 Å at the benzene ring and 0.53 ± 0.05 Å at the central part of the ligand. The corresponding averaged line profiles are plotted in Figure 3.14b. The variation of the ω-BDBA profile is considerably larger compared to the pristine ligand, suggesting that a range of distinct configurations contribute to the appearance of the ω-BDBA molecules. The high-resolution images presented in Figure 3.14c,d reveal that some

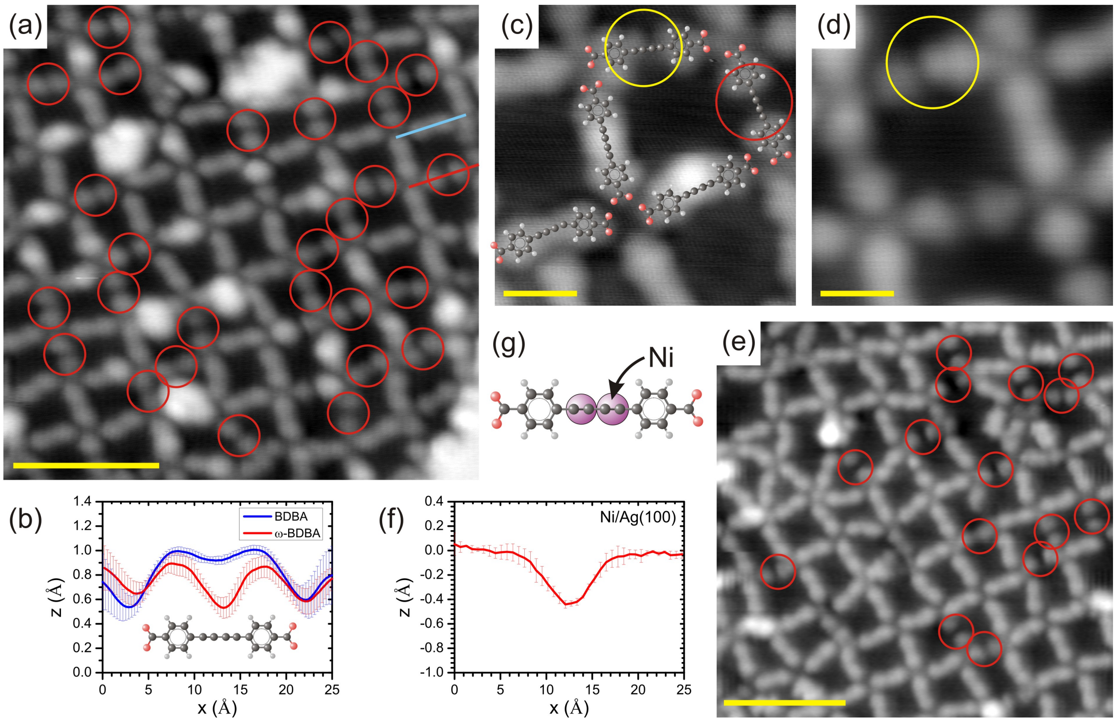

Figure 3.14: STM topographs of a Fe-BDBA/Ag(100) coordination network after Ni deposition at room temperature (a, c, and d) and after subsequent annealing to 450 K (e). (a) Red circles mark BDBA ligands with a pronounced depression at their centers (ω-BDBA). (b) Average profiles of pristine and ω-BDBA marked by color-coded lines in (a) with 1σ error bars. The magnified images (c) and (d) show the observed features in greater detail with the superimposed molecule model. (e) Only the ω-BDBA features remain after annealing to 450 K. (f) Line profile of a Ni atom embedded in the first Ag substrate layer. (g) Proposed trapping site of Ni atoms underneath the ligand molecules. Acquisition parameters: 5 K, 1 nA, +0.5 V (a, e), +0.7 V (c), and +0.2 V (d). Scale bars: 5 nm (a, e), and 1 nm (c, d).

of the BDBA molecules display an asymmetry along the long axis with one benzene ring being lower than the other. Further, the apparent height at the center of the molecules can be as low as 0 Å. We attribute the dark features to Ni atoms residing underneath the molecules (see below).

Figure 3.14a shows additional relatively large protrusions with measured heights in the range of 1.4 - 2.2 Å that are tentatively attributed to metal clusters. These features are predominantly located near the central part of the ligands, and only a minority of clusters is found near the benzene rings. Also on Ag(100) some of the network cavities are completely filled with an apparent height of 2.05 Å that matches exactly the Ag substrate step height. As will be discussed below, both clusters and islands are composed of Ag atoms. Apart from the decoration of the network, rectangular metal ad-islands were found on the bare Ag surface as discussed below.

Annealing to 385 K leads to a reduced amount of clusters decorating the network and an accompanied increase in the size of the metal ad-islands on the bare surface. Further annealing to 450 K removes nearly all cluster features inside the network with only ω-BDBA features remaining at the same abundance (Figure 3.14e).

3.2.3 Ni deposition on bare Ag(100)

Figure 3.15 shows STM images of the bare Ag(100) surface after Ni deposition at room temperature. The apparent depressions marked by orange, red and green circles in Figure 3.15a are associated with Ni atoms embedded in the first substrate layer.[130,131] The corresponding average line profiles are shown in Figure 3.15b (the color corresponds with the color of the circles in the Figure 3.15a). The depressions are associated with Ni atoms and clusters, where the variation of the profiles is ascribed to the number of Ni atoms as well as the cluster geometry. Figure 3.15c presents a variety of Ni induced features on the bare surface with the associated line profiles plotted in Figure 3.15d. The depressions (profiles 2 and 3) are attributed to embedded Ni atoms. Further, a volcano-like cluster with an apparent height of 1.2 - 1.3 Å at the rim and 0.7 Å in the center (profile 4) and a half-volcano cluster (profile 5) are due to Ag adatoms surrounding embedded Ni atoms.[130,131]

Since Ni atoms readily exchange their position with substrate atoms, diffusing Ag adatoms become available during this process. In Figure 3.15a rectangular shaped Ag islands are randomly placed on the bare substrate and have an apparent height of about 2.05 Å, which matches exactly the height of a monoatomic step of the Ag(100) surface. In addition, the orientation of the edges of the islands follows the close-packed orientation of the Ag(100) surface.[132] The embedded Ni atoms and the network periphery act as nucleation sites for the Ag island growth. The height of the clusters decorating the network amounts to 1.4 - 1.8 Å, which is comparable to the height of the Ag adatoms in the volcanoshaped features in Figure 3.15c. Hence, we identify the clusters inside the network as Ag adatoms in the vicinity of embedded Ni atoms. The bigger clusters and filled cavities can be related to Ag atoms on the Ag(100) substrate as their apparent height is close to the height of the Ag islands. Annealing at 385 K increases the mean size of the islands on the bare surface due to the diffusion and aggregation of Ag atoms that were trapped inside the network areas.

3.2.4 Binding guest molecules into Ni-functionalized cavities on Ag(100)

The applicability of the Ni-functionalized Fe-BDBA/Ag(100) networks for the hierarchical assembly of multicomponent architectures is demonstrated by binding additional BDBA molecules into the cavities. Upon subsequent deposition of BDBA onto the Ni-decorated networks at room temperature (see Figure 3.16a), the molecules are bound into the cavities as depicted in Figure 3.16b. The guest BDBA molecule binds predominantly to the central butadiyne groups at the opposite sides of the cavity (see red circles in Figure 3.16b and scheme in Figure 3.16c). The accommodated BDBA molecules can also point to a network node or to the center of adjacent ligands of the cavity involving the bending of the guest molecule (marked by orange and yellow circles in Figure 3.16b, respectively). For steric reasons the ligands preferentially arrange parallel to the long side of the cavity. The accommodation of additional molecules was not observed for the plain Fe-BDBA network.

Discussion

A number of distinct explanations for the nature and positions of the observed adspecies can be presented since a delicate interplay of a variety of mutual interactions and surface-related processes contributes to the resulting structure. On the bare substrate the surface diffusion and island nucleation may be altered by the interchange of incoming Ni metal atoms with atoms from first substrate layer (see before). Besides reactive sites related to the substrate, e.g., step edges and heteroatoms embedded in substrate, the molecular networks, i.e., butadiyne group, phenyl rings, and coordination nodes, additionally modify the adatom diffusion.

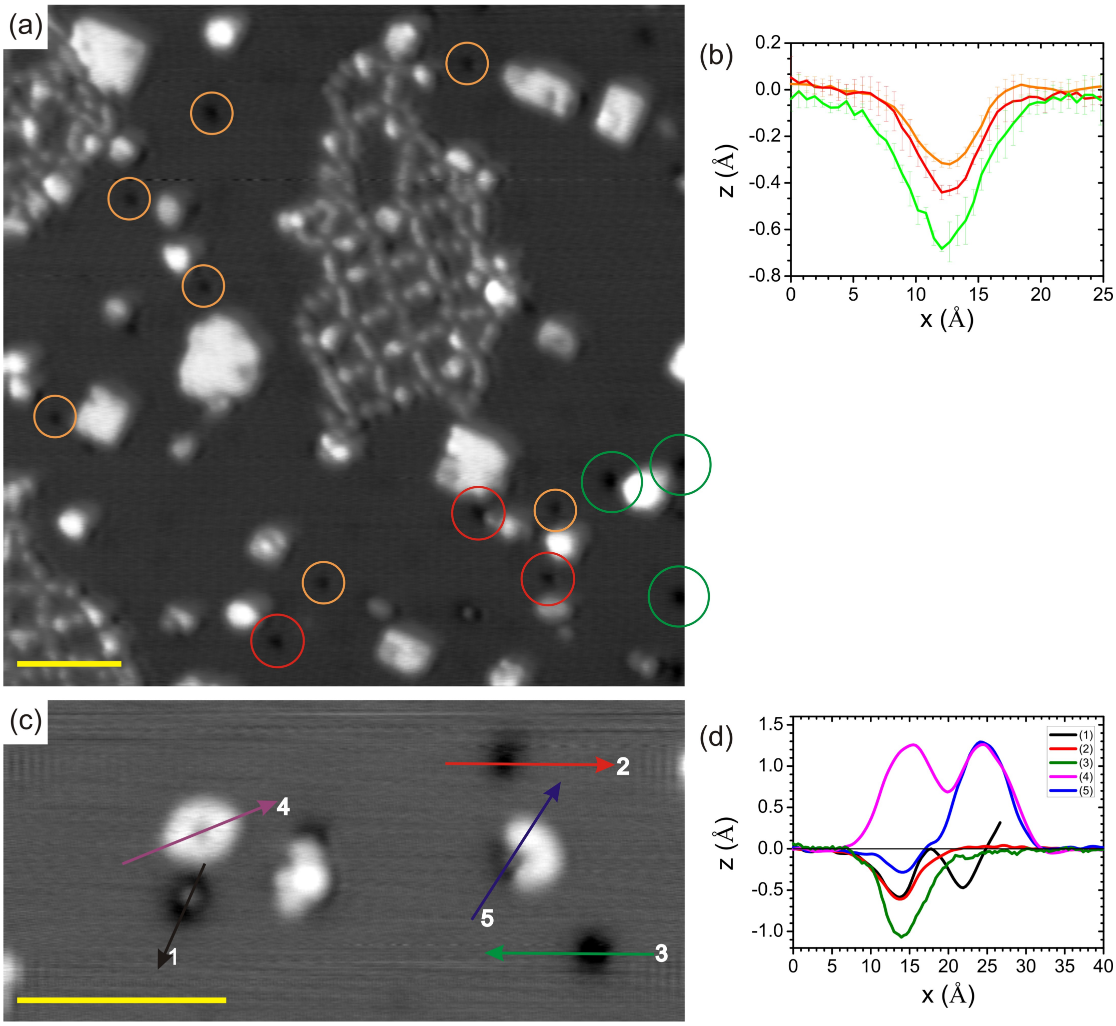

Figure 3.15: Representative STM images (a,c) acquired after Ni deposition on the Ag(100) surface at room temperature and related profiles (d) along the marked lines in (c). (a) Several smaller (orange and red) and larger depressions (green) are highlighted by circles with (b) corresponding line profiles. Acquisition parameters: + 0.5 V, 1 nA, 5 K; Scale Bar: 5nm.

Moreover, the observed features are not necessarily the thermodynamically most stable ones because all above-mentioned processes are thermally activated. All these processes should be taken into account in order to reach a coherent and consistent interpretation of the experimental results. We start the discussion by considering the surface diffusion processes of Ni adatoms on the surfaces.

The distinct observations in the incorporation of Ni into the networks on the Au(111) and Ag(100) substrates can be understood by taking into account also the elementary processes for Ni atoms on the bare surfaces. On the Ag surface, Ni atoms exchange with the substrate atoms, assuming their thermodynamically most stable position within the first layer.[131,133] The associated activation energy amounts to only ∼ 0.3 eV,[134] enabling the exchange process even at low temperatures (∼ 130 K).[133] The surface diffusion of Ni atoms proceeds via an exchange diffusion mechanism within the topmost Ag layer[135] that can be assisted by Ag adatoms (from the exchange process) binding to the embedded Ni atom (Ni - Ag pair).[131] Ni atoms migrate in the first substrate layer and form islands,[130] following the standard nucleation and island growth model.[136]

The situation changes by the presence of the Fe-BDBA network on top of the surface. Here, the mobility of the Ni-Ag pair is spatially limited to the network cavity. The apparent depth of ∼ 0.4 Å associated with a single Ni atom (see exemplary profile in Figure 3.14f and Supporting Information for details) matches

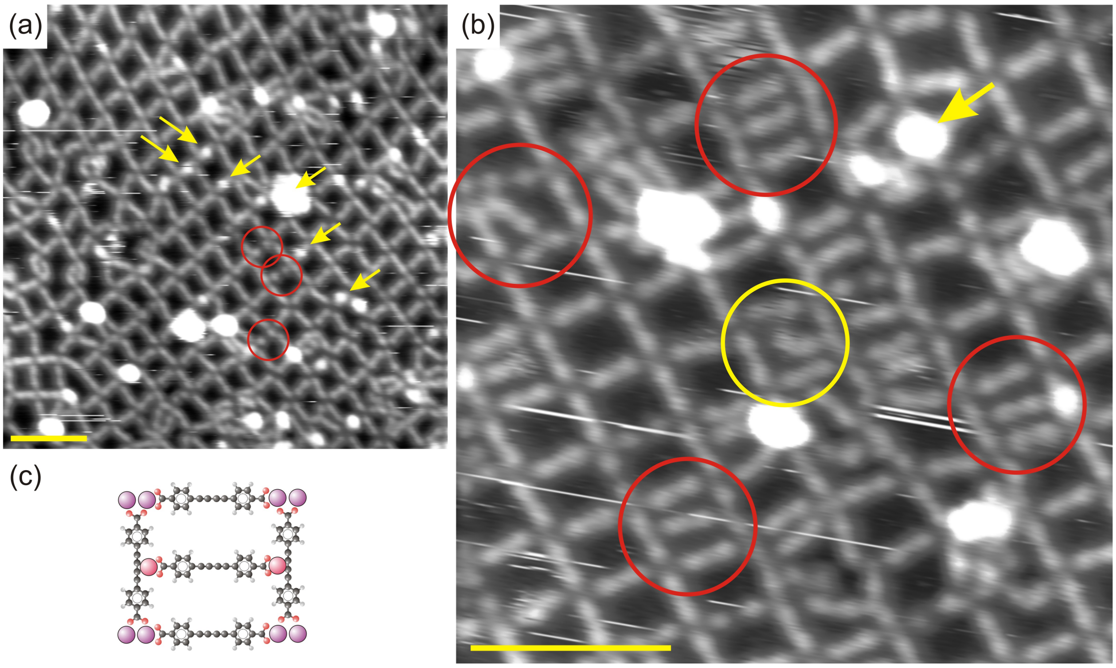

Figure 3.16: (a) STM image taken at room temperature shows the Ni-decorated Fe-BDBA/Ag(100) network before the deposition of additional BDBA molecules; the main features - ω-BDBA molecules and Ag clusters - are highlighted by red circles and yellow arrows, respectively. (b) Upon BDBA deposition (310 K), the additional BDBA molecules are bound into the cavities as highlighted by circles. The orange and yellow circles highlight accommodated BDBA molecules that point to a network node or to the center of a cavity molecule involving the bending of the guest molecule, respectively. Note that the Ag clusters are still present as marked by an arrow. (c) Tentative model of the BDBA bound into the cavity. Acquisition parameters: (a) -1.0 V, 0.07 nA, 300 K and (b) -0.9 V, 0.09 nA, 300 K. Scale bars: 5 nm.

closely the lowering of the central part of the ω-BDBA molecules. Since no excessive segregation of Ni-related islands was observed on the bare surface, and no features were found within the exposed surface area of the cavities, we propose that the Ni atoms reside directly below the butadiyne group. During the diffusion process the Ni atoms are attracted by the high electron density of the alkynyl group, thereby breaking the Ni-Ag pair. Already a weak Ni-butadiyne attraction raises the diffusion barrier for the Ni atoms, which increases the residence time of the Ni atoms in the vicinity of the butadiyne moiety and consequently enhances the probability to form a stable nucleus by trapping a second Ni atom. Figure 3.14g illustrates the proposed geometry of the Ni nucleus. Its stability is enhanced by the absence of Ag adatoms assisting the Ni diffusion. The differences and variations in the measured heights of the ligands are thus ascribed to the number and geometry of Ni atoms below the molecules. In the proposed configuration, the Ni atoms could not be incorporated oxidatively by rehybridization of the alkynyl bonds since this would lead to a strong upward bending of the ligand.[137–141] Therefore, we expect a rather weak nonoxidative binding between Ni and BDBA.[142,143]

To accommodate the additional BDBA into the cavity as shown in Figure 3.16b, we presume that the Ni atom is lifted again above the surface. The energy gain from the formation of coordination bonds ($\sim$ 1.2 eV)[34] is much higher than the energy expense ($\sim$ 0.4 eV) needed for lifting the embedded Ni atom. Apart from the butadiyne moiety, the benzene rings also possess π-electron density, and the Ni atoms can be localized there. The benzene rings show a decrease in the apparent height of 0.13 ± 0.08 Å for the ω-BDBA ligands, which suggests the presence of Ni atoms below the aromatic rings. However, a reduced height of the benzene rings was always accompanied by a significantly lowered central part of the molecules. Thus, we infer that the presence of Ni atoms under the aromatic rings is a result of the continuing growth of the Ni clusters and that the benzene rings do not serve as primary nucleation sites.

The stability of the Ni functionalized network at temperatures exceeding 450 K is significantly higher compared to previous reports, in which Co and Fe decorated networks start to collapse above 250 K.[125] Since every molecule in the network acts as a nucleation site for Ni atoms, the resulting pattern shows a mean Ni cluster distance of 2 nm corresponding to an areal density of 4×10^{13} clusters/cm^2. Besides the organic templates,[125,126] other patterning methods can be employed to steer the cluster growth with comparable areal cluster density. These include the use of surface strain relief patterns,[144] surface oxide templates,[145,146] or graphene Moiré patterns.[147] However, only the last two approaches also show appreciable cluster stability above room temperature.[146,147]

The trapped Ni atoms and clusters can serve as a template for the growth of metal clusters of a third kind as demonstrated by the presence of Ag clusters. These Ag adatoms originate from the Ni-Ag exchange process and aggregate close to embedded Ni atoms inside the networks or on the bare surface. The room temperature stability of the Ag clusters is traced back to their appreciable binding energy of 0.59 eV in the vicinity of an embedded Ni atom. This energy gain increases to 0.82 eV for Ag adatoms in contact with two Ni atoms, which usually leads to the capping or encapsulating of Ni islands on the bare Ag surface.[130,131] At elevated temperatures, the Ag atoms can overcome the binding energy, resulting in the removal of the Ag clusters from the network area and to the attachment of the adatoms to the substrate step edges and Ag islands on the bare surface (Figure 3.14e). In contrast to Ag(100), on the Au(111) surface the Ni adatom interchange takes place only in the vicinity of elbow sites of the herringbone reconstruction,[129] leading to the preferential formation of Ni islands at these sites.[148,149] This preference is maintained even within the network area. However, the size of the clusters is limited to the size of the cavity. The composition of these islands is presumably a mixture of Ni and Au atoms.[150] On Au(111) the Ni atoms show only a low affinity to the butadiyne moiety but rather interact more strongly with the benzene rings. The interaction of transition metal atoms with the benzene rings of organic templates was reported recently. Cobalt atoms residing on top of the benzene rings were observed for both coordination networks[125] and molecular adlayers[126] on a Ag(111) substrate. The observations were explained by the formation of stable half-sandwich complexes.[151] Similar behavior was observed for Fe atoms decorating the benzene rings at lower temperatures (90-130 K).[125] In this work a slightly asymmetric binding of the Ni atoms to the benzene rings was found on Au(111) (cf. Figures 3.12b and 3.12c). The calculated binding energy to a free benzene ring is considerably lower for Ni (1.73 eV) compared to Co (2.58 eV).[152] On the other hand, the adsorption energy of a Ni adatom on Au(111) amounts to about 2.9 eV.[34] Hence, a preferential binding of Ni atoms to the substrate would be expected. This explains the observation of filled cavities after annealing the substrate, which was not observed for both Fe and Co atoms on the Ag(111) surfaces.[125] The Ni binding to the benzene rings is only metastable for the BDBA ligands on Au(111). Further insight into the selective interaction of Ni atoms with the BDBA ligand on the two surfaces can be gained by the investigation of the Ni-BDBA interaction in the absence of Fe.

3.2.5 Ni-BDBA networks

On Au(111), Ni binds almost exclusively to the carboxylate oxygen atoms, forming nearly identical network structures as Fe-BDBA. Contrarily, on Ag(100) predominantly disordered structures were found that involve the binding of Ni adatoms equally to the carboxylate and the butadiyne groups. The bonding to the latter is sufficiently strong to bend the ligands, indicating a strong oxidative Ni-butadiyne association.[137,141] The Ni atoms could also interact with the carboxylate groups. Since Fe forms stronger coordination bonds with carboxylate groups than Ni,[34] the interchange of Ni and Fe atoms in coordination nodes is not expected. However, the clustering of Ni atoms with Fe dimers at the network node after a pronounced annealing at temperatures beyond 450 K cannot be fully excluded. To examine the difference in the interaction of Ni atoms with the BDBA butadiyne moiety on both Au(111) and Ag(111) surfaces, we investigated the interaction of Ni and the free BDBA ligand. The intact BDBA molecules form close packed domains consisting of complementary hydrogen bond rows on both Au(111) and Ag(100) substrates; for details see Section 3.1. Subsequently deposited Ni binds to BDBA and forms metal-organic networks at elevated substrate temperature of 430 - 450 K. As presented in Figure 3.17a, the Ni-BDBA coordination networks on the

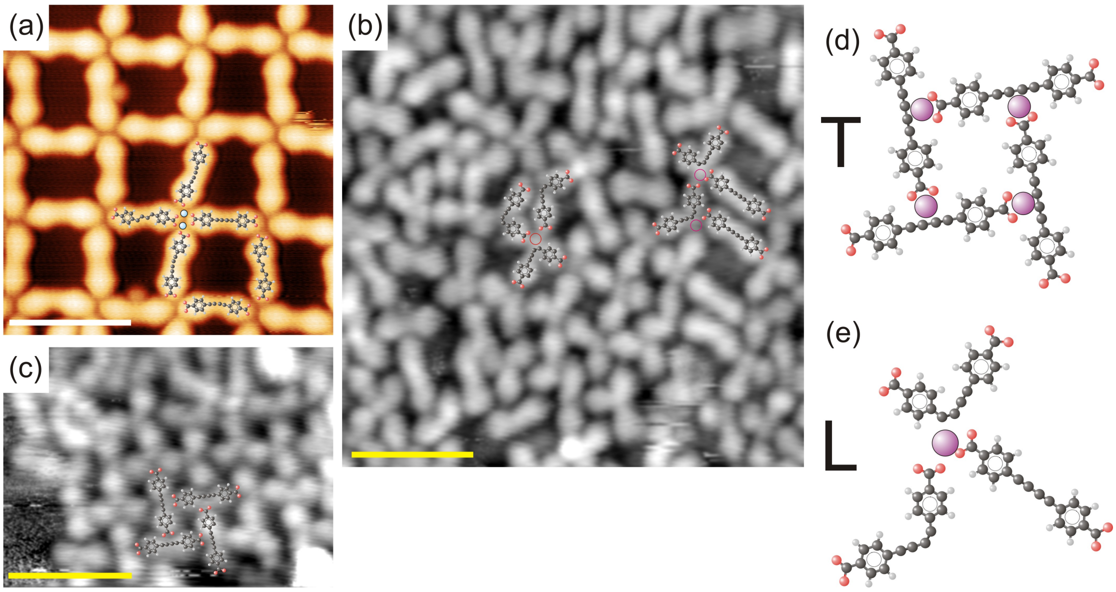

Figure 3.17: Representative STM images of (a) the Ni-BDBA coordination network formed on Au(111) substrate, and (b, c) L- and T- shaped binding motifs within disordered Ni-BDBA phases on Ag(100). The tentative models of T- and L- shaped geometry are depicted in (d) and (e), respectively. Acquisition parameters: -1.0 V, 0.3 nA, 5 K (a); -1.2 V, 0.2 nA, 297 K (b); -1.0 V, 0.4 nA, 297 K (c); Scale bars: 3 nm.

Au(111) resemble their Fe-BDBA analogue. In contrast, on Ag(100), Ni atoms interact strongly with the butadiyne moiety and disordered phases possessing no long range order were mainly observed. Figures 3.17b and 3.17c present two typical small ordered domains coexisting with the disordered phase. Here, two prevailing binding motifs are distinguished: (1) T-shaped motif with Ni atom in between the butadiyne group and carboxylate moiety of two distinct ligands (Figure 3.17d). In this case, a pronounced lowering of the central part of BDBA molecules hosting the Ni atoms is observed, which relates the origin of ω-BDBA molecules to the presence of Ni atoms. (2) L-shaped motif where the Ni atom coordinates to two BDBA carboxylate groups and one alkynyl carbon atom of the butadiyne moiety. Such a binding situation supports the mechanism of oxidative addition of the metal atom to the ligand.[137–141] This binding motif includes the lowering of the carbon-carbon bond order from $sp^1 \rightarrow sp^n$ (with n close to 2) of the alkynyl carbon to a trigonal planar geometry and the formation of σ-bonds between both C atoms of the alkyne and the nickel atom (see tentative model in Figure 3.17e). This results in the strong bent shape (L-shape) of the BDBA molecule. From the energy expense for the lifting of Ni atoms from the embedded to the adatom position ($\Delta E = 0.3$ - 0.4 eV[131,134]) and the stability of this configuration at room temperature, one can estimate the lower limit for the associated binding energy to 0.5 eV.

However, for an existing Fe-BDBA network this strong binding is only possible at the network periphery, i.e., for undercoordinated ligands. Here, strong deformations of the BDBA molecules were observed even on the Au(111) surface. Within the network, the BDBA geometry is fixed by the dominant coordination bonds to Fe atoms, and hence, the structural change associated with the rehybridization of alkynyl bonds is not possible. Consequently, the Ni atoms can only interact nonoxidatively with the high π-electron density of the butadiyne group, which results in a much weaker binding of Ni atoms to the ligand molecules.

The striking difference in the behavior of the Ni binding on Au(111) and Ag(100), both to the free ligands and within the Fe-BDBA networks, highlights the role of the underlying substrate. On the one hand, the Ni adatom processes are distinct on the two surfaces as described above, and on the other hand, the specific interaction of the π-electrons of the butadiyne moiety and benzene rings with the metal substrates results in different chemical states of the constituents on the two surfaces and hence to different affinities to Ni atoms.

In summary, the incorporation of Ni atoms and clusters into open two-dimensional robust metal-organic templates was demonstrated. The functionalized networks are thermally stable at temperatures up to 450 K and enable the coordination of additional molecules into the open structures, demonstrating the utilization of selective interactions for the assembly of multicomponent architectures at different organizational stages. Further, we showed that the employed metal substrate plays a crucial role in the interaction of transition metal atoms with the metal-organic host networks. On the Ag(100) substrate, the surface-confined metal-organic template steers the growth of the Ni clusters underneath the network pattern. Here, the embedded Ni atoms nucleate preferentially at the butadiyne moiety of the BDBA ligands. Thereby, Ni clusters consisting of a few metal atoms with an areal density of 4×10^{13} cm^{-2} can be obtained. In contrast, on the Au(111) substrate the Ni atoms interact preferentially with the BDBA benzene rings and form size-limited clusters inside the cavities.

The work demonstrates the unique occurrence of selective interactions in a multicomponent system including the surface that may be further explored to create functional molecular architectures with novel properties. Moreover, the stability and direct accessibility of the non-capped Ni atoms and clusters on both gold and silver substrates render these systems attractive candidates to explore their catalytic activity.

4 Resolving the molecule-oxide interface of DSSCs

In a time when conventional sources of energy become depleted, the development of potent novel technologies for the efficient conversion of solar energy into electricity and suitable energy carriers plays a key role in paving the way towards a carbon neutral energy economy. Furthermore, it is of paramount importance to improve the efficiency of existing technologies in order to meet the challenges of the climate change and the increasing energy demands of the future. As explicitly illustrated in the main introduction chapter, dye-sensitized solar cells constitute a promising approach meeting the requirements of sustainability and low production costs with considerable light conversion efficiencies in excess of 12 percent.[61,66,153,154] However, at present, substantial improvement of the DSSC efficiencies is particularly hindered by a deficient understanding of the interfacial characteristics of the dye-substrate interface at a fundamental level. Since the charge injection efficiency and consequently the overall photovoltaic performance of DSSCs directly depends on the effective coupling of the photosensitizer molecules to the TiO_2 substrate (see below), great theoretical and experimental efforts have been made to investigate such dye-substrate interfaces. So far, the detailed structural and electronic properties of photosensitizer molecules adsorbed on TiO_2 surfaces are being actively debated and no conclusive understanding has been achieved at the atomic level.

For the first time since the invention of the DSSC in 1991,[61] we address the challenge of investigating at the atomic level the geometrical and electronic characteristics of both the photosensitizer N3 and its anchoring ligand BINA on the most relevant surface of DSSCs - TiO_2 anatase (101). The unique method of electrospray ion beam deposition was employed to bring the thermally fragile N3 dye onto the oxide surface at maximum level of control. The molecule-substrate interface was investigated by means of scanning tunneling microscopy and spectroscopy methods at 5 K in UHV. Furthermore, the N3 dye was investigated on Au(111) surfaces.

Extensive first-principle density functional theory based calculations were performed to support the experimental findings.

This chapter is organized as follows: at first, the basic concepts of DSSCs are described. The next paragraphs introduce the material properties of TiO_2 and illustrate different ways how molecules with carboxylate anchoring groups can coordinate to metal oxide surfaces. Subsequently, the successful preparation of natural TiO_2 anatase (101) crystals and its characterization by means of STM and STS are described. In the following, the combined experimental and theoretical study of the structural and electronic properties of the photosensitizer N3 adsorbed on TiO_2 anatase (101) is presented. The structural and electronic properties of the N3 dye deposited on Au(111) are compared to the results obtained on the TiO_2 substrates. At the end, the findings are correlated to atomic-scale investigations of the N3 anchoring ligand BINA on TiO_2 anatase (101).

4.1 Scientific background

4.1.1 Dye-sensitized solar cells

In conventional solar cells, charge separation is achieved by an internal electrical field, produced by incorporating differently charged atoms in a semiconducting material. In this way, an electron-rich *n*-region and a hole-rich *p*-region can be produced, which together form a pn-junction with a certain build-in potential difference. Depending on the specific realization of this junction, light absorption and electron-hole pair generation happens either mostly in the *p* or in the *n* region of the semiconductor. This implies that either electrons or holes are minority charge carriers, with only very short lifetimes due to interfacial recombination. Since recombination occurs very likely at impurities, the chosen material has to be extremely pure to guarantee high energy conversion efficiencies. In addition, the material has to be a very good conductor for both electrons and holes, and has to harvest incident photons from sun efficiently, i.e. its bandgap has to be close to the optimum values of 1.4 eV.

In DSSCs, where the two operation steps of light absorption and charge separation are separated, the materials can be optimized independently. The operating principle of DSSCs is schematically depicted in Figure 4.1a. These devices consist of a mesoporous high-surface-area TiO_2 layer on a transparent fluorine-doped SnO_2 conducting glass coated with a charge-transfer dye to sensitize the film for light harvesting.[61] Similar to natural photosynthetic systems with chlorophyll molecules,

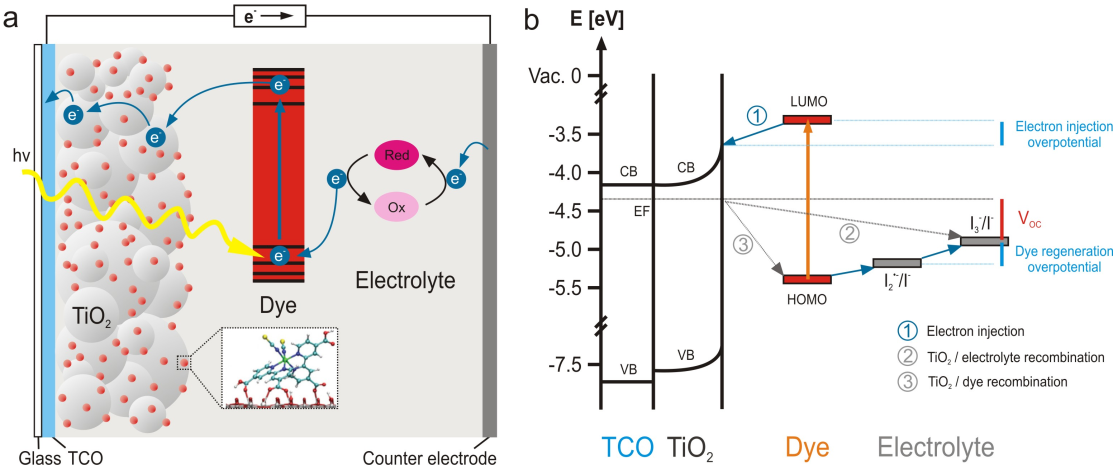

Figure 4.1: (a) Schematic view and device operation of a dye-sensitized solar cell (DSSC) comprised of a transparent conducting oxide on glass, a nanoparticle photoanode covered by a monolayer of sensitizing dye, a hole-conducting electrolyte and a FTO-coated glass back-contact. The sensitizing dye absorbs a photon, the electron is injected into the conduction band of the metal oxide and travels to the front electrode. The oxidized dye is reduced by the electrolyte, which is regenerated at the counter-electrode to complete the circuit. (b) Energy level diagram of a DSSC. The open-circuit voltage V_{OC} is determined by the Fermi level of titania and the redox potential (I_3^-/I^-) of the electrolyte.

the light absorption is handled by a photosensitizer. As indicated in Figure 4.1a and 4.1b, photoexcitation of the dye molecule is followed by ultrafast electron injection from the dye into the conduction band of the TiO_2 film.[155,156] Subsequently, the photosensitizer is regenerated by electron donation from the redox electrolyte such as an iodide/triiodide couple.[157] The regeneration of the redox mediator by reduction of the triiodide at the counterelectrode completes the electric circuit which results in the generation of a photocurrent through an external load.[62,158] Since only majority charge carriers are involved in this process, the demands on material purity existing in conventional pn-devices can be relieved. To a great extent, the efficiency of DSSCs depends on the structure-property relationship at the photosensitizer-TiO_2 interface. For example, efficient excited-state charge transfer dynamics necessitate stable electronic coupling between the sensitizer molecules and substrate atoms. Hence, particularly the dye adsorption geometry on TiO_2 nanoparticles has crucial influence on the electron transfer kinetics and open-circuit potential of DSSCs.[159] Furthermore, the dye has to be custom-tailored to have optimized lowest unoccupied molecular orbitals (LUMOs) and highest occupied molecular orbitals (HOMOs) relative to the energy levels of both the substrate and electrolyte. As shown in Figure 4.1b, the open-circuit voltage V_{OC} of DSSCs is determined by the Fermi level of the titania and the redox potential of the electrolyte.[62,66] In turn, the process of electron injection is controlled by the energy difference between the conduction band of the TiO_2 material and the LUMO level of the dye. In this context, the process of electron recombination is mainly dominated by the interaction between the electrons at the surface of TiO_2 and the I_3 - ions in the electrolyte. Charge recombination at the surfaces or back-electron transfer to the electrolyte are a direct result of interfacial processes and can both act to reduce the efficiency of DSSCs. In particular, the process of electron injection at the TiO_2/dye interface and the electron recombination reaction at the TiO_2/dye/electrolyte interface are critical because they control both the short-circuit current and open-circuit voltage of the DSSC. Thus, the characterization of the dye-substrate interface at the atomic level is of great importance to optimize the overall photovoltaic performance of DSSCs.

4.1.2 TiO_2 anatase substrate

The low-cost, widely available and non-toxic wide-bandgap semiconductor titanium dioxide represents one of the most investigated metal oxides. As mentioned in the main introductory chapter, TiO_2 materials find versatile applications in important technological areas. Titanium oxide exhibits three major crystalline polymorphs: the tetragonal forms rutile and anatase as well as the rhombic form brookite.[43,160–166] Titanium(IV) is the most stable valence state while Ti(II) and Ti(III) are readily oxidized to the tetravalent state.[167] Accordingly, the titanium-oxide system shows a quite diverse phase diagram with a lot of different structures and stoichiometries TiO_x with $x=\frac{2}{3}, 1, \frac{3}{2}, \frac{5}{3}, 2, \frac{7}{4}, \frac{2n-1}{n}$ (n=4,...,10).[167] With increasing n, the phase structures resemble more and more closely that of TiO_2 rutile. While rutile constitutes the thermodynamically stable phase, both anatase and brookite are metastable. The TiO_2 brookite is difficult to synthesize in the laboratory and is consequently rarely studied.[168] In contrast, surface science investigations have yielded a quite extensive database on the structural and chemical properties of single-crystalline rutile TiO_2.[43,169] On large single TiO_2 anatase crystals, only few atomic-scale studies exist so far.[170–176] However, the anatase phase represents the technologically most interesting crystallographic form of titanium dioxide since, in many cases, it exhibits a higher photocatalytic acitivity in its bulk form than other TiO_2 polymorphs.[59,62,63] Furthermore, mesoporous TiO_2 films in DSSCs are predominantly of the anatase phase.[43,63,170,175,177,178]

TiO_2 anatase has the same stoichiometry as rutile, but a different crystal structure with space group $I4_1$ (compared to rutile $P4_2$). Figure 4.2d shows the 140 $Å^3$ sized tetragonal unit cell of the metastable TiO_2 anatase phase including four TiO_2 units which corresponds to nearly 100 atoms/nm^3. The bonding of titanium with

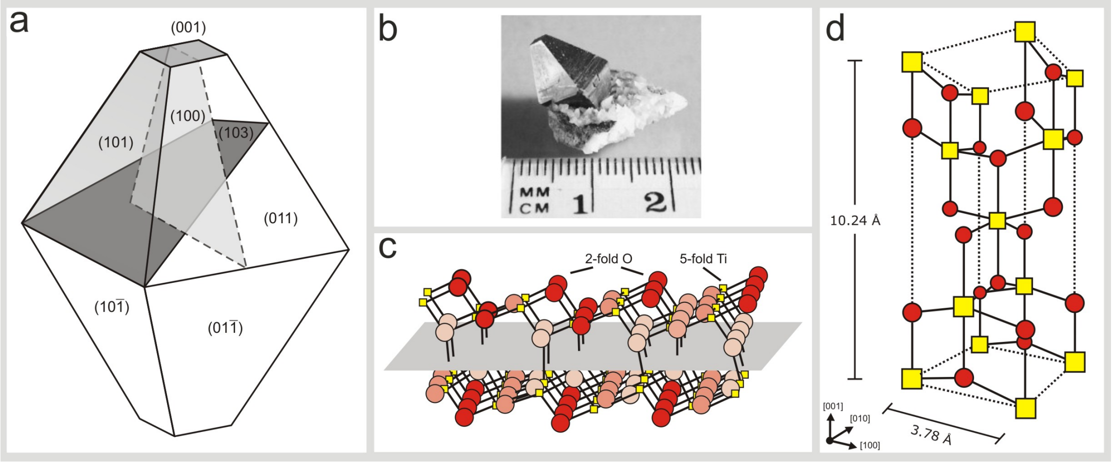

Figure 4.2: (a) The equilibrium shape of a TiO_2 crystal in the anatase phase, according to the Wulff construction and surface energies given in Ref. 170. The crystallographic planes that have been investigated with surface science techniques are indicated. (b) Photograph of a natural TiO_2 anatase mineral crystal characterized by an octahedron shape (image taken from Ref. 170). (c) Side-view atomic model of the low-energy bulk-terminated TiO_2 anatase (101) surface with characteristic sawtooth-like surface corrugation. The titanium (Ti) ions are five-/sixfold coordinated and the oxygen (O) ions are two-/threefold coordinated, respectively. (d) Schematic drawing of the bulk TiO_2 crystal structure in the anatase phase. The space group is $I4_1/amd$, the unit cell 10.24×3.78 Å^2 in size with the substrate orientation indicated. (yellow: titanium atom, red: oxgen atom)

oxygen atoms has rather ionic character.[179] The titanium cation is surrounded by a distorted oxygen octahedron with each octahedron having four edge-sharing and four corner-sharing neighbors. Each titanium atom is coordinated via two (long) apical and four (short) equatorial bonds, of lengths 1.979 Å and 1.932 Å, respectively.[180] Figure 4.2a shows the equilibrium shape of an anatase crystal calculated according to the Wulff construction[181] with the relevant surface planes. This calculated anatase equilibrium shape compares well with the bipyrimidal shape of naturally-grown mineral samples as exemplary shown in Figure 4.2b (image taken from Ref. 170). Several theoretical studies have predicted the stability of the different low-index anatase surfaces.[178,182] It appears that the (101) orientation which is stable in a (1×1) configuration was found to be the thermodynamically most stable surface of anatase.[170,177,178,183] Interestingly, the average surface energy of an equilibrium-shape anatase crystal is smaller than the one of rutile,[178] which explains the fact that nanoscopic TiO_2 particles are more stable in the anatase phase. A side-view model of the main low-energy bulk-terminated (101) surface with characteristic sawtooth-like surface corrugation is shown in Figure 4.2c. As indicated, the titanium atoms at the terraces are fivefold and sixfold coordinated, and titanium atoms at the step edges are fourfold coordinated. Twofold coordinated (bridging) oxygen atoms are located at the ridges of the sawtooth like structure. According to previous studies,[182] these oxygen atoms relax inwards by ~ 0.21 Å. The threefold coordinated O atoms relax outwards by 0.06 Å and the fivefold coordinated Ti atoms inwards by 0.17 Å, so that the surface exhibits a slightly buckled geometry. The coordinatively unsaturated 2(5)-fold O(Ti) atoms (indicated in Figure 4.2c) are expected to be favorable anchoring points for adsorbates. At elevated temperatures, the metastable anatase phase transforms irreversibly to rutile[184] where the transition temperature depends on a variety of factors including impurities and crystal size. One strategy to deal with this problem was to grow TiO_2 films on $SrTiO_3$ (001)[185,186] and $LaAlO_3$[187] but only the (001) crystallographic surface of anatase could be studied in this manner. Synthetically grown anatase[63,171,188,189] are typically small and take a considerable time to grow. Alternatively, mineral samples[170,186,190] as large, well ordered, single-crystalline, and relatively pure specimens can be found in nature. However, working with natural minerals poses its own difficulties, in particular its preparation in UHV as described below.

The general topology of the electronic band structure was found to be similar for both TiO_2 anatase and rutile. As expected for a mostly ionic compound, the electronic bands are very flat. However, the most striking difference in the bandstructures of anatase and rutile is the deeper minimum in the conduction band of anatase which indicates a much smaller effective electron mass in anatase being 10 times lower compared to rutile.[48,191] In contrast, the effective hole mass seems to be higher in anatase compared to rutile resulting in substantial differences in the electron transport properties of the two polymorphs. The electron transport is clearly favored in anatase due to the much higher electron mobility in the conduction band. The single-band conduction in anatase is isotropic in contrast to rutile in which anisotropic conduction occurs due to the presence of several conduction band minima.[48,191] Because of the high bandgap of anatase, thermally excited intrinsic charge carriers are generated only in very small numbers at ambient temperatures. Consequently, electrical currents are usually sustained by extrinsic charge carriers. For example, oxygen vacancies produce bandgap states which are associated with Ti^{3+} ions acting as electron donor. In heavily doped anatase films, even a Mott transition to metallic conduction occurs.[192] The higher photoactivity of TiO_2 anatase compared to rutile can be partially attributed to the Fermi level of the anatase which is about 0.1 eV higher than that of rutile.[43,193] However, no clear and widely accepted explanation is available yet.

4.1.3 Carboxylate groups on metal oxides

A carboxylate group can coordinate to metal oxide surfaces in different ways, e.g. in a monodentate, a chelating or a bridging bidentate mode as illustrated in Figure 4.3.[194] The monodentate coordination of a carboxylate group removes the equivalence of the two oxygen atoms resulting to an ester type of bond formation between the carboxylic acid group and for instance the TiO_2 surface. Attenuated total reflectance Fourier transform infrared spectroscopy (ATR-FTIR) allows the elucidation of specific coordination configurations of carboxylate groups for instance on TiO_2.[194] In ATR-FTIR spectroscopy measurements, the asymmetric and symmetric bands in the free and the adsorbed state of the carboxylate group have been used as criteria for identifying the carboxylate-anchoring mode.[194] If the difference between the asymmetric and symmetric bands of the carboxylate group in the adsorbed state is lower than that in the free state, the anchoring mode is interpreted being either bidentate chelating or bridging. If the band difference is greater or equal to that in the free state, the anchoring mode is most probably unidentate. For the photosensitzer N3, ATR-FTIR spectroscopy measurements suggested e.g. a bridging coordination mode on nanocrystalline TiO_2.[195] To note, there are several hints from both experiment[196] and theory[197] that the bridging binding is favoured over monodentate ester type binding for an individual carboxyl group on metal oxide surface such as TiO_2. However, the elucidation of specific coordination types, particularly at dye-TiO_2 interfaces, remains demanding.

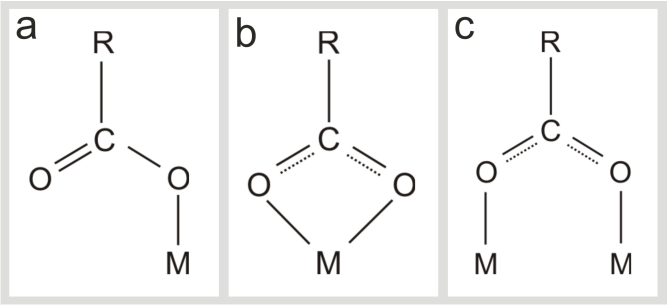

Figure 4.3: Carboxylate coordination to metal oxide surfaces: (a) monodentate (b) chelating (c) bridging bidentate mode.

4.2 Preparation of atomically well-defined TiO_2 anatase (101)

4.2.1 Natural TiO_2 anatase single bulk crystal

Experimental investigations on well-defined TiO_2 anatase (101) surfaces are still relatively sparse. The lack of atomic-scale studies on this surface most relevant for DSSCs is mainly attributed to major difficulties in successful sample preparation. On the one hand, TiO_2 anatase is a metastable phase which makes the preparation of both suitably large and atomically well-defined surfaces challenging. In this work, natural TiO_2 anatase single crystals with a size of $\sim 4\times4\times2$ mm^3 and a metallic opaque color[198] were employed as depicted in Figure 4.4a (supplier: SurfaceNet GmbH). The crystals were cut in the (101) surface orientation and polished with a roughness of smaller than one lattice constant. X-ray photoelectron spectroscopy (XPS) measurements indicate relatively small amounts of impurities (lower than 1 % of Zr, Al, Zn, Pb). Furthermore, the natural TiO_2 anatase crystals were investigated by X-ray diffraction method (XRD) to ensure surface orientation in the (101) plane. For coherent scattering from a crystal lattice, the Bragg's law has to be fulfilled: $\mathrm{n}\lambda = 2\mathrm{dsin}(\Theta)$. With respect to the tetragonal unit cell of TiO_2 anatase, *d* can be calculated according to $\mathrm{d_{hkl}} = \frac{1}{\sqrt{\frac{\mathrm{h^2+f^2}}{\mathrm{a^2}}+\frac{\mathrm{l^2}}{\mathrm{c^2}}}}$ with h=1, k=0 and l=1 for anatase (101). The lattice constants for anatase are a = 3.74 Å and b = 9.39 Å while the XRD measurement was performed at λ=1.54059 Å. The XRD spectra of the natural TiO_2 anatase crystal is shown in Figure 4.4c. It reveals two major peaks at 26.21° and 82.53° which nicely correspond to the calculated value Θ = 27,20° (n=6) and Θ = 82,19° (n=13). Since there are no further major peaks in the XRD spectra, the anaylsis shows that the TiO_2 anatase crystal is ideally cut and polished in the (101) surface plane. The crystals were further analyzed by Laue diffraction technique indicating high crystallinity (cf. Figure 4.4b). Before transfer into UHV, the natural TiO_2 crystals were cleaned both with acetone and isopropanol. Subsequently, the crystal surfaces were prepared in UHV by repeated cycles of Ar^+ ion sputtering (ion energy 600 eV, incidence angle 30°, ~ 1 μA ion beam measured on the sample, 10 min) and annealing at $\sim$ 900 K (pressure below 2×10^{-9} mbar, 10 min). On a regular basis, the TiO_2 crystals were reoxydized by dosing oxygen for 15 minutes at a partial pressure of $\sim 5\times10^{-7}$ mbar while keeping the crystal at $\sim$ 900 K. The reoxidation is required since the TiO_2 gets reduced to a n-type semiconductor by vacuum annealing. In this context, XPS studies led to the conclusion that defects are localized at the titanium sites next to oxygen vacancies.[199, 200] The surface-defect states can be quenched by exposure of

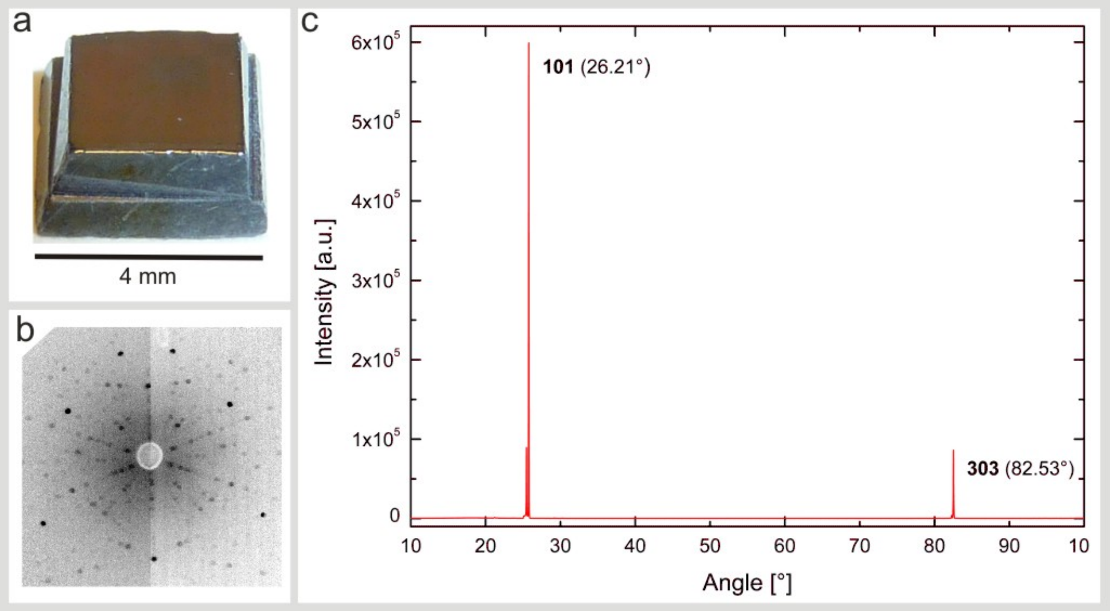

Figure 4.4: (a) Natural TiO$_2$ anatase single crystal which was cut and polished in the (101) surface orientation and employed in this work. (b) Laue diffraction pattern and (c) XRD spectrum of the natural TiO$_2$ anatase crystal.

the sample to oxygen at elevated temperature,[201,202] which fills the vacancies.[203,204]

4.2.2 STM characterization

Figure 4.5a shows a typical STM overview image of the bulk-terminated TiO$_2$ anatase (101) surface after crystal preparation. The surface morphology is characterized by flat terraces with an average width of ∼20 nm and characteristic trapezoidally shaped islands. As indicated, the monoatomic steps are preferably orientated along the [010], $[11\bar{1}]$ and $[\bar{1}11]$ crystallographic directions which were assigned according to previous work.[175] On a molecular scale, a typical nanocrystalline facet of 25×25 nm^2 is indistinguishable from the similarly sized anatase terrace of such a bulk single crystal. Figure 4.5b shows the atomically resolved anatase (101) surface where rows of circular-shaped protrusions oriented along the [010] direction are revealed.[171] The interpretation of atomically resolved constant-current STM topographies on TiO$_2$ surfaces is complicated by strong electronic effects.[171,175] Because TiO$_2$ anatase is an n-type semiconductor with 3.2 eV band gap, empty states are usually imaged when scanning at positive bias voltage. The conduction band is dominated by titanium 3d states which should give rise to a high tunneling probability and bright contrast on titanium sites. On the other hand, the anatase (101) surface is very corrugated and the twofold-coordinated oxygen

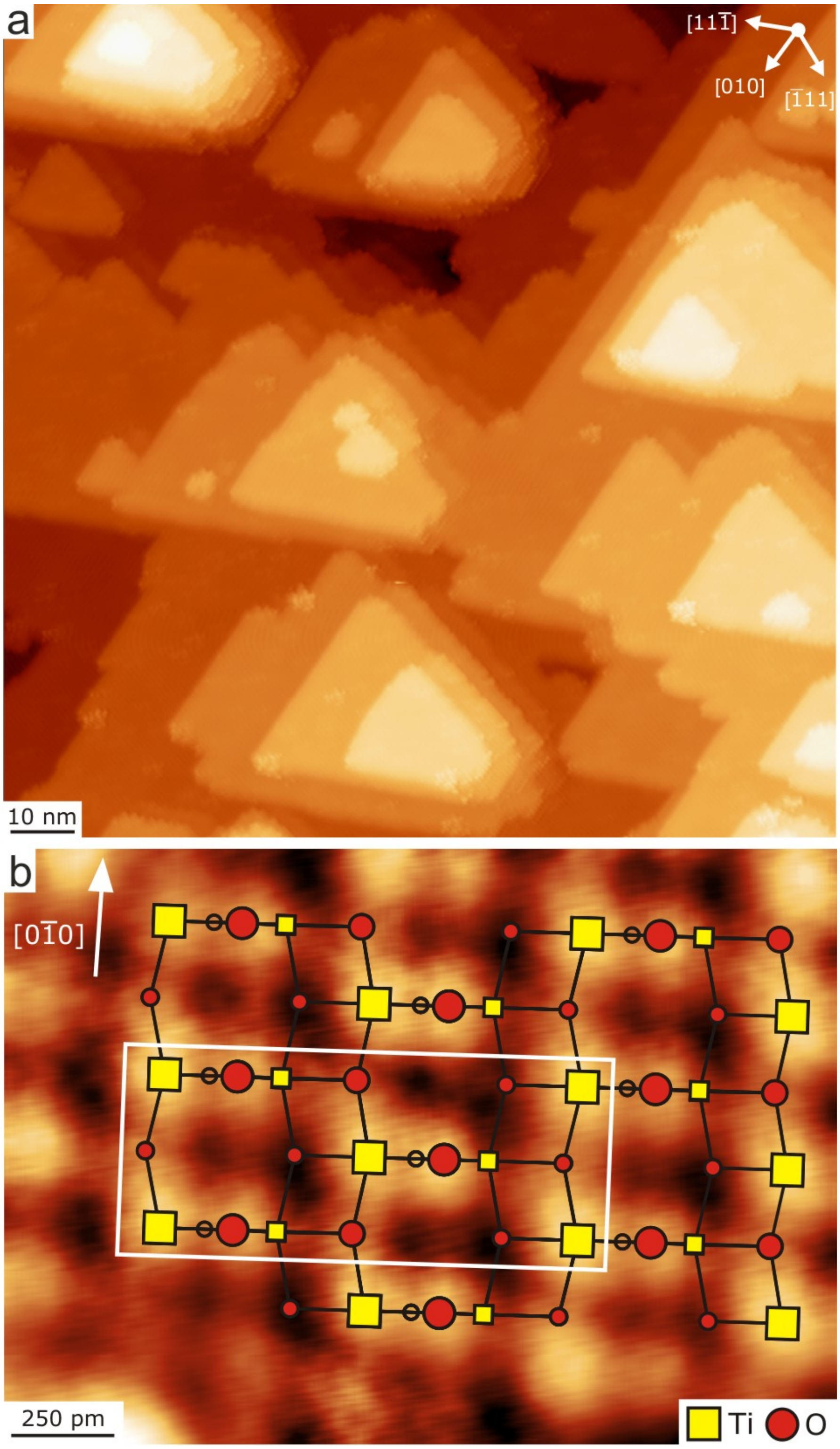

Figure 4.5: (a) STM overview image of TiO_2 anatase (101) showing typical trapezoidal islands and monoatomic steps with distinct orientations (1.8 V, 0.16 nA, 5 K). (b) Atomically resolved substrate with unit cell overlayed (1.2 V, 0.2 nA, 5 K). The titanium and oxygen atoms are indicated in yellow and red, respectively.

atoms at the highest position could also be imaged bright. The corresponding unit-cell is overlayed to the STM image with respect to the assignment made in previous work[175] (see Figure 4.5b). The bright features are identified as twofold oxygen atoms. These STM surface investigations proof both the suitability of the described sample preparation procedure and the high quality of the natural TiO_2 anatase single crystals. These findings renders the natural TiO_2 anatase crystal to a highly suitable substrate for studying photosensitizer-TiO_2 interfaces at the atomic level.

Defects on TiO_2 anatase (101)

TiO_2 samples used in experiments are generally reduced and should thus contain a substantial amount of oxygen vacancies and titanium defects. These defects have been known for long time to play a central role in the surface chemistry of oxide materials. Oxygen vacancies are also relevant for the sputtering and annealing processes that are used to prepare the surface: the diffusion of these defects, and of Ti interstitials, largely determines the mass transport occurring between the surface and the bulk,[206] as well as the surface reconstruction that often results from these processes.[207] However, TiO_2 anatase surfaces were found to have a significantly lower defect concentration and are more difficult to reduce than the rutile surface.[43,208] Titanium interstitials prefer to have a high coordination and therefore are mostly found in the bulk. For oxygen vacancies, instead, undercoordinated surface sites, where a smaller number of Ti-O bonds needs to be broken, should be

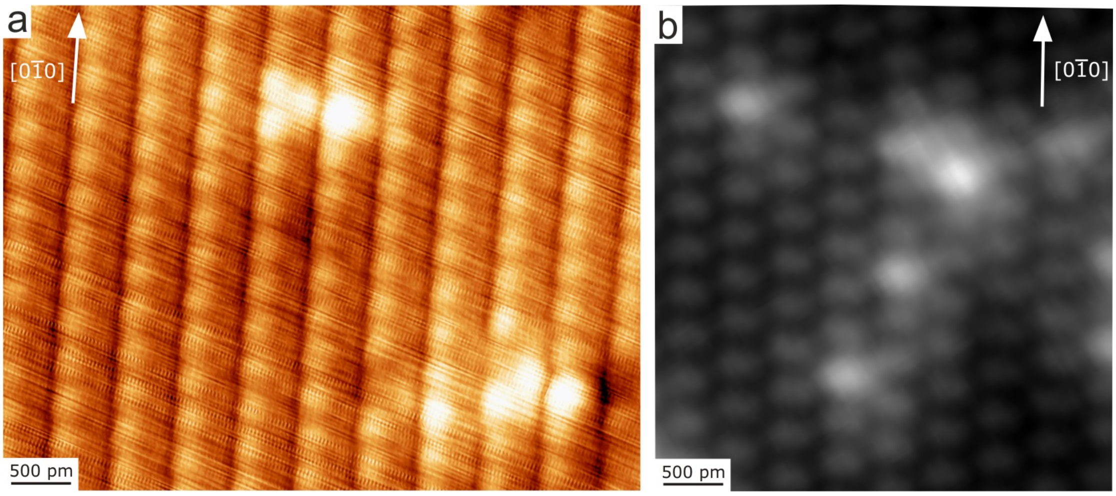

Figure 4.6: High-resolution STM images of TiO_2 anatase (101). (a) Bright spots are revealed at regular lattice sites (1.8 V, 1.0 nA, 5 K). (b) STM image taken from Ref. 205. The bright features were attributed to oxygen vacancies.

energetically favored. Thus, these defects should be observed on the TiO_2 anatase surfaces. STM measurements of the bare TiO_2 anatase (101) were performed to elucidate the amount of surface defects. Figure 4.6 shows a high-resolution STM image of the clean, almost pristine TiO_2 anatase (101) surface measured at 5 K after sputtering and annealing (sample preparation see Section 4.2.1). At regular lattice sites, some bright features were revealed. These features resemble previous STM observations in which the bright protrusions were attributed to oxygen vacancies on TiO_2 anatase (101) as shown in Figure 4.6b (taken from Ref. 205). The low defect concentration revealed on this natural TiO_2 anatase (101) surface is in agreement with theoretical predictions. A removal of a twofold coordinated oxygen atom would give rise to one fivefold and one highly unstable fourfold coordinated Ti^{3+} cation, whereas the Ti^{3+} cations neighboring bulk oxygen vacancies are fivefold coordinated. Moreover, the titanium-oxygen (twofold coordinated) bonds are short and strong, so breaking two titanium-oxygen bonds at the surface is expected to be energetically more costly than breaking three in the bulk. Therefore, defects on the anatase surface were shown to migrate into the bulk making this specific phase of TiO_2 highly interesting for pristine surfaces which are desirable in efficient DSSCs.[209, 210]

4.2.3 STS investigation

The atomic-scale investigation of electronic properties at the TiO_2 interface is of paramount importance as discussed in the following chapters. Figure 4.7 shows a typical scanning tunneling spectroscopy spectrum which was taken on the bare TiO_2 anatase (101) surface by varying the bias voltage in a range between -5 and +2 V. The spectroscopy measurements were performed at 5 K using chemically etched platinum-iridium tips (see Chapter **??**). As revealed in the Figure 4.7, the differential conductance increases in the filled-state region below -2.5 V and in the empty-state region above +0.8 V. At positive bias voltages, the differential conductance shows a slightly higher magnitude compared to the spectra at negative bias. It is important to note that the STS measurements depends for instance on the degree of substrate defect concentrations and the tip condition. The STS spectra shown in Figure 4.7 reveals a typically observed band gap of $\sim$ 3.3 V. As mentioned in Section 4.1.1, the process of electron injection and consequently the overall efficiency of DSSCs is controlled by the energy difference between the conduction band of the TiO_2 material and the LUMO level of the dye. Hence, the possibility of resolving both the conduction and valence band onset of the TiO_2 anatase (101) substrate is of paramount importance when elucidating the charge injection potential of photosensitizers adsorbed on this relevant oxide surface.

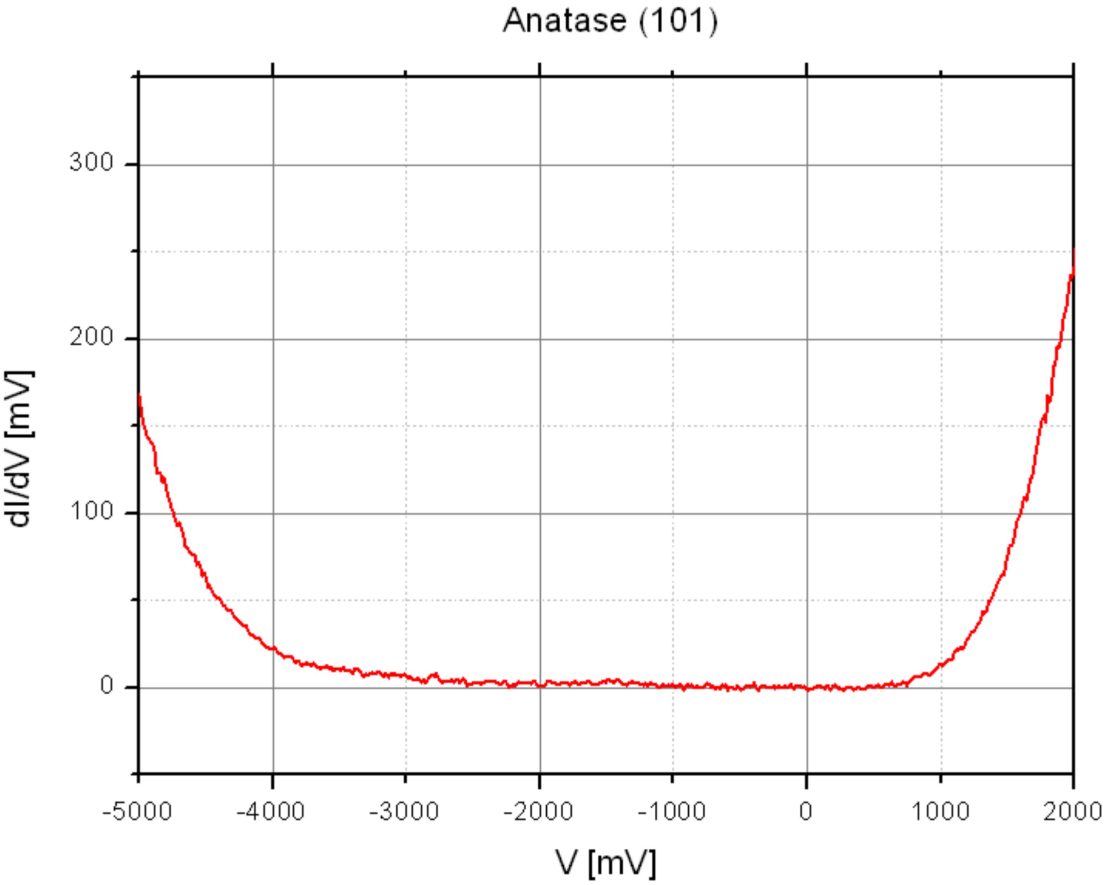

Figure 4.7: Differential conductance spectra taken on TiO_2 anatase (101) in the bias range -5 V to +2 V at 5 K. The conductance increases below -2.5 V and above +0.8 V, respectively.

4.3 Photosensitizer N3 on TiO_2 anatase (101)

As described before in detail, DSSCs constitute a promising approach to sustainable and low-cost solar energy conversion. The overall efficiency of DSSCs is determined by three interdependent dynamical processes, namely photon absorption and electron-hole pair creation, the injection of the photoexcited electron into the conduction band of the semiconductor and the subsequent dye regeneration by the electrolyte (see Section 4.1.1). For these processes, integral time-resolved optical spectroscopic and theoretical methods have provided a great deal of information. The effective operation of the photosensitizers crucially depends on the specific adsorption geometry[159, 211, 212] and consequently, much effort has been dedicated to study the binding configurations of the dye molecules on TiO_2 surfaces. For instance, a highly efficient photosensitizer prevalently coated on the mesoporous TiO_2 films of DSSCs is the N3 dye (cis-di(thiocyanato)-bis(2,2'-bipyridyl-4,4'-dicarboxylate) ruthenium(II)) with a mass of 705.64 dalton.[24] Its chemical structure is shown in the inset of Figure 4.8 (marked in red). However, the determination of the precise N3 adsorption geometry and its associated electronic properties has not been directly achievable so far. In addition, recently proposed supramolecular interactions between N3 dyes lack experimental evidence.[213] The further optimization of DSSCs would greatly benefit from the possibility of correlating photosensitizer adsorption geometries to electronic properties at the dye-substrate interface, i.e. the fundamental understanding of the interfacial properties will provide chemists with specific design rules which enable the synthesis of optimized photosensitizer structures for higher charge injection efficiencies in DSSCs.

Raman spectroscopy and DFT based studies indicate that N3 molecules are in general coordinatively bonded to the fivefold coordinated Ti sites of the anatase (101) surface via the carboxyl groups of their anchoring ligand BINA (2,2'-bipyridyl-4,4'-dicarboxylic acid).[214–216] However, there is profound uncertainty about the number of involved carboxyl groups and the respective binding modes of the partially deprotonated carboxylic groups, i.e. monodentate, bidentate bridging and bidentate chelating (see Section 4.1.3). Studies on the readily accessible TiO_2 rutile (110) surface report ambiguous N3 anchoring either only via two carboxyl groups,[217, 218] or mixed-binding involving both carboxylate groups and sulphur atoms of the N3's thiocyanate ligand.[219] Experimental data for the relevant TiO_2 anatase is scarce, but vibrational spectroscopic and x-ray photoemission spectroscopy investigations indicate adsorption of the Ru-based dyes via two deprotonated carboxylate groups either in a bidentate chelate or in a bridging coordination.[195, 220, 221] DFT based molecular modelling proposed the thermodynamically most stable N3 anchoring to be given by a bidentate configuration of the BINA ligand.[222] In addition, the stabilizing role of surface hydroxyl groups and supramolecular interactions between the photosensitizers through hydrogen bonds were recently discussed.[213,223] Despite previous experiments and theoretical studies, the experimental investigation of individual N3 photosensitizers on atomically well-defined TiO_2 rutile and anatase surfaces at the molecular level has not been achieved so far. The lack of atomic-scale studies is mainly attributed to the major obstacle of sample preparation as discussed in Section 4.2.1. Deposition techniques such as substrate immersion in N3 solution prevailed high-resolution imaging and characterization of the dye-substrate interface.[217,218] Here we address the challenge of investigating both the adsorption geometry and electronic characteristics of the photosensitizer N3 adsorbed on TiO_2 anatase (101) with single molecule sensitivity.

4.3.1 Electrospray ion beam deposition of intact N3

In this study, a natural TiO_2 anatase single crystal with (101) surface orientation was employed (see Section 4.2.2). Complex functional photosensitizer molecules typically have a low vapor pressure which represents a major problem for their analysis by means of scanning probe microscopy and other UHV-based advanced characterization techniques. In fact, such molecules decompose before being sublimed and therefore cannot be deposited onto clean surfaces in UHV by traditional molecular beam evaporation techniques. Hence, the photosensitizer N3 was brought onto the atomically well-defined substrate by means of electrospray ion beam deposition technique (see Section 1.3). For deposition, N3 molecules (supplier: Sigma-Aldrich, 703206) were dissolved in ethanol (supplier: Sigma-Aldrich, 34998) at a concentration of 10^{-4} M. A high efficiency nano electrospray ionization source was used in negative ion mode to generate the ions at a spray voltage of 3500 V. The top row of Figure 4.8 shows a typical ESI time-of-flight mass spectrum of the N3 ion beam containing both differently charged N3 molecules (M^{-}, M^{2-}, M^{3-}) by likely proton abstraction from the carboxylic groups and fragments (M^{2-}-S). To avoid any contamination at the surface, the ion beam was mass selected to transmit only the peak at 705 thomson, which corresponds to the singly negative charged N3 ion. The ESI-TOF spectrum of the mass-selected N3 ion beam is shown at the bottom of Figure 4.8. The kinetic energy of the singly ionized N3 molecules was measured at values of 35 - 50 eV and the bias at the sample was set to 30 - 45 V respectively, which led to N3 deposition energies of $\sim$ 5 eV. At the target in UHV, mass selected ion currents of 60 - 120 pA were measured.

It was further made sure that the fragile N3 molecules survive the ESI deposition procedure by choosing minimal kinetic energies of 5 ± 2 eV. The intactness of

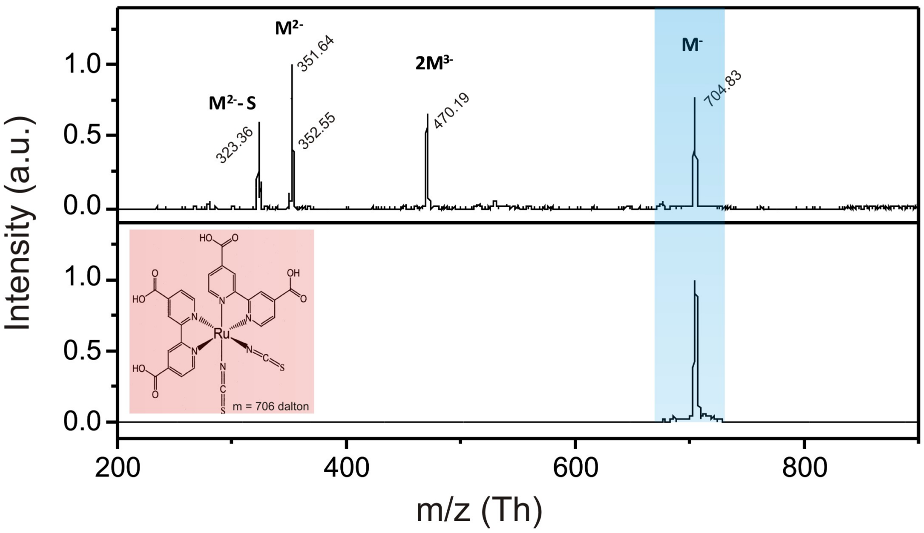

Figure 4.8: Typical ESI-TOF mass spectrum of the N3 ion beam before (top) and after (bottom) mass-selection of the singly-ionized N3 molecules (704.83 Th, marked in blue). Only singly negative ionized N3 molecules were deposited on the TiO_2 anatase (101) surface by ES-IBD. The chemical structure of the N3 dye is shown in the inset (marked in red).

the N3 molecules upon substrate adsorption was verified by soft cluster-induced desorption (SCID) experiments.[224] This technique employs neutral SO_2 clusters which are seeded in a helium beam and hit the collision target in UHV (see Figure 4.9a). Five N3 samples on gold substrates were prepared: four samples onto which N3 molecules were deposited by ES-IBD (charge ~ 50 pAh) at different kinetic energies (3/8/20/50 eV) and one sample by simply drop casting the respective N3 solution. Upon impact of the neutral cluster beam on the sample surface, the abundant formation of free N3 ions was detected with a pulsed time-of-flight mass spectrometer which is oriented perpendicular to the beam axis. The corresponding mass spectrum is shown in Figure 4.9b. The spectrum of the drop-cast sample can be considered as a reference showing intensity peaks at 705 thomson and around 1400 thomson. These peaks correspond to the singly-ionized (M^{1-}) and two coupled singly-ionized ($2M^{1-}$) N3 molecules, respectively. Importantly, compared to the ES-IBD prepared samples, the major peaks of the singly-ionized N3 molecules remain and no additional strong peaks arise. This shows that even at a N3 deposition energy of 50 eV, the vast majority of adsorbates are intact N3 molecules. Accordingly, the kinetic energy upon adsorption gets transferred to internal degrees of freedom of the N3 molecule[225, 226] keeping the photosensitizer intact.

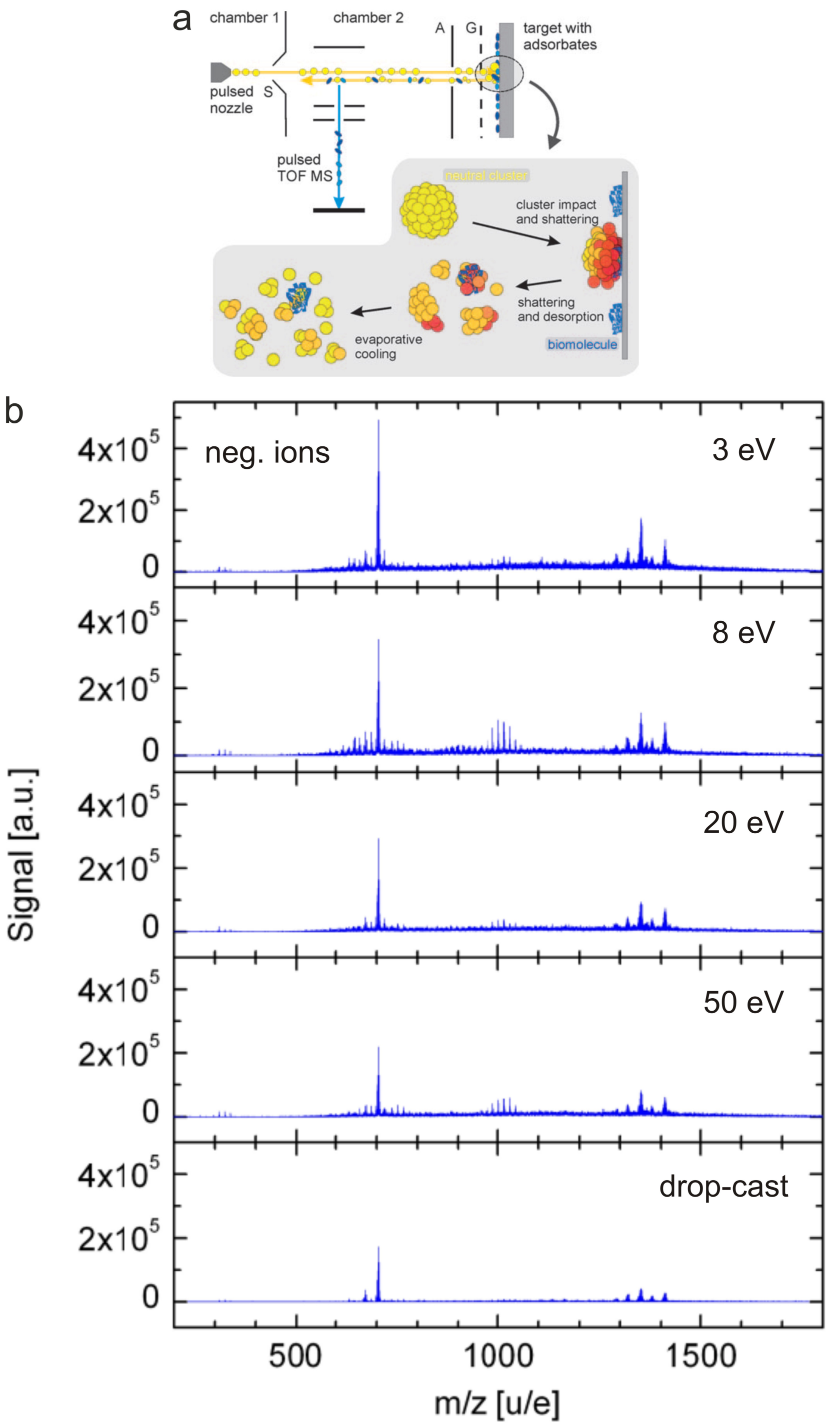

Figure 4.9: (a) Upper left: schematic depiction of the cluster-impact experiment. After the neutral cluster beam hits the N3/Au(111) sample surface, charged fragments carrying N3 molecules are extracted by the biased grid (G). Mass analysis is performed in the TOF mass spectrometer oriented perpendicular to the primary beam. Skimmer (S) and aperture (A) allow for beam collimation. Lower right: schematic depictions of cluster impact and subsequent desorption of biomolecules from a surface (Taken from ref. 224). (b) TOF analysis of N3 desorbed by neutral SO_2 clusters from Au(111): N3 dyes deposited by means of electrospray ion beam deposition method (top four spectra) and drop-cast method (bottom spectrum) on Au(111).

4.3.2 Mobility and formation of dye assemblies

Figure 4.10 shows STM images of the bulk-terminated TiO_2 anatase (101) surface revealing typical flat terraces with an average width of $\sim$ 20 nm and characteristic trapezoidally shaped islands. The monoatomic steps are preferably orientated along the [010], $[11\bar{1}]$ and $[\bar{1}11]$ directions (see Section 4.2.2). The bright particles protruding by $\sim$ 6 Å and a lateral diameter of $\sim$ 15 Å are assigned to intact N3 molecules.

At low N3 coverage (charge 15 pAh, Figure 4.10a), initial N3 adsorption is evidently preferred close to step edges without any preference of a particular step orientation. Moreover, only few N3 molecules adsorb isolated on terraces. As the coverage is increased (charge 30 pAh, Figure 4.10b), N3 molecules assemble into larger two-dimensional clusters and chains both close to step edges and on terraces. The formation of dye clusters is further revealed in Figure 4.11a and 4.11b, respectively. In absence of molecular diffusion, a spatially random adsorption of N3 molecules would be expected due to the strong anchoring via the carboxylic groups. However, the preferred N3 binding at step edges and the formation of N3 assemblies revealed in Figures 4.10 and 4.11 indicate a certain mobility of the N3 molecules in their physisorbed or chemisorbed state. The time between the deposition and the measurement at 5 K amounts to several hours ($\sim$ 8 h). During this time, the substrate is at room temperature and N3 might diffuse through a sequence of intramolecular transitions overcoming existing energy barriers, whose calculation is a challenging task not achieved so far. However, the energetics can be estimated from the diffusion barrier of a single benzoic acid adsorbed in a bidendate manner on TiO_2 rutile (110) along the (001) direction that was calculated to $\sim$ 0.55 eV.[227] Compared to rutile (110), the large surface corrugation at the anatase (101) induces a high degree of diffusion anisotropy potentially leading to an increase of the N3 diffusion barrier. Further, the N3 diffusion barrier depends on the number of carboxylate groups involved in the coordination to the anatase (101). In order to gain further insights into the N3 diffusion, the binding behaviour of its bare anchoring ligand BINA is studied in Section 4.4. Moreover, intrinsic surface defects such as step edges and defect sites[210] of the anatase (101) represent special adsorption sites (see Section 4.1.2) and local electric fields could contribute to the immobilization of N3 molecules close to these sites as observed in Figure 4.10 and 4.11. The role of a potential physisorbed intermediate state in the adsorption and anchoring process needs to be considered as well.

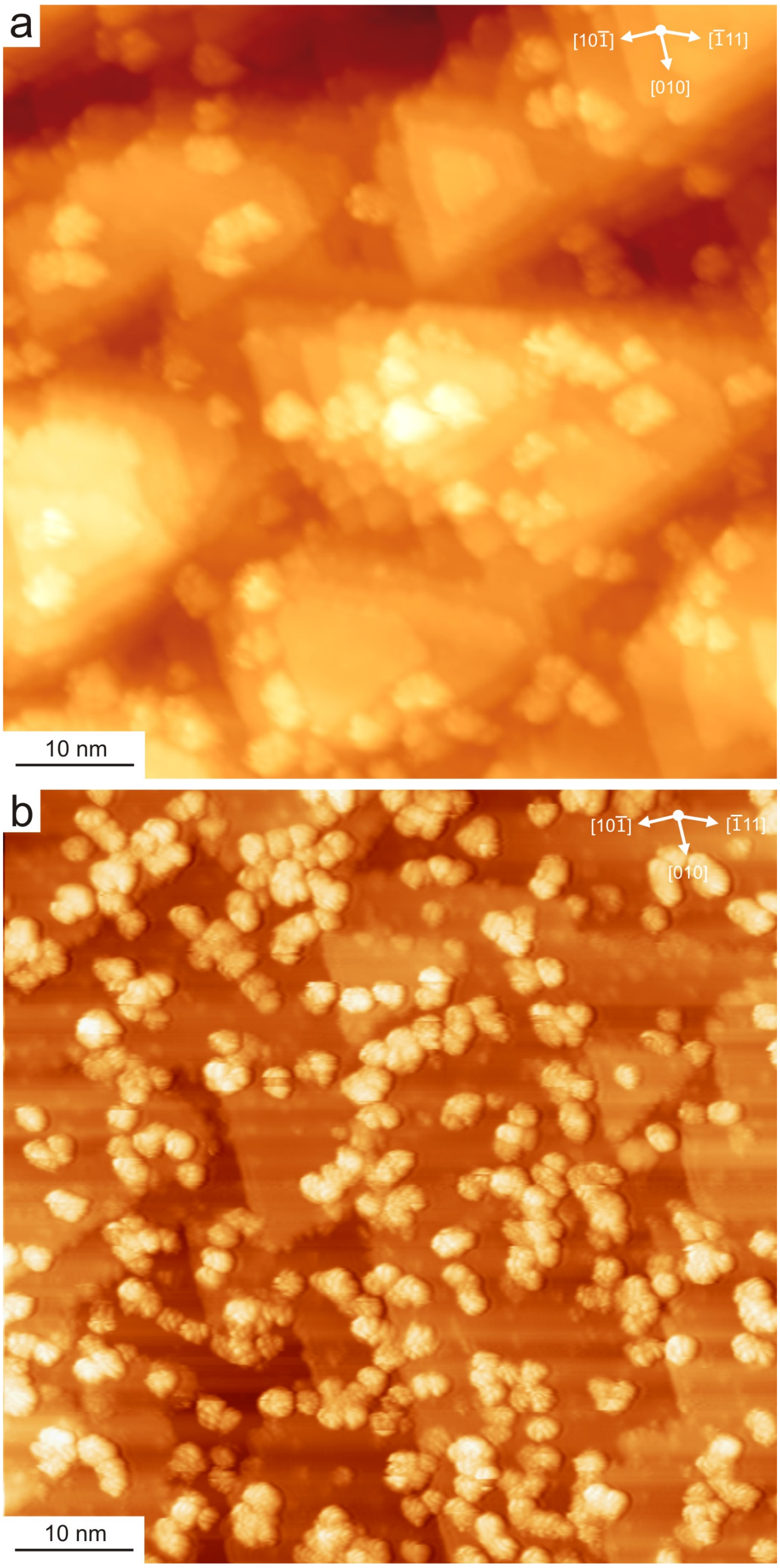

Figure 4.10: Photosensitizer N3 adsorbed on TiO_2 anatase (101). (a) STM overview image at low N3 coverage (charge 15 pAh, 2.04 V, 0.06 nA, 5 K). (b) STM image at middle N3 coverage (charge 30 pAh, 1.99 V, 0.15 nA, 5 K). The crystallographic directions of the substrate were assigned according to Ref. 175.

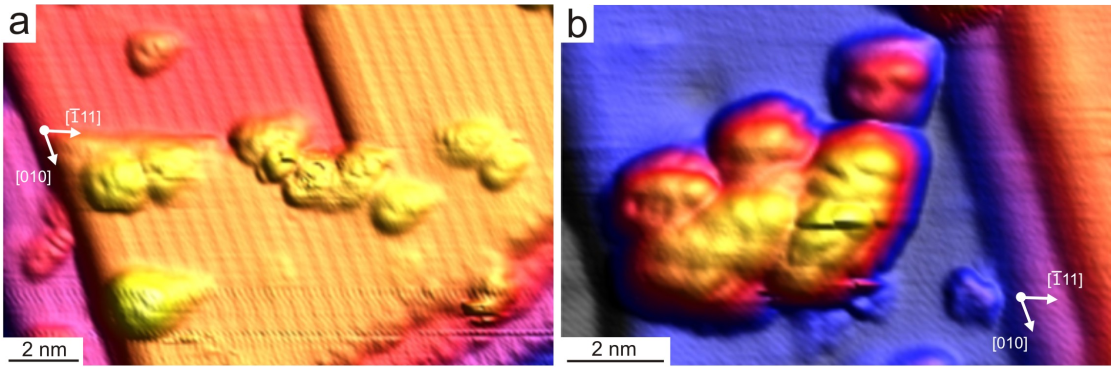

Figure 4.11: Photosensitzer N3 adsorbed on TiO_2 anatase (101). Clustering at (a) step edge (1.98 V, 0.08 nA, 5 K) and (b) on terrace (1.80 V, 0.06 nA, 5 K).

4.3.3 Multi-conformational binding geometries

Figure 4.12 shows a high-resolution STM image revealing individual N3 molecules with submolecular structure adsorbed on atomically resolved anatase (101). Surprisingly, each N3 molecule reveals a different shape and inner structure whereas the apparent height is very similar ($\sim$ 6 Å). While the top left and bottom N3 molecules are characterized by broad protrusions, the top right and middle N3 molecules rather show oval adsorption geometries. This observation gives direct hint to multi-conformational N3 binding geometries.

Following theoretical approach was pursued to model the experimental findings. First, the electronic structure of an intact N3 molecule was obtained by densitiy functional theory in absence of the substrate. Calculations were performed within a generalized-gradient approximation to density-functional theory [28]. The core-valence interaction was taken into account using ultrasoft pseudopotentials.[228] Periodic boundary conditions and plane-wave basis sets were used as implemented in the Quantum ESPRESSO package.[229] The electronic wavefunctions and densities were expanded up to kinetic energy cutoffs of 35 and 200 Ry, respectively. For the calculations on the isolated N3 dye, a simulation cell of dimensions 32×32×32 Å^3 was used, and the Coulomb interaction between periodic replicas was removed via the truncation technique of Ref. 230. The relaxed structure of the gas-phase molecule was obtained by minimising the forces until the total force on each atom was less than 25 meV/Å. STM images of the dye were simulated in the Tersoff-Hamann approach.[69] The local density-of-states (LDOS) was integrated up to 1 eV above the N3 LUMO and plotted on a logarithmic scale. A large number of different geometries were investigated by randomly varying the orientation of the molecule. For each case, the map was calculated on a plane located 3 Å above the furthest atom from the (virtual) TiO_2 surface. The DFT-calculated maps which correspond most closely to the experimental STM maps of Figure 4.12a are displayed in Figure 4.12b. In general, the calculated STM maps show the particular electronic features of the main ligand parts, i.e., the thiocyanate, phenyl and carboxylic group, sticking out of the surface. For instance, the thiocyanate group is imaged as a single round protrusion while the carboxylic group features a double lobe structure as can be seen in the upper right and bottom simulation in Figure 4.12b. Molecules having a different orientation are imaged asymmetrically

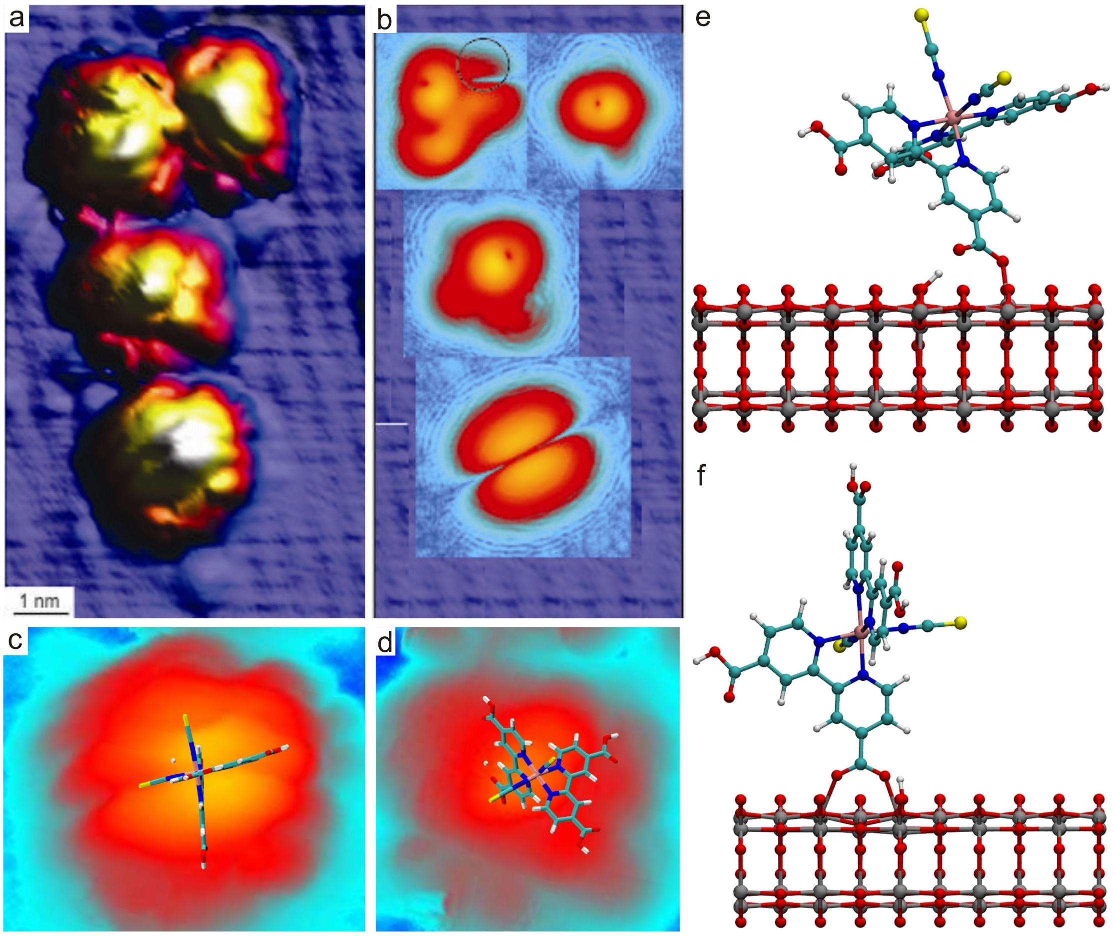

Figure 4.12: Individual N3 molecules on TiO_2 anatase (101). (a) High-resolution STM image revealing multi-conformational N3 adsorption geometries and submolecular N3 structure at atomic substrate resolution. Top two N3 molecules form a dimeric supramolecular assembly (1.72 V, 0.06 nA, 5 K). (b) DFT-calculated maps which correspond most closely to the experimental STM map neglecting substrate influence. Realistic placement of the N3 model on the experimental STM map of the (c) bottom and (d) middle N3 molecule. Ball-stick model of the coordination geometries of the (e) middle and (f) bottom N3 molecules. (1.72 V, 0.06 nA, 5 K)

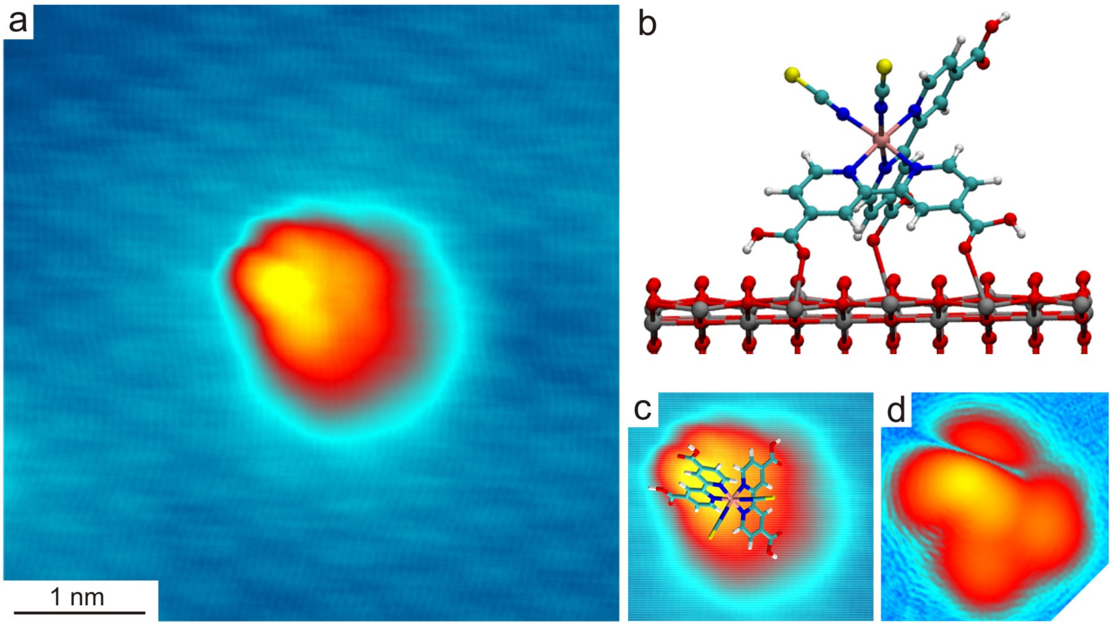

Figure 4.13: (a) STM image of an individual N3 dye with atomically resolved substrate (2.0 V, 0.2 nA, 5 K). (b) Corresponding ball-stick coordination geometry including three carboxylic groups binding to the substrate in unidendate modes. (c) Realistic N3 model overlayed to STM topograph. (d) Corresponding Tersoff-Hamann STM simulation.

and show lobes originating from different parts of the ligand. In this way the best theoretical fit structure for the experimental topographs was obtained. Figure 4.12c and 4.12d show the experimental STM maps of the two bottom N3 molecules with the best fitting N3 model overlayed. The corresponding ball-stick models of the N3 - anatase (101) interface are shown in Figure 4.12e and 4.12f (models of the top two N3 molecules see below). The specific N3 binding geometries are derived from a realistic placement of the molecules on the substrate, and vary from the unidentate to the bidentate bridging mode.

In most cases, the access of the energetically most favourable N3 configuration seems to be kinetically hindered due to insurmountable barriers at room temperature. The observation of multi-conformational N3 binding geometries indicates that the N3 molecules are frequently trapped in local energy minimum configurations. Rarely, N3 adsorption geometries in the lowest energetical configuration were observed. Figure 4.13a shows a high-resolution STM image of a single N3 molecule on the atomically resolved TiO_2 anatase (101). The corresponding ball-stick binding model for this particular case is shown in Figure 4.13b, Figure 4.13c shows the N3 model overlayed to the STM image and the corresponding DFT map is depicted in Figure 4.13d. In this N3 adsorption geometry, three carboxylic groups bind to the substrate in unidendate modes. According to Ref. 213, this configuration is the energetically most favorable one owing to the minimum strain exerted on the dye molecule. However, in general, even energetically less favorable configurations such as the unidentate mode involving a hydrogen bond to the surface or the bidentate bridging mode including only one out of four N3 carboxylate groups are observed (see Figure 4.12). These findings indicate that the adsorption energetics of the interface models is not a reliable quality indicator and that kinetics fundamentally influences the N3 adsorption behaviour. Note that by the examples given here, the participation of the thiocyanato ligands in the substrate bonding for other not identified N3 adsorbates cannot be excluded. The multitude of observed configurations is even more surprising considering the residual ion kinetic energy of ~ 5 eV that could provide for a transient mobility after deposition giving additional impetus to overcome energy barriers.

4.3.4 Supramolecular interaction

The two top N3 molecules revealed in Figure 4.12a are shown in greater detail in Figure 4.14a. Compared to the two bottom N3 molecules (Figure 4.12), they are further characterized by an elongated intermolecular protrusion which gives strong hint to the formation of a dimeric N3 assembly. The corresponding DFT

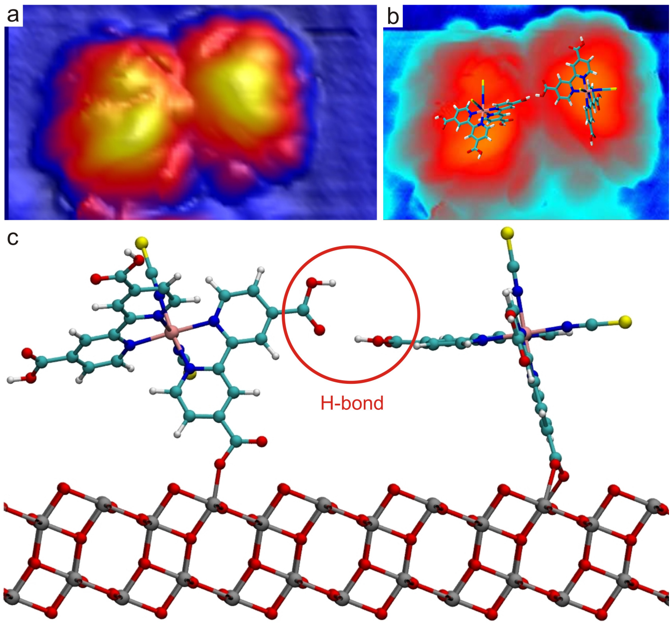

Figure 4.14: (a) STM image of the two top N3 molecules from Figure 4.12a forming a dimeric supramolecular assembly (1.72 V, 0.06 nA, 5 K). (b) N3 binding models overlayed to the STM image. (c) Ball-stick representation of best-fitting DFT model with a hydrogen bond interconnecting both N3 dyes.

structures and binding modes are shown in Figure 4.13b and 4.13c, respectively. In this proposed configuration, the left N3 molecule forms a unidentate linkage to the substrate whereas the right one coordinates in the bidentate bridging configuration. Particularly, this configuration allows the formation of a hydrogen bond interconnecting both N3 carboxylic groups. These findings support the recently proposed supramolecular interactions between N3 molecules based on the reverse-engineering of core-level spectra.[213]

4.3.5 N3 charge injection potentials

As discussed in Section 4.1.1, the process of electron injection in DSSCs is crucially determined by the energy difference between the LUMO level of the photosensitizer and the conduction band of the TiO_2 substrate. Since the N3 molecules coordinate in various different ways to the TiO_2 surface (see before), an important question directly relating to the DSSC performance arises: do the specific N3 adsorption configurations have an influence on the respective dye LUMO level relative to the

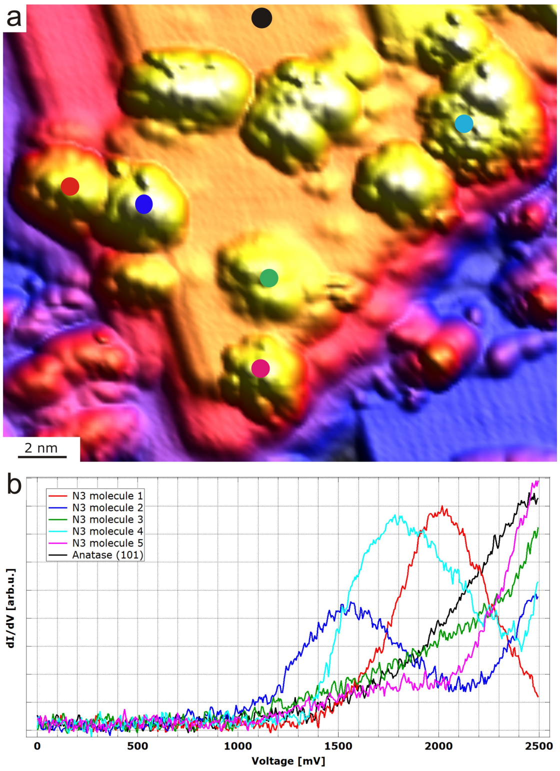

Figure 4.15: (a) STM overview image of various different N3 adsorption configurations on TiO_2 anatase (101) (1.98 V, 0.08 nA, 5 K). (b) Corresponding dI/dV spectra taken at positions indicated in (a).

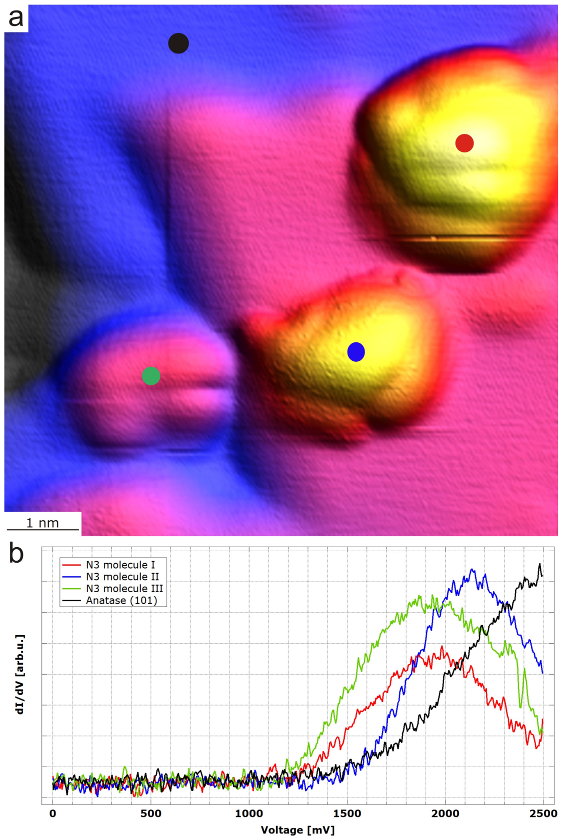

Figure 4.16: (a) STM overview image of N3 adsorption configurations on TiO_2 anatase (101) (1.98 V, 0.09 nA, 5 K). (b) Corresponding dI/dV spectra taken at positions indicated in (a).

substrate conduction band? Are there preferential N3 adsorption geometries which promote an efficient charge transfer from the dye into the substrate by effectively coupling to the TiO_2 surface? It was shown in Section 4.2.3 that both the substrate HOMO and LUMO can be revealed by STS. The onset of the TiO_2 conduction band lies at about + 0.8 eV and the valence band maximum is found at $\sim$ -2.5 eV. Here we adress the challenge of characterizing individual N3 molecules adsorbed on TiO_2 anatase (101) by means of STS. Note that STS of the occupied states is unstable due to the dye's HOMO levels being inside the TiO_2 band gap and corresponding discharging of the N3 when approaching the HOMO. Hence, the STS spectra were recorded in the positive bias voltages range. Figure 4.15a shows a STM overview image of N3 molecules which are adsorbed in various different configurations on TiO_2 anatase (101). Figure 4.15b reveals the corresponding differential conductance spectra of both the substrate (black line) and the individual N3 molecules (coloured lines) which were recorded as indicated in the figure. The STS spectra of the individual N3 molecules show a strong variation in the LUMO energetic position

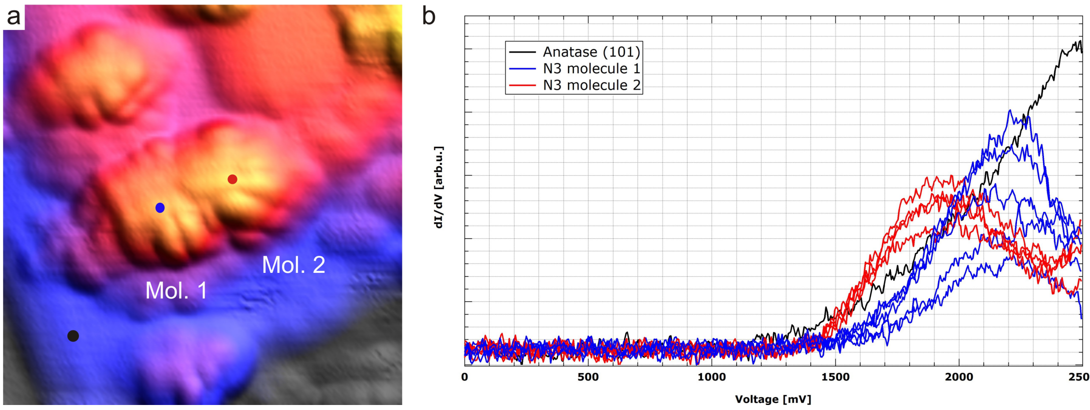

Figure 4.17: (a) STM overview image revealing a dimeric N3 assembly (Mol. 1 and Mol. 2) on TiO_2 anatase (101) (1.8 V, 0.08 nA, 5 K). (b) Corresponding dI/dV spectra taken at positions indicated in (a).

up to $\sim$ 1 eV. These findings are of paramount importance since they indicate with single molecule sensitivity the fundamental dependence of the N3 LUMO positions on the specific N3 coordination mode. Since the dye LUMO position varies in such strong manner, even adsorbtion geometries where the dye LUMO states lie below the conduction band minimum are conceivable. In this case, not all photoabsorbers would contribute to the photovoltage. Figure 4.16a shows three N3 molecules adsorbed on the TiO_2 anatase (101). The two bottom molecules are characterized by quite similar topographical shapes. However, even such little variations between these N3 adsorption geometries are directly visualized in differing STS spectra which are shown in Figure 4.16b. Figure 4.17a shows a dimeric N3 assembly on TiO_2 anatase (101) which was characterized by means of STS. Figure 4.17b shows the corresponding differential conductance spectra. The N3 molecules can be nicely distinguished by their LUMO levels (Mol. 1: 2.25 V, Mol. 2: 1.94 V). These findings provide the possibility to perform STS calculations and learn from theory the change in energy alignment upon mutual dye interaction.

4.3.6 Monolayer of N3

To complete the investigation of the N3 molecules on TiO_2 anatase (101), a N3 monolayer sample (deposited charge 90 pAh) was prepared. Figure 4.18 shows the TiO_2 substrate at full N3 coverage where an underlying molecular ordering is not directly visible. In some areas (marked by white circle), the formation of chain-like structures can be observed. This finding could potentially support the recently suggested self-assembly of hydrogen-bonded N3 molecules in chains.[231] Furthermore, Figure 4.18 gives a realistic scenario for DSSCs.

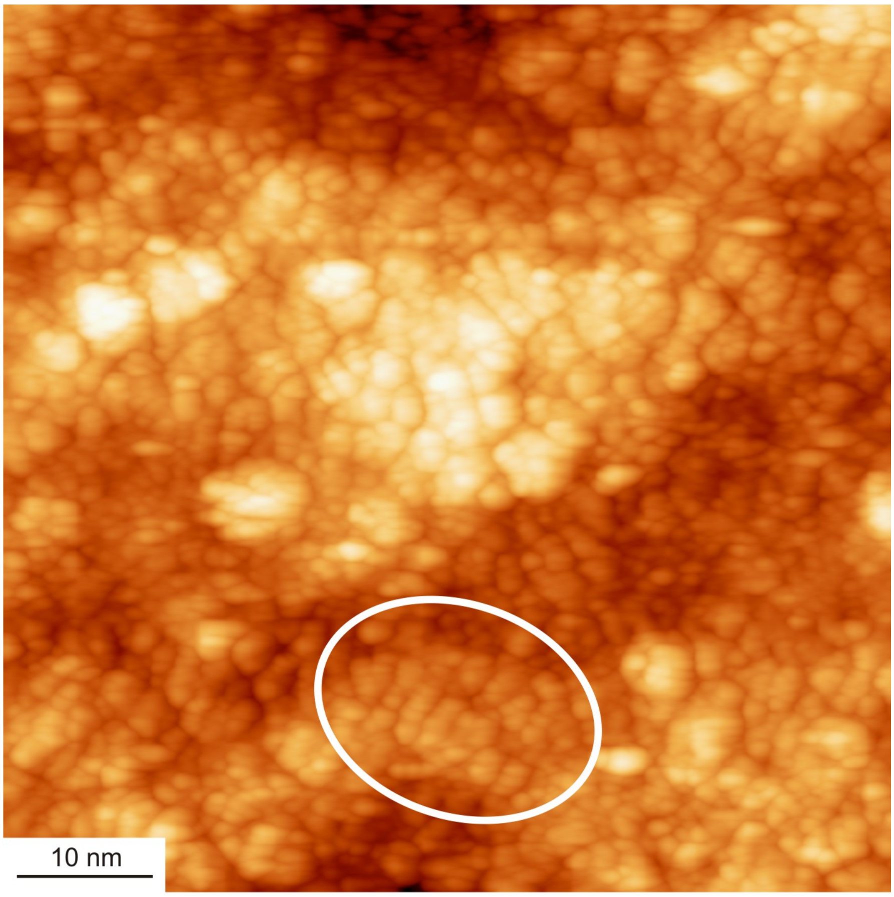

Figure 4.18: STM image of a monolayer N3 (deposited charge 90 pAh) adsorbed on TiO_2 anatase (101) (2.08 V, 0.07 nA, 5 K). Formation of chain-like structures can be observed (area marked by the white circle).

In conclusion, our studies provide first atomic-scale insights into the structure-property relationship of the photosensitizer N3 adsorbed on the relevant TiO_2 anatase (101). The local structure of N3 molecules was probed with single molecule sensitivity revealing a multitude of different N3 binding geometries on the oxide surface. The specific N3 binding geometries were derived by DFT simulations and vary from the unidentate to the bidentate bridging mode involving various carboxylate groups. This indicates that the N3 molecules are frequently trapped in local energy minimum configurations and demonstrates the essential influence of adsorption kinetics on the N3 binding geometry. Further, our studies revealed the formation of supramolecular dye assemblies. The strong influence of specific N3 adsorption geometries on its electronic properties, i.e. the N3 LUMO level with respect to the substrate Fermi level, was demonstrated. Our experimental findings supported by DFT-based calculations show that understanding the kinetics of the N3 molecule is essential to control both the adsorption geometry and the diffusion of

N3 on the TiO_2 anatase (101) surface. The present work carries direct relevance to the optimization of the quantum yield of DSSCs, enhance their stability and design more efficient dyes.[232] Even in the early stages of development, photosensitizers can be probed with molecular sensitivity on relevant TiO_2 surfaces which allows preselection of highly suitable chemical structures. The experimental procedure can be directly extended to new dye molecules and a variety of different substrates. Furthermore, the atomic-scale insights pave the route towards achieving optimum dye coverages and enhanced structural stability of the dye-substrate interface. Finally, the present work provides an experimental basis for important theoretical investigations in the future.

4.4 Dye anchoring ligand BINA on TiO_2 anatase (101)

It was shown in Section 4.3 that the polypyridyl complex N3 coordinates in various different adsorption geometries via carboxylate groups of its anchoring ligand to the TiO_2 anatase (101) surface. STM and STS investigations further gave evidence that the electronic properties of N3 dyes, i.e. the dye LUMO level with respect to the substrate Fermi level, depend on the specific molecular adsorption geometry. This finding is of paramount importance for increasing charge injection efficiencies in DSSCs and additional insights into the specific photosensitizer coordination geometries would be advantageous. Here we study the adsorption geometry of the anchoring ligand of the photosensitizer N3 (BINA, 2,2'-bipyridyl-4,4'-dicarboxylic acid,[158,233,234] cf. Figure 4.19) on TiO_2 anatase (101) by means of STM at 5 K combined with DFT-based calculations. Revealing the BINA binding characteristics with single molecule sensitivity will contribute to understanding the multi-conformational binding geometries of the N3 dye in more detail. Previous work has shown that the BINA ligand provides a route for ultra-fast electron transfer from the photosensitizer into the conduction band of the substrate on a femtosecond timescale.[235] Consequently, its integrity is critical to the function of DSSCs which are based on this molecular anchoring ligand.

Details of the BINA configuration geometry on well-defined TiO_2 anatase (101) still lack experimental evidence at the atomic level. Strongly surface-bonded N3 dyes can be expected to be more favorable than a weakly adsorbed dye with an undeformed surface-binding BINA.[236] The high flexibility of the BINA molecules has been evidenced with rather strong twists between its two pyridine rings.[237–240] A theoretical study of the BINA adsorbed on TiO_2 anatase (101) indicated that the lowest energy configuration for this system is the bridging bidendate adsorption mode (see Section 4.1.3) involving both carboxyl groups.[237,241] This means the deprotonated carboxylate oxygen atoms of each pyridyl ring bind to neighbouring Ti atoms along the Ti rows rather than to one Ti atom in a chelate-like geometry.[242] Further theoretical works on the adsorption of the BINA molecule on anatase (101) surfaces using the large unit cell periodic approach[236,243] and semiempirical techniques[239] have been reported. Apart from theoretical studies, UHV experiments have been recently carried out to study the adsorption geometry of the bare BINA molecule on TiO_2 surfaces.[241,244] The general consensus now seems to be that at least a fraction of the carboxylic groups of the BINA ligand are deprotonated and coordinate to the TiO_2 substrate.[220,222] In addition, core-level spectroscopy (XPS and XAS) studies of intermolecular hydrogen-bonding in thick films of BINA

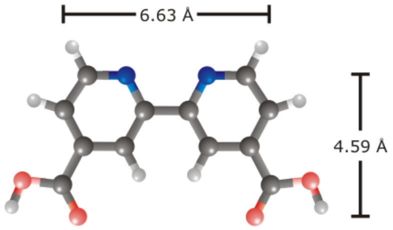

Figure 4.19: Chemical structure of the cis-confomer of the bi-isonicotinic acid (2,2'-bipyridyl-4,4'-dicarboxylic acid).

on TiO_2 rutile (110) were reported.[245] NEXAFS investigations also focused on the BINA bonding to TiO_2 rutile (110).[239] However, previous studies have not been sufficient to determine the full atomic-level details of the BINA coordination geometry on the relevant TiO_2 anatase (101) surface.

STM study of BINA on TiO_2 anatase (101)

Atomically well-defined TiO_2 anatase (101) surface was prepared following the procedure described in Section 4.2.1. BINA (supplier: Sigma-Aldrich, 550566) was thermally evaporated at 520 K (see Section 1.2) in UHV onto the substrate which was kept at room temperature during dosing. Subsequently, the sample was cooled down to 5 K. The STM measurements were performed in the constant current mode using chemically etched platinum iridium tips. Figure 4.20 shows a high-resolution STM overview image of the BINA molecules adsorbed on TiO_2 anatase (101). Numerous different molecular adsorption shapes are revealed on the atomically resolved substrate. Two adsorption structures can be observed more frequently: u-shape (20 %) and three-lobe shape (13 %) BINA geometries as highlighted in Figure 4.20.

The u-shape BINA configuration is shown in greater detail in Figure 4.21a. It reveals a significant circular protrusion in the molecule center and an extended u-shape protrusion around the molecule center. Besides some additional adsorbates revealed in the STM image, this STM topograph represents the typically observed u-shape BINA and allows detailed analysis due to the atomically resolved substrate. In this configuration, the BINA molecules show a preferential binding angle of $\sim$ -45° and 39° relative to the [010] direction of the atomically resolved substrate as indicated in Figure 4.21a. In order to elucidate the underlying coordination mode, DFT-based simulations of the STM data were performed. For calculations of the BINA molecule on the TiO_2 surface, a twelve-layer anatase TiO_2 slab of dimensions 20.9 × 19.0 Å was used as in Ref. 213. Periodic images of the slab were separated

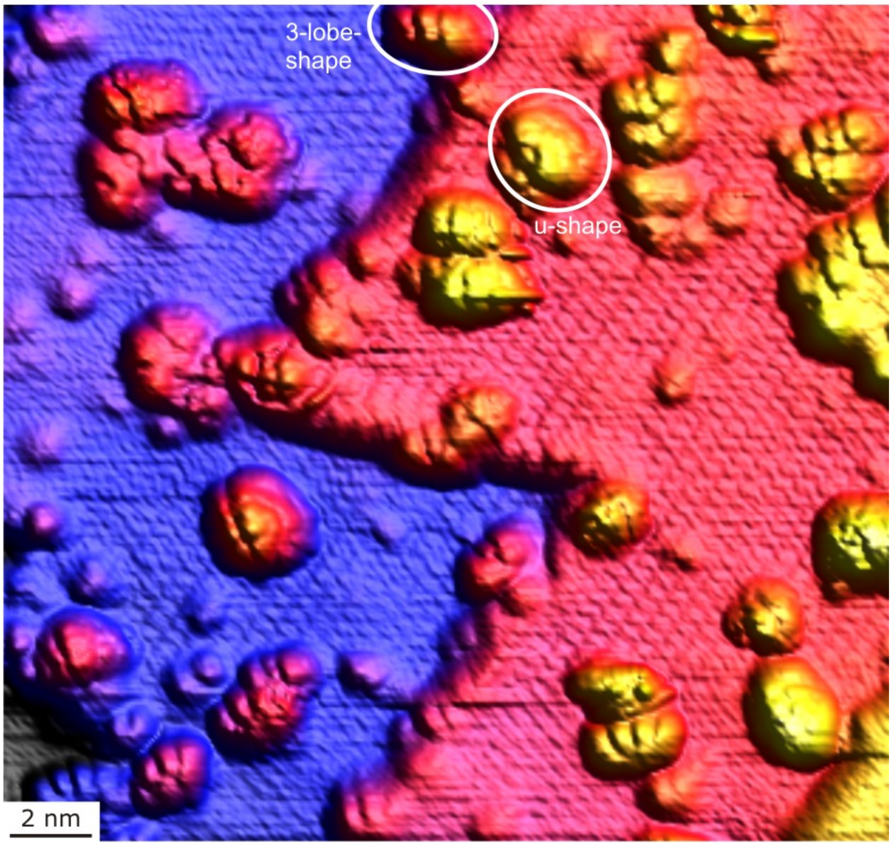

Figure 4.20: High-resolution STM overview image of the photosensitizer ligand BINA (2,2'-bipyridyl-4,4'-dicarboxylic acid) on TiO_2 anatase (101). Various different BINA adsorption configurations are revealed on the atomically resolved substrate (1.75 V, 0.08 nA, 5 K).

by a vacuum region of 22 Å. A single BINA molecule was adsorbed on the slab and relaxed with the same 25 meV/Å force criterion as for the isolated N3 dye. The Tersoff-Hamann STM images were obtained by integrating the LDOS up to 1.2 eV above the anatase conduction band edge. This integration bound correctly captures the contribution from the LUMO of BINA, whose energy is calculated to be 1 eV above the conduction band edge. The map was calculated on a plane located 2 Å above the extremal BINA atom.

Among the various different BINA configurations revealed in Figure 4.20, the most frequently observed u-shape was modeled by DFT. The calculated overall molecular shape shown in Figure 4.21b (bottom) represents the best fitting model at present. It shows highly similar features compared to the STM map of the u-shape BINA (Figure 4.21a) revealing a circular protrusion in the molecule center and a extended overall u-shape. The corresponding ball-stick model of this BINA

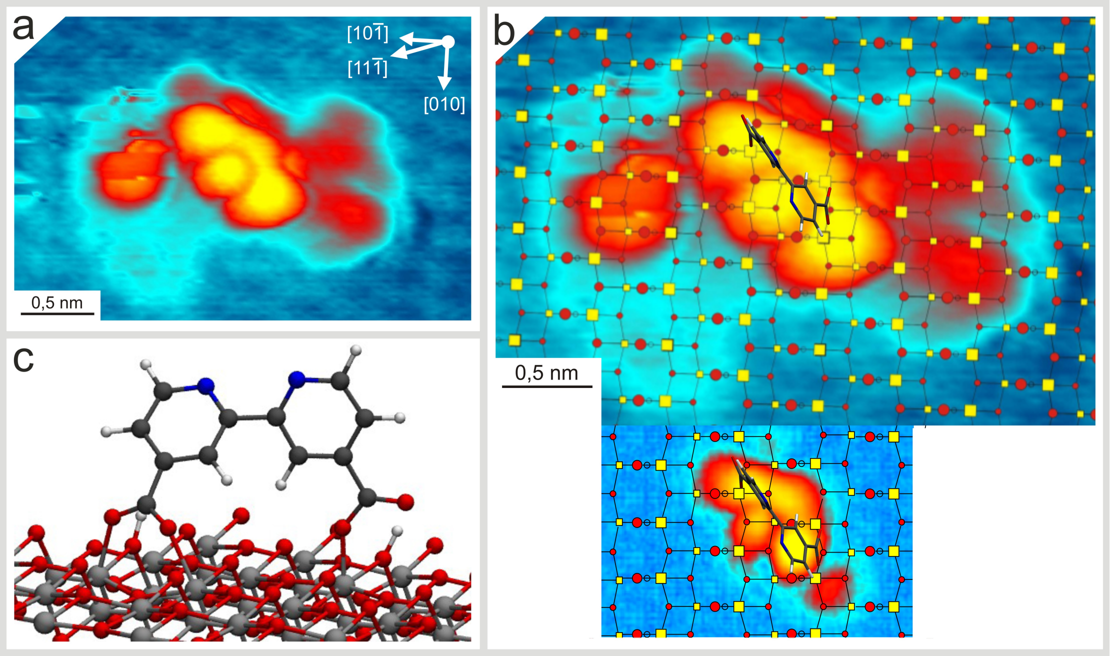

Figure 4.21: U-shape BINA adsorption configuration on TiO_2 anatase (101). (a) High-resolution STM image of the BINA molecule (2.0 V, 0.3 nA, 5 K). (b) Corresponding substrate and BINA overlayed on the atomically resolved substrate of the STM map. (c) DFT ball-stick model of the BINA adsorption configuration. (d) Corresponding DFT map of the BINA u-shape with molecule model overlayed.

adsorption geometry is shown in Figure 4.21c. In this particular configuration, both carboxylic groups are deprotonated and two bidentate bridging modes are formed with one elongated Ti-O bond and a substantial twist between the pyridine rings. The BINA model overlayed to the DFT map (Figure 4.21d) shows that the two main protrusions of the u-shape result from the pyridyl rings of the BINA. The circular protrusion at the center is attributed to one nitrogen atom of the bipyridyl complex while the additional lobe in the bottom right corner of the DFT map arises from one of the pyridine rings. Furthermore, the binding angle of the calculated structure matches well with the experimental observation ($\sim$ -45° relative to the [010] substrate direction) which strongly supports the theoretical model. However, the present DFT simulations still show some deviations to experimental findings. Figure 4.21b (top) shows the STM map of BINA with overlayed atomic substrate lattice and the suggested BINA model. The adsorbed molecule appears as large and bright oval spot in between two adjacent titanium rows. Zooming in the DFT plot with the substrate and comparing the positions of the bright spots to the atoms on the surface, the correspondence of the theoretical findings to the experimental modeling (see Figure 4.21b (bottom)) appears to be incidental. In terms of scale, the experimental picture occupies a larger area. Currently ongoing calculations

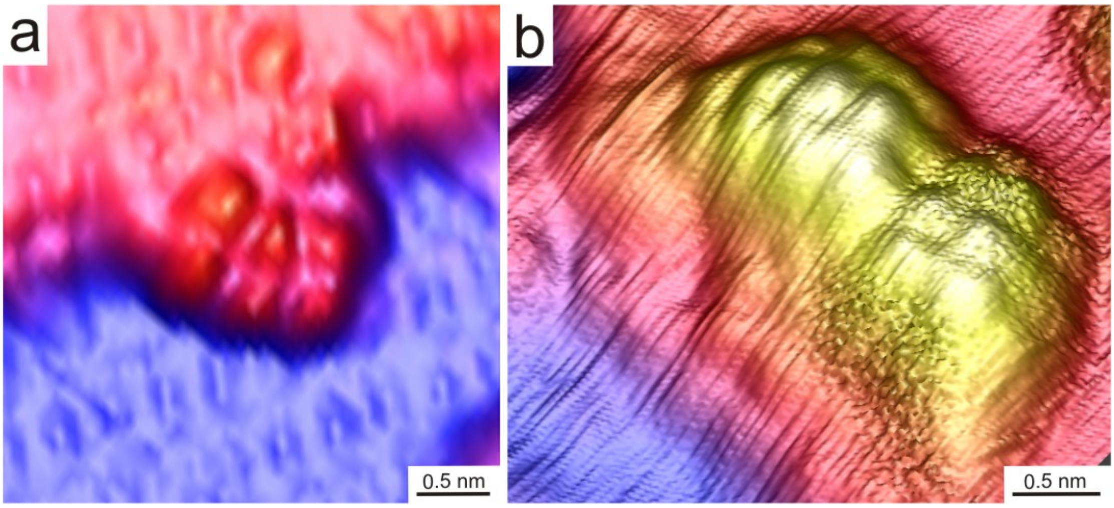

Figure 4.22: High-resolution STM image of a second BINA configuration regularly observed on TiO_2 anatase (101). (a) Single BINA ligand binding at a step edge (1.8 V, 0.07 nA, 5 K). (b) Formation of a type II BINA dimer (1.7 V, 0.08 nA, 5 K).

will clarify these slight deviation, one possible explanation for the size difference might be the broadening due to the extended tip.

The second type of BINA frequently observed on TiO_2 anatase (101) is the three-lobe structure. Figure 4.22a shows this coordination type adsorbed at a step edge with atomically resolved substrate. The submolecular resolution reveals six protrusions. Figure 4.22b shows a dimeric BINA three-lobe assembly. The currently performed DFT modeling of the three-lobe shape and of additionally observed BINA structures will reveal further details of specific coordination modes.

In previous theoretical studies, the adsorbed molecules have been generally considered as isolated, even though high coverages or full monolayers of adsorbed molecules are often present in experiments and are relevant for applications. Hence, the experimental determination of supramolecular interactions between BINA molecules is important. The STM image shown in Figure 4.23a reveals the formation of molecular assemblies, i.e. dimeric and trimeric u-shape BINA clusters. Strikingly, the BINA molecules assemble into single molecular chains which are orientated again in a preferential angle of ∼ -45° relative to the [010] substrate direction. Figure 4.23b shows a 3D view of a BINA u-shape dimer at atomic substrate resolution. The mobility of the BINA molecules on the TiO_2 anatase (101) surface is also revealed in Figure 4.23c and 4.23d where the binding of both single and dimeric BINA molecules to step edges are resolved. These findings show that supramolecular mutual interactions have a direct influence on the adsorption

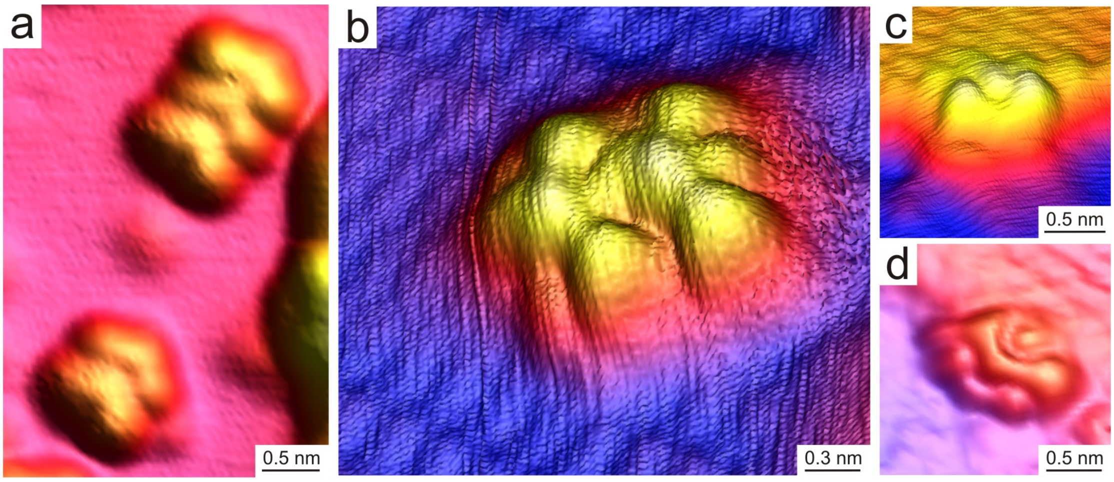

Figure 4.23: High-resolution STM images of the BINA ligand adsorbed on TiO_2 anatase (101). (a) Formation of supramolecular BINA assemblies preferentially orientated along the [010] substrate direction (1.7 V, 0.08 nA, 5 K). (b) Perpective view of a BINA dimer with atomic substrate resolution. (c) Single BINA molecule binding at a substrate step edge (1.9 V, 0.07 nA, 5 K) (d) Formation of a BINA dimer at the step edge (1.8 V, 0.06 nA, 5 K).

sites on TiO_2 anatase (101).

The observation of various different BINA adsorption geometries on TiO_2 anatase (101) represents an unexpected finding since not only the thermodynamically most stable adsorption configuration of the BINA was observed. These results suggest that the observation of various different N3 adsorption geometries reported in Section 4.3 can be attributed to a complex combination of the multiple BINA coordination modes. One further important finding is the BINA ligand mobility which correlates to the observed N3 dye diffusion on TiO_2 anatase (101).

4.5 Photosensitizer N3 on Au(111)

Elucidating details of the geometrical and electronic properties of the photosensitizer N3 on Au(111) surfaces potentially helps to understand fundamentals of a new type of dye-sensitized solar cell proposed by McFarland and Tang.[246] In these cells, a fluorescein photoreceptor is adsorbed on an Au/TiO_2/Ti multilayer structure. The photoexcited electrons are transferred from the dye through the conducting surface layer and over the Schottky barrier to the titanium providing a photocurrent. These devices show high internal quantum efficiencies and the advantage of operating without an electrolyte. Furthermore, comparing STM/STS findings of the N3 dye on Au(111) to respective structural and electronic properties on TiO_2 anatase (101) gives insights into the general N3 adsorption characteristics on both metal and metal oxide surfaces.

In this section, we study the geometric and electronic properties of the N3 dye adsorbed on Au(111) by means of scanning tunneling microscopy and spectroscopy at 5 K. The Au(111) surface was prepared following the sample cleaning procedure

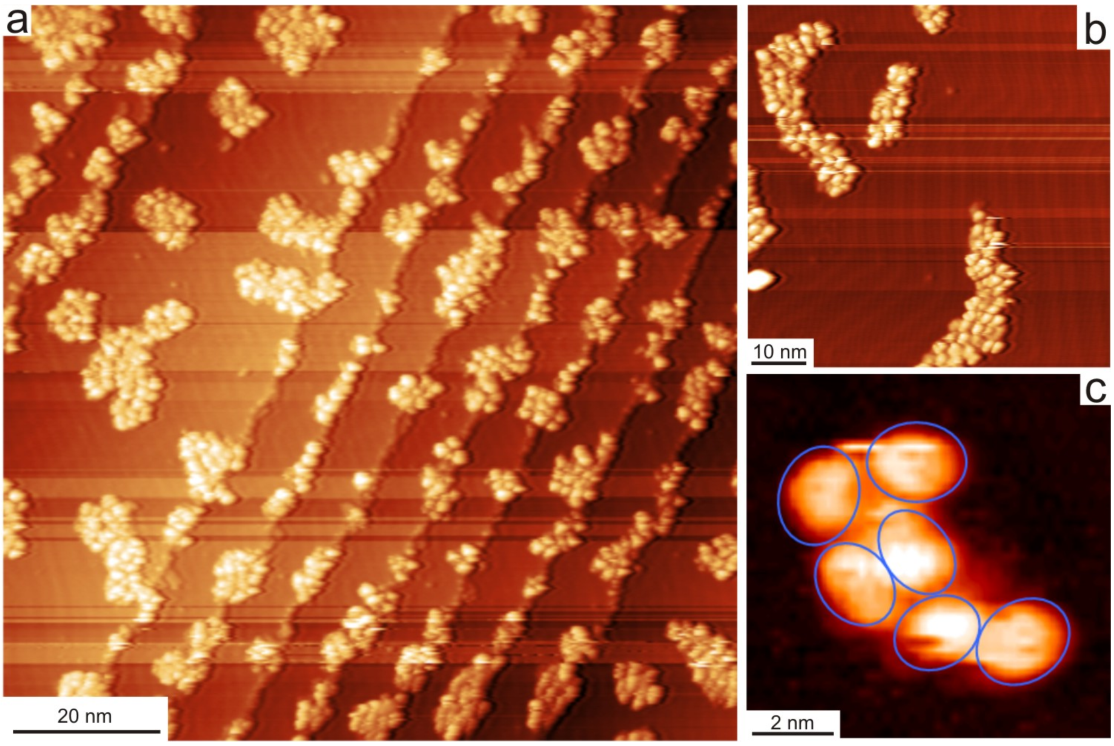

Figure 4.24: Constant current STM images of the photosensitizer N3 adsorbed at low coverage on Au(111). (a) Overview image revealing the formation of N3 assemblies (2 V, 0.3 nA, 5 K). (b) N3 clustering along the Au(111) herringbone reconstruction (2 V, 0.3 nA, 5 K). (c) Enlarged view of a N3 cluster (1.8 V, 0.2 nA, 297 K).

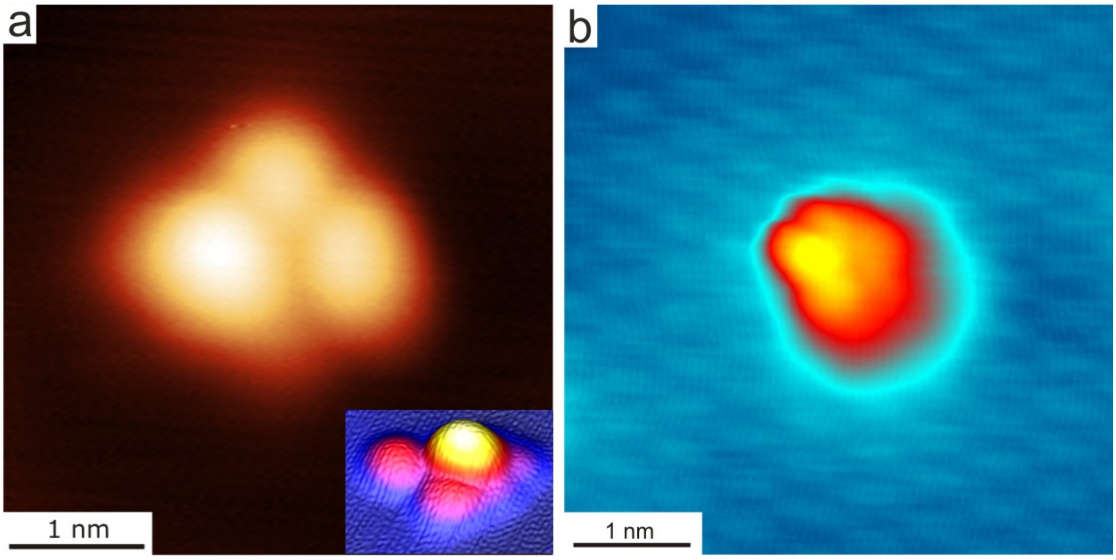

Figure 4.25: High-resolution STM images of the N3 dye adsorbed on (a) Au(111) (inset: rotated 3D-view) (1.48 V, 0.1 nA, 5 K) and (b) TiO_2 anatase (101) 2.0 V, 0.2 nA, 5 K.

described in Section 1.2. Electrospray ion beam depostion was employed to bring singly ionized N3 molecules onto the Au(111) surface (details see Section 1.3 and 4.3.1) Upon N3 deposition, the sample was cooled to 5 K for characterization.

Figure 4.24a shows a STM overview image of N3 dyes adsorbed at low coverage (charge of 15 pAh) on Au(111). It reveals the assembly of N3 molecules into larger two-dimensional clusters and chains on both terraces and, to a greater extent, at substrate step edges. The supramolecular N3 clusters preferentially assemble along the Au(111) herringbone reconstruction as shown in Figure 4.24b. This corresponds to previous findings that N3 dyes adsorb primarily at the faulted regions of the Au(111) herringbone reconstruction.[247] Figure 4.24c shows a N3 cluster in more detail. Comparing the lateral size of N3 dyes of $\sim$ 15 Å measured on TiO_2 anatase (101) (see Section 4.3) to the dimensions of each protrusion revealed in the STM image allows the conclusion that each protrusion in Figure 4.24c corresponds to a single N3 molecule. The observation of N3 assemblies hints to N3 molecules which are free to diffuse upon adsorption on the Au(111) surface. Their mobility seems not to be hindered by interaction with the substrate and only gets reduced upon the formation of molecular assemblies preferentially at the elbow site of the herringbone reconstruction or upon binding at step edges. The preferential N3 binding at the Au(111) elbow sites of the herringbone reconstruction could be attributed to the higher electron density at these sites.

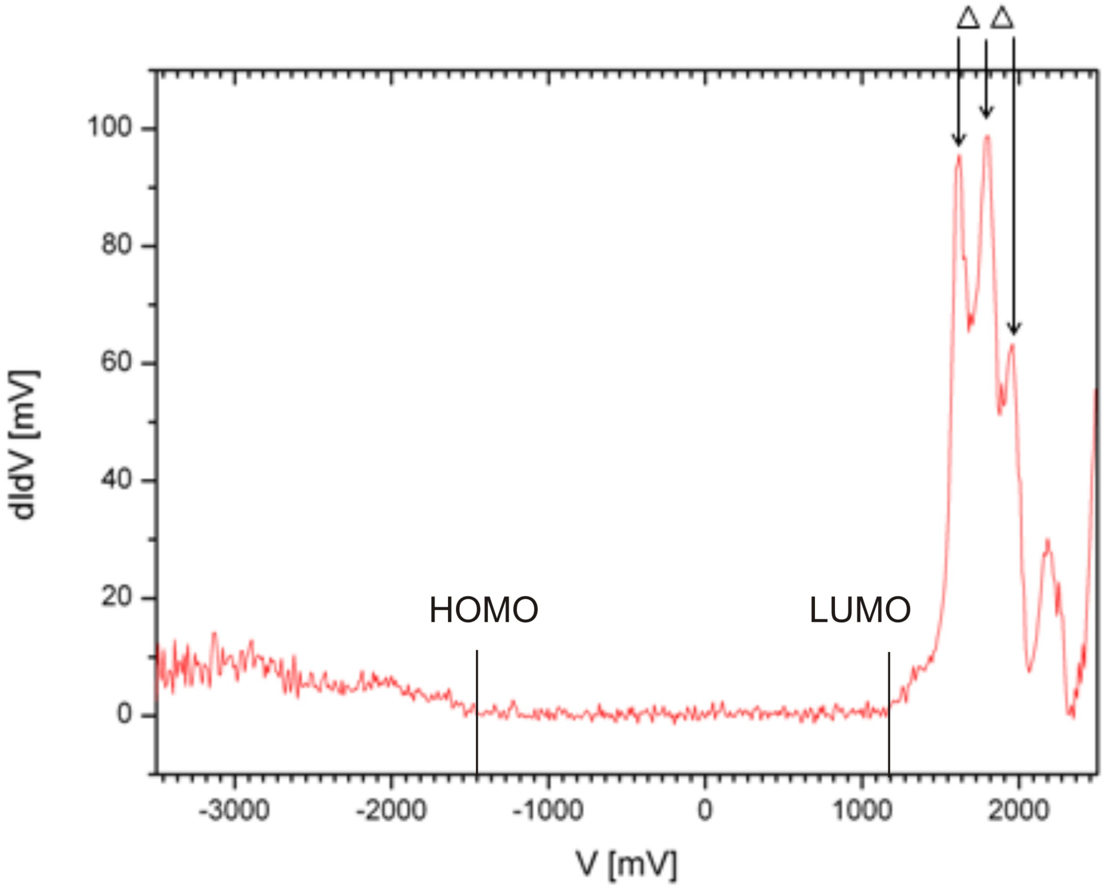

Figure 4.26: Differential conductance spectrum recorded above the center of the N3 dye adsorbed on Au(111) at 5 K. N3 HOMO and LUMO starts rising at - 1.5 V and + 1.2 V, respectively. Vibronic modes are revealed with equidistant features (Δ E ∼ 200 mV).

A high-resolution STM image of a single N3 molecule adsorbed on Au(111) is shown in Figure 4.25a. The N3 dye is characterized by a triangular adsorption shape with ∼ 15 Å lateral size. The submolecular resolved STM image indicates three circular protrusions within a single N3 dye. The molecular adsorption shape of the N3 molecules show similar dimensions on both Au(111) and TiO_2 anatase (101) as compared in Figure 4.25.

Figure 4.26 shows a differential conductance spectrum of the N3 dye taken at 5 K. The spectrum exhibits rising of the N3 HOMO and LUMO at - 1.5 V and + 1.2 V, respectively. Furthermore, the spectrum displays a series of equally spaced features with equidistant peaks separated by ∼ 200 mV. These features are attributed to resonant tunneling into vibronic states of individual N3 molecules.[248] Polypyridyl ruthenium complexes were studied for instance by resonance Raman spectroscopy.[249] The equidistant features ($\Delta E \sim 200$ mV) are indicative of C-H bending and C-C stretching modes of the bipyridine rings. XPS studies suggested that the N3 dye bonds to the Au(111) surface via the sulphur atoms of its thiocyanate ligands, most likely accompanied by a physisorption interaction from the bi-isonicotinic acid ligands.[247,250] The observation of vibronic modes in the STS spectrum supports such possible N3 adsorption configuration on Au(111) where the bipyridine rings are lifted up from the surface. In this case, the N3 molecules are chemisorped with either one or two NCS groups on the gold substrate.

In conclusion, the coordination of the N3 molecules via its thiocyanate ligands to the gold substrate shows remarkable different adsorption behaviour on TiO_2 anatase (101) where the carboxylate groups of the N3 anchoring ligand BINA dominate the substrate binding.

Conclusions and Perspectives

The current thesis aimed at providing an experimental basis for gradually approaching the longterm aim of increasing the efficiency of current solar converters such as dye-sensitized solar cells as well as the realization of surface assisted catalysis for chemical energy conversion. To this end, both the hierarchical assembly of metal-organic coordination networks for functional catalysis and the molecule-oxide interface of dye-sensitized solar cells have been investigated. The key scientific results of this thesis can be condensed as follows:

1. Realization of a new low-temperature scanning tunneling microscope
2. Hierarchical assembly of highly adaptive metal-organic coordination networks and its catalytic functionalization
3. Structural and electronic characterization of the photosensitizer N3 - TiO_2 anatase (101) interface at the atomic level.

The investigation of metal oxide surfaces necessitated the first integral part of this thesis: the design and construction of a new type of low-temperature STM operating in UHV. The realization of the STM unit, its wiring to a new liquid helium bath cryostat as well as the construction of various different system components such as a manipulator unit, an optical microscope or an UHV transfer suitcase unit was described in Chapter 2. In this STM design, the z-approach is realized by using an Attocube piezo system which allows precise tip z-approach. Lateral sample positioning with (sub-)micrometer precision in a range of 5×5 mm^2 is made possible by x-y shear actuators. An optical access to the tip-sample junction allows to control the sample positioning by a CCD camera and furthermore enables light-induced or photo-emission studies. In addition, the new STM design features simple in-situ tip exchange and the possibility of using a variety of sampleholders for different substrates. Four independent contacts to the sample can be used for in-situ transport and back-gate functionalities. The STM setup provides a basis for a variety of novel experiments on different substrates (see below).

Based on this STM, the first main research direction constituted the fabrication and characterization of extended metal-organic coordination networks on metal surfaces with insensitivity to intrinsic substrate defects and its functionalization by catalytic active metal atoms. The formation of extended two-dimensional MOCNs showing high adaptability to surface step edges and structural defects was revealed by scanning tunneling microscopy. Chapter 3 reported on the rod-like 4,4'-di-(1,4-buta-1,3-diynyl)-benzoic acid BDBA and iron atoms which assemble into extended 2D-MOCNs on Au(111) and Ag(100) surfaces. Independent from the chosen substrate and its surface symmetry the MOCN grows continuously over multiple surface terraces through mutual inphase structure adaptation of network domains at step edges as well as on terraces. The adaptability of the MOCNs was mainly ascribed to the high degree of conformational flexibility of the butadiynyl functionality of the ligand. Despite their flexibility, the MOCNs exhibit considerable robustness against annealing at high temperatures. The findings show that mesoscale self-assembled functional architectures with a high degree of substrate error tolerance can be realized with metal coordination networks.

Further, the interaction of nickel atoms and clusters with the butadiyne metal-organic templates on Au(111) and Ag(100) surfaces was investigated by STM. It was shown that Ni atoms can be incorporated in the metal-organic matrix without loosing its structural integrity. It turned out that the metal substrate plays a crucial role in the interaction of Ni atoms with the metal-organic host networks. On Au(111), Ni clusters and islands are spatially limited to the network cavity size and decorate the phenyl rings. In contrast, on Ag(100) the metal-organic template imposes the nucleation of Ni atoms within the topmost substrate layer underneath the network pattern. In both cases, clusters consisting of a few metal atoms with an areal density of 4×10^{13} cm^{-2} can be obtained that are stable upon annealing up to 450 K, i.e. relevant temperatures in catalytic reactions. Additionally, experimental evidence was given that the Ni decorated networks can be utilized for binding additional molecular units into the network cavities which opens up the way to assemble hierarchically organized multicomponent architectures at surfaces.

The second main research topic of this thesis focused on the atomic-scale investigation of the structural and electronic properties of the photosensitizer N3 and its anchoring ligand BINA adsorbed on TiO_2 anatase (101). First, the preparation of atomically well-defined TiO_2 anatase surfaces using natural TiO_2 bulk crystals was reported. Subsequently, Chapter 4 reported on a combined experimental and theoretical study of the geometric and electronic properties of the photosensitizer N3 adsorbed on TiO_2 anatase (101). In situ electrospray ionization deposition combined with STM and STS studies in UHV at 5 K provided direct access to the dye-substrate interface at the atomic level. The local structure of N3 molecules was probed with single molecule sensitivity revealing multi-conformational N3 binding geometries on the oxide support. Experimental evidence was given that the electronic properties of the photosensitizer N3 strongly depend on its adsorption geometry which makes specific dye adsorption geometries more favorable in terms of higher charge injection efficiencies. Furthermore, the STM studies revealed the formation of supramolecular N3 dye assemblies that are potentially stabilized by molecular interactions. To gain further insights into the N3 coordination geometry, the N3 studies were complemented with STM investigations of the N3 anchoring ligand BINA adsorbed on TiO_2 anatase (101). The multi-conformational N3 binding geometries were correlated to the observation of multiple adsorption configurations of the BINA ligand on the TiO_2 support. These experimental findings were supported by density functional theory based calculations. Additionally, the N3 dye was resolved with submolecular resolution on Au(111). The observation of vibronic modes in the N3 STS spectrum supports previously suggested N3 adsorption configuration on Au(111) where the bipyridine rings are lifted up from the surface with the N3 molecules chemisorped with either one or two NCS groups on the gold substrate.

These findings contribute to a major leap when striving for higher efficient DSSCs with the longterm aim to make these devices a primary contributor to renewable electricity generation. Further optimization of DSSC efficiencies greatly benefits from the possibility of correlating the photosensitizer adsorption geometries to electronic properties at the dye-substrate interface. The insight that only specific dye adsorption configurations participate in the charge injection process is of direct relevance to the optimization of the quantum yield of DSSCs. By proceeding current investigations, chemists can be provided in the future with specific design rules enabling the synthesis of optimized photosensitizer structures for maximum charge injection efficiencies and low charge recombination rates. The experimental procedure developed in this thesis can be directly extended to new dye molecules and a variety of different substrates. Even in the early stages of development, photosensitizers can be probed with molecular sensitivity on relevant photoelectrodes which allows preselection of highly suitable chemical structures. Furthermore, the atomic-scale insights pave the route towards achieving optimum dye coverages and enhanced structural stability of the dye-substrate interface. Finally, the present work provides an experimental basis for important complementary investigations in the future.

Defects, dye co-sensitization and photodynamics at molecule-oxide interfaces

The new STM developed in the framework of the thesis allows further investigations which are highly relevant for increasing the efficiency of DSSCs. One important aspect to be studied in detail constitutes the spectroscopic characterization of local defects on TiO_2 surfaces at low temperature. Furthermore, the experimental setup allows investigations of light-induced processes at the atomic level of the dye-substrate interface in situ during the STM measurements. Among various potential projects, one particular interesting study represents the investigation of co-sensitization processes, i.e. systems in which different dye molecules are combined to extend the photoabsorption spectrum toward longer wavelengths. In this context, little is known about the so-called concerto effect: the absorption, i.e. bandwith as well as cross section, of a dye mixture is larger and enhanced with respect to the single components. The composition and adlayer structure alone would be of great interest to understand this effect.

The following experiment can be envisioned as schematically illustrated in Figure 4.27. Light coupled into the tip-surface junction is absorbed by the molecules

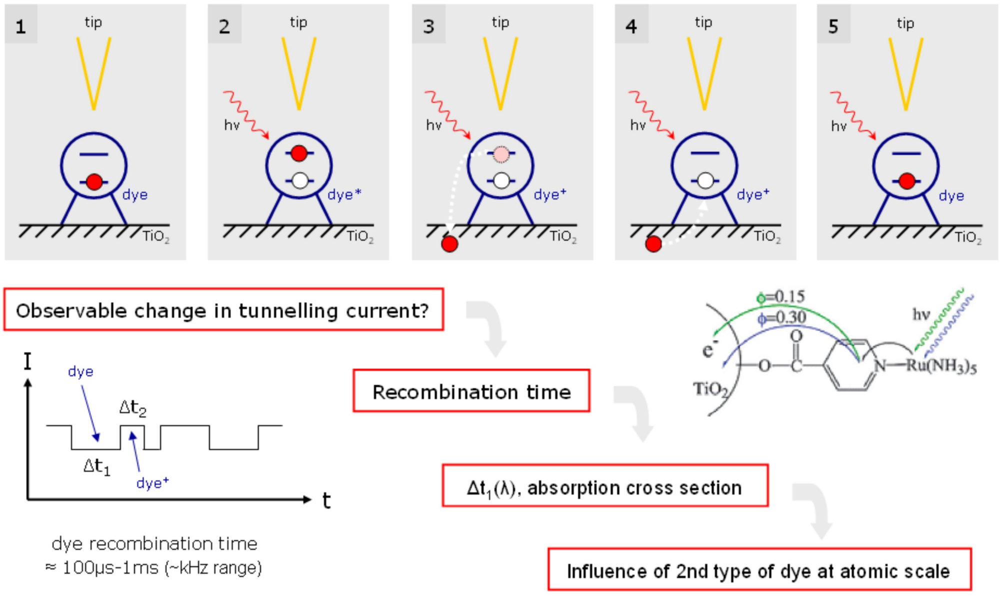

Figure 4.27: Schematic drawing: studying the photodynamics of single photosensitizers as well as compositions of different dyes on TiO_2 surfaces. Light coupled into the tip-surface junction induces charge injection into the metal oxide support. Measuring the inherent changes in the tunneling current allows estimations of absorption probabilities well as the recombination rate aiming at providing an atomistic picture of for instance the concerto effect (see text).

(2). The excited state generally has a short lifetime (fs) and donates charge into the substrate (3). The dye is left in a positively charged state with a hole in the HOMO which should influence the conductance of the tunneling junction because of a change in the potential conductivity and in the work function due to positive charge on the molecule. After a certain time (μs - ms) the dye recombines with electrons from the substrate to a neutral state due to the absence of the electrolyte (4) and a new cycle can begin. The photon absorption process should be slower than the recombination rate at the employable light intensities ($\sim$ seconds at mW laser intensities focused to the tip). Hence, the current should be in a low and high state, corresponding to be charged and neutral molecule one way or another. From the frequency of up and down jumps of the current one can estimate the absorption probabilities as well as the recombination rate. The latter should be independent of the wavelength of the light and is an important parameter in the overall efficiency of DSSCs. Then the wavelength of the light can be tuned using a tunable white laser and one would obtain a histogramm of current jumps in dependence of the light wavelength and hence a measure of the absorption probability of a single dye for each wavelength. This can be then studied in dependence of local fields and dipoles (from steps, defects) and other dye molecules and adsorbates to get an atomistic picture on the concerto effect.

Magnetic impurities on gate-tunable substrates

The ability to implement chip carriers and to access optically controlled small sample areas with the new STM setup allows the investigation of gate-tunable substrates such as graphene on SiO_2 or $SrTiO_3$ as shown in Figure 4.28. Most of the recent studies on organic-based nanostructures on surfaces have focused on metallic surfaces. It is widely known that the metallic substrate specifically modifies the electronic and chemical properties of the adsorbates.[251] However, the usage of substrates such as graphene gives rise to the possibility of adjusting the substrate charge carrier density and thus, to modify self-organization processes on such substrates. Furthermore, the study of systems consisting of magnetic impurities in/on graphene and their property dependence on the substrate are currently of high interest. Over the last ten years, for instance the Kondo effect[252] has been observed in the transport properties of many nanoscale systems such as quantum dots,[253] single atoms,[254] carbon nanotubes[255] and single molecules.[256] Due to the powerful ability in high resolution observation and manipulation in real space, the STM has been employed for both observing and controlling the Kondo effect of magnetic impurities on surfaces at a single-molecule level. There have been several efforts to study the Kondo effect of a single adsorbed magnetic impurity

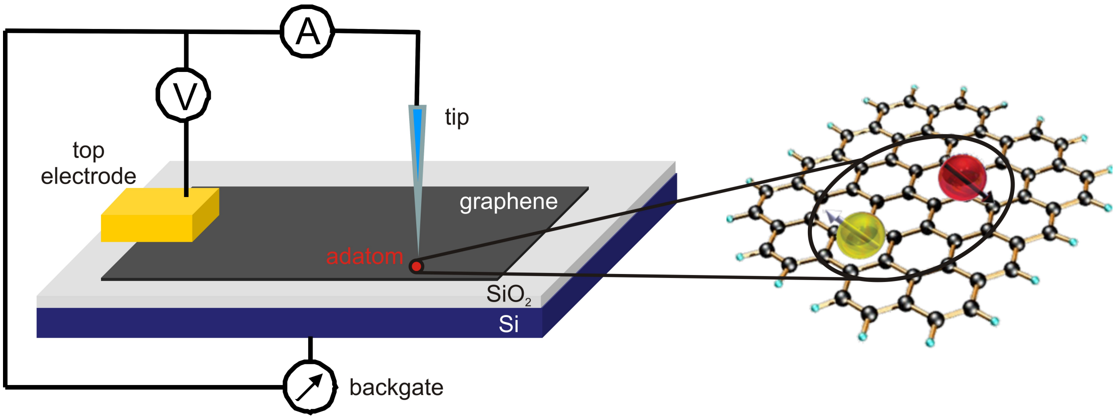

Figure 4.28: Schematic drawing: studying the Kondo effect and RKKY interaction of magnetic impurities adsorbed on a graphene monolayer on Si wafers. The system can be tuned into the Kondo regime and the RKKY interaction between adatoms modulated from ferromagnetic to antiferromagnetic coupling by applying a backgate voltage.

controlled indirectly by modulations of surface density of states,[257] by surface coordination numbers[257] and by controllable ligation.[258] However, manipulating the Kondo effect of a single magnetic impurity by directly tuning its interaction with the metal host remains challenging. Furthermore, the indirect exchange interaction between magnetic impurities localized in a graphene plane and its influence on the Kondo effect is currently of high interest.[258,259] One promising future research direction constitutes the study of magnetic impurities on gate-tunable substrates. Theoretical works predict the observability of an unconventional Kondo effect[260,261] and a finite critical Kondo coupling strength in/on graphene. Accordingly, the Kondo regime can be entered by tuning the applied sample gate voltage und thus varying the graphene charge carrier density.[260] However, at present, experiments in this field are scarce.[262] Furthermore, the focus could be on the investigation of the Ruderman-Kittel-Kasuya-Yosida (RKKY) interaction[263] between magnetic impurities in/on graphene. According to existing theories, the properties of magnetic impurities and their mutual interaction could be manipulated between the ferromagnetic and antiferromagnetic regime by tuning the substrate charge carrier density.[259,264] A potential experimental approach could comprise: (i) realization of samples consisting of e.g. a graphene monolayer on Si wafers and adsorbing cobalt phthalocyanine molecules as spin 1/2 system with an out of plane orbital on the graphene monolayer (ii) appropriate electrical contacting of the samples and integration into the new sample holders which were specifically developed for this purpose (iii) study properties mainly with respect to the tunable substrate charge carrier density and verify theoretical predictions. Furthermore, the mutual RKKY interaction between magnetic impurities on graphene, their dependence on the graphene electron density and their influence on the Kondo effect are highly interesting topics.

Surface assisted catalysis for chemical energy conversion

The realization of extended and robust metal-organic coordination networks as well as their functionalization with catalytic active nickel atoms opens new research avenues in the field of surface assisted catalysis. The stability and direct accessibility of the non-capped Ni atoms and clusters on both gold and silver substrates render these systems attractive candidates to explore their catalytic activity. The low-valent Ni atoms are potential active sites for CO_2 conversion[128] and consequently, a highly promising experiment would be the study of the binding behaviour of CO_2 and CO to these MOCNs.

Bibliography

[1] Binnig, G. & Rohrer, H. *Helvetica Physica Acta* **55**, 726–735 (1982).

[2] Binnig, G. & Rohrer, H. *IBM Journal of Research and Development* **30**, 355 (1986).

[3] Ho, W. *J. Chem. Phys.* **117**, 11033 (2002).

[4] Zandvliet, H. J. W. & van Houselt, A. *Annu. Rev. Anal. Chem.* **2**, 37 (2009).

[5] Pan, S. H., Hudson, E. W., Lang, K. M., Eisaki, H., Uchida, S. & Davis, J. C. *Nature* **403**, 746 (2000).

[6] Crommie, M. F., Lutz, C. P. & Eigler, D. M. *Nature* **363**, 524 (1993).

[7] Oncel, N., van Houselt, A., Huijben, J., Hallbäck, A. . S., Gurlu, O., Zandvliet, H. J. W. & Poelsema, B. *Phys. Rev. Lett.* **95**, 116801 (2005).

[8] Carpinelli, J. M., Weitering, H. H., Plummer, E. W. & Stumpf, R. *Nature* **381**, 398 (1996).

[9] Weitering, H. H., Carpinelli, J. M., Melechko, A. V., Zhang, J., Bartkowiak, M. & Plummer, E. W. *Science* **285**, 2107 (1999).

[10] Jung, T. A., Schlitter, R. R. & Gimzewski, J. K. *Nature* **386**, 696 (1997).

[11] Dmitriev, A., Spillmann, H., Lin, N., Barth, J. V. & Kern, K. *Angew. Chem. Int. Ed.* **42**, 2670 (2003).

[12] Yokoyama, T., Yokoyama, S., Kamikado, T., Okuno, Y. & Mashiko, S. *Nature* **413**, 619 (2001).

[13] Rosei, F. *et al. Science* **296**, 328 (2002).

[14] Theobald, J. A., Oxtoby, N. S., Phillips, M. A., Champness, N. R. & Beton, P. H. *Nature* **424**, 1029 (2003).

[15] Spillmann, H., Dmitriev, A., Lin, N., Messina, P., Barth, J. V. & Kern, K. *J. Am. Chem. Soc.* **125**, 10725 (2003).

[16] Lopinski, G. P., Moffatt, D. J., Wagner, D. D. & Wolkow, R. A. *Nature* **392**, 909 (1998).

[17] Barth, J. V. *et al.* *J. Am. Chem. Soc* **124**, 7991 (2002).

[18] Pietzsch, O., Kubetzka, A., Bode, M. & Wiesendanger, R. *Science* **292**, 2053 (2001).

[19] Heinze, S., Bode, M., Kubetzka, A., Pietzsch, O., Nie, X., Blügel, S. & Wiesendanger, R. *Science* **288**, 1805 (2000).

[20] Zambelli, T., Barth, J. V., Wintterlin, J. & Ertl, G. *Nature* **390**, 495 (1997).

[21] Dürr, M., Biedermann, A., Hu, Z., Höfer, U. & Heinz, T. F. *Science* **296**, 1838 (2002).

[22] Guo, X. . C. & Madix, R. J. *J. Phys. Chem. B* **107**, 3105 (2003).

[23] Besenbacher, F., Chorkendorff, I., Clausen, B. S., Hammer, B., Molenbroek, A. M. & Norskov, I., Stensgaard. *Science* **279**, 1913 (1998).

[24] Nazeeruddin, M. K. *et al.* *J. Am. Chem. Soc.* **115**, 6382 (1993).

[25] Lehn, J.-M. *Supramolecular Chemistry: Concepts and Perspectives.* (Wiley-VCH., Weinheim, 1995).

[26] Wiester, M. J., Ulmann, P. A. & Mirkin, C. A. *Angew. Chem., Int. Ed.* **50**, 114 (2011).

[27] Lin, N., Stepanow, S., Ruben, M. & Barth, J. V. *Top. Curr. Chem.* **287**, 1 (2009).

[28] Barth, J. V., Costantini, G. & Kern, K. *Nature* **437**, 671 (2005).

[29] Schnadt, J., Rauls, E., Xu, W., Vang, R. T., Knudsen, J., Læ gsgaard, E. & Besenbacher, F. *Phys. Rev. Lett.* **100**, 46103 (2008).

[30] Langner, A., Tait, S. L., Lin, N., Chandrasekar, R., Ruben, M. & Kern, K.

Angew. Chem. Int. Ed. **48**, 8835 (2008).

[31] O'Keeffe, M. & Yaghi, O. M. *Chem. Rev.* **112**, 675 (2012).

[32] Meek, S. T., Greathouse, J. A. & Allendorf, M. D. *Adv. Mater.* **23**, 249 (2011).

[33] Stepanow, S., Lin, N., Barth, J. V. & Kern, K. *J. Phys. Chem. B* **110**, 23472 (2006).

[34] Clair, S., Pons, S., Fabris, S., Baroni, S., Brune, H., Kern, K. & Barth, J. V. *J. Phys. Chem. B* **110**, 5627 (2006).

[35] Lu, Y., Yeung, N., Sieracki, N. & Marshall, N. M. *Nature* **460**, 855 (2009).

[36] Merkx, M., Kopp, A., Sazinsky, M. H., Blazyk, J. L., Müller, J. & Lippard, S. J. *Angew. Chem. Int. Ed.* **40**, 2782 (2001).

[37] Fabris, S. *et al.* *Nano Lett.* **11**, 5414 (2011).

[38] Langner, A., Tait, S. L., Lin, N., Chandrasekar, R., Ruben, M. & Kern, K. *Proc. Nat. Acad. Sci. USA* **104**, 17927 (2007).

[39] Langner, A. *et al.* *Angew. Chem. Int. Ed.* **51**, 4327 (2012).

[40] $http://www.nrel.gov/ncpv/images/efficiency\_chart.jpg$.

[41] Kamat, P. V. *J. Phys. Chem. C* **116**, 11849 (2012).

[42] Weir, A., Westerhoff, P., Fabricius, L., Hristovski, K. & von Goetz, N. *Environ. Sci. Technol.* **46**, 2242 (2012).

[43] Diebold, U. *Surf. Sci. Rep.* **48**, 53 (2003).

[44] Fujishima, A. & Honda, K. *Nature* **237**, 37 (1972).

[45] Molinari, A., Amadelli, R., Antolini, L., Battioni, P. & Mansuy, D. *J. Mol. Catal. A: Chem* **158**, 521 (2000).

[46] Makarova, O. V., Rajh, T., Thurnauer, M., Martin, A., Kemme, P. A. & Cropek, D. *Environ. Sci. Technol.* **34**, 4797 (2000).

[47] Wold, A. *Chem. Mater.* **5**, 280 (1993).

[48] Hadjiivanov, K. & Klissurski, D. *Chem. Soc. Rev.* **25**, 3123 (1996).

[49] Simons, C. *Chem.-Eur. J.* **10**, 5829 (2004).

[50] Maeda, K. & Domen, K. *Phys. Chem. Lett.* **1**, 2655 (2010).

[51] Teoh, W. Y., Scott, J. A. & Amal, R. *J. Phys. Chem. Lett.* **3**, 629 (2012).

[52] Moseley, P. T. & Tofield, B. C. (eds.) *Solid State Gas Sensing* (Adam Hilger, Bristol, 1987).

[53] Varghese, O. K. & Grimes, C. A. *J. Nanosci. Nanotech.* **3**, 277 (2003).

[54] Borgarello, E., Kiwi, J., Pelizzetti, E., Visca, M. & Grätzel, M. *J. Am. Chem. Soc.* **103**, 6324 (1981).

[55] Gao, Y. M., Shen, H. S., Dwight, K. & Wold, A. *Mater. Res. Bull.* **27**, 1023 (1992).

[56] Jones, F. H. *Surf. Sci. Rep.* **42**, 75 (2001).

[57] Xiong, H., Slater, M. D., Balasubramanian, M., Johnson, C. S. & Rajh, T. *J. Phys. Chem. Lett.* **2**, 2560 (2011).

[58] Borgarello, E., Kiwi, J., Grätzel, M., Pelizzetti, E. & Visca, M. *J. Am. Chem. Soc.* **104**, 2996 (1982).

[59] Serpone, N. & Pelizzetti, E. (eds.) *Photocatalysis Fundamentals and Applications* (Wiley, New York, 1989).

[60] Linsebigler, A. L., Lu, G. Q. & Yates, J. T. *Chem. Rev.* **95**, 735 (1995).

[61] O'Regan, B. & Grätzel, M. *Nature* **353**, 737 (1991).

[62] Hagfeldt, A. & Grätzel, M. *Chem. Rev.* **95**, 49 (1995).

[63] Kavan, L., Grätzel, M., Gilbert, S. E., Klemenz, C. & Scheel, H. J. *J. Am. Chem. Soc.* **118**, 6716 (1996).

[64] Barbé, C. J., Arendse, F., Comte, P., Jirousek, M., Lenzmann, F., Shklover, V. & Grätzel, M. *J. Am. Ceram. Soc.* **80**, 3157 (1997).

[65] Peter, L. M. *J. Phys. Chem. Lett.* **2**, 1861 (2011).

[66] Hardin, B. E., Snaith, H. J. & McGehee, M. D. *Nat. Phot.* **6**, 162 (2012).

[67] Mora-Sero, I. & Bisquert, J. *J. Phys. Chem. Lett.* **1**, 3046 (2010).

[68] Tersoff, J. & Hamann, D. R. *Phys. Rev. Lett.* **50**, 1998 (1983).

[69] Tersoff, J. & Hamann, D. R. *Phys. Rev. B* **31(2)**, 805 (1985).

[70] Bardeen, J. *Phys. Rev. Lett.* **6(2)**, 57 (1961).

[71] Miller, S. A., Luo, H., Pachuta, S. J. & Cooks, R. G. *Science* **275**, 1447 (1997).

[72] Ouyang, Z. *et al. Science* **301**, 1351 (2003).

[73] Gologan, B., Green, J. R., Alvarez, J., Laskin, J. & Cooks, R. G. *Phys. Chem. Chem. Phys.* **7**, 1490 (2005).

[74] Rauschenbach, S., Stadler, F. L., Lunedei, E., Malinowski, N., Koltsov, S., Constantini, G. & Kern, K. *Small* **2**, 540 (2006).

[75] Rauschenbach, S. *et al. ACS Nano* **3**, 2901 (2009).

[76] Fenn, J. B., Mann, M., Meng, C. K., Wong, S. F. & Whitehouse, C. M. *Science* **246**, 64 (1989).

[77] Pohl, D. W. *Rev. Sci. Instrum. 58* **58**, 54 (1987).

[78] Barth, J. V., Brune, H., Ertl, G. & Behm, R. J. *Phys. Rev. B* **42**, 15 (1990).

[79] Chen, W., Madhavan, V., Jamneala, T. & Crommie, M. *Phys. Rev. Lett.* **80**, 1469 (1998).

[80] Reinert, F. & Nicolay, G. *Appl. Phys. A: Mat. Science and Processing* **78**, 817 (2004).

[81] Cicoira, F., Santato, C. & Rosei, F. *Top. Curr. Chem.* **285**, 203 (2008).

[82] Bartels, L. *Nat. Chem.* **2**, 87 (2010).

[83] Seufert, K., Bocquet, M. . L., Auwärter, W., Weber-Bargioni, A., Reichert, J., Lorente, N. & Barth, J. V. *Nat. Chem.* **3**, 114 (2011).

[84] Carbone, C. & et al. *Adv. Funct. Mater.* **21**, 1212 (2011).

[85] Urdampilleta, M., Klyatskaya, S., Cleuziou, J. . P., Ruben, M. & Wernsdorfer, W. *Nat. Mater.* **10**, 502 (2011).

[86] Langner, A., Tait, S. L., Lin, N., Rajadurai, C., Ruben, M. & Kern, K. *Proc. Natl. Acad. Sci. U.S.A.* **46**, 17927 (2007).

[87] Stepanow, S. *et al.* *Nat. Mater.* **3**, 229 (2004).

[88] Kühne, D., Klappenberger, F., Krenner, W., Klyatskaya, S., Ruben, M. & Barth, J. V. *Proc. Natl. Acad. Soc. U.S.A.* **107**, 21332 (2010).

[89] Gambardella, P. & et al. *Nat. Mater.* **8**, 189 (2009).

[90] Kühne, D. *et al.* *J. Am. Chem. Soc.* **131**, 3881 (2009).

[91] Méndez, J., Lo.pez, M. F. & Martin-Gago, J. *A. Chem. Soc. Rev.* **40**, 4578 (2011).

[92] Bieri, M. *et al.* *J. Am. Chem. Soc.* **132**, 16669 (2010).

[93] Abel, M., Clair, S., Ourdjini, O., Mossoyan, M. & Porte, L. *J. Am. Chem. Soc.* **133**, 1203 (2011).

[94] Bieri, M. & et al. *Chem. Commun.* **45**, 6919 (2009).

[95] Perepichka, D. F. & Rosei, F. *Science* **323**, 216 (2009).

[96] Zwaneveld, N. A. A., Pawlak, R., Abel, M., Catalin, D., Gigmes, D., Bertin, D. & Porte, L. *J. Am. Chem. Soc.* **130**, 6678 (2008).

[97] Heim, D. *et al.* *J. Am. Chem. Soc.* **132**, 6783 (2010).

[98] Schnadt, J., Xu, W., Vang, R. T., Knudsen, J., Zheshen, L., Lagsgaard, E. & Besenbacher, F. *Nano Res.* **3**, 459 (2010).

[99] Matsubara, H., Shimura, T., Hasegawa, A., Semba, M., Asano, K. & Asamoto, K. *Chem. Lett.* 1099 (1998).

[100] Fasina, T. M. *et al.* *J. Mater. Chem.* **15**, 690 (2005).

[101] Nie, G., X.; Wang. *J. Org. Chem.* **71**, 4734 (2006).

[102] Clair, S., Pons, S., Seitsonen, A. P., Brune, H., Kern, K. & Barth, J. V. *J. Phys. Chem. B* **108**, 14585 (2004).

[103] Schlickum, U. *et al.* *J. Phys. Chem. B* **114**, 15602 (2010).

[104] Payer, D. *et al.* *Chem. Eur. J.* **13**, 3900 (2007).

[105] Dmitriev, A., Spillmann, H., Lin, N., Barth, J. V. & Kern, K. *Angew. Chem. Int. Ed.* **42**, 2670 (2003).

[106] Lingenfelder, M. A., Spillmann, H., Dmitriev, A., Stepanow, S., Lin, N., Barth, J. V. & Kern, K. *Chem.-Eur. J.* **10**, 1913 (2004).

[107] Zhang, Y. . F., Zhu, N. & Komeda, T. *J. Phys. Chem. C* **111**, 16946 (2007).

[108] Lin, N., Stepanow, S., Vidal, F. & Barth, J. V. *Chem. Commun.* **13**, 1681 (2005).

[109] Stuve, E. M., Madix, R. J. & Sexton, B. A. *Surf. Sci.* **123**, 491 (1982).

[110] Pascual, J. I., Barth, J. V., Ceballos, G., Trimarchi, G., De Vita, A., Kern, K. & Rust, H. . P. *J. Chem. Phys.* **120 (24)**, 11367 (2004).

[111] Rao, C. N. R., Natarajan, S. & Vaidhyanathan, R. *Angew. Chem., Int. Ed.* **43**, 1466 (2004).

[112] Klemm, D., Heublein, B., Fink, H. . P. & Bohn, A. *Angew. Chem., Int. Ed.* **44**, 3358 (2005).

[113] Kato, T., Mizoshita, N. & Kishimoto, K. *Angew. Chem., Int. Ed.* **45**, 38 (2006).

[114] Brammer, L. *Chem. Soc. Rev.* **33**, 476 (2004).

[115] Descalzo, A. B., Martínez-Mánez, R., Sancenón, F. F., Hoffmann, K. & Rurack, K. *Angew. Chem., Int. Ed.* **45**, 5924 (2006).

[116] Calzaferri, G., Huber, S., Maas, H. & Minkowski, C. *Angew. Chem., Int. Ed.* **42**, 3732 (2003).

[117] Furukawa, H. *et al.* *Science* **329**, 424 (2010).

[118] Meilikhov, M., Yusenko, K., Esken, D., Turner, S., van Tendeloo, G. & Fischer, R. A. *Eur. J. Inorg. Chem.* **2010**, 3701 (2010).

[119] Sumida, K. *et al.* *Chem. Rev.* **112**, 724 (2012).

[120] Yoon, M., Srirambalaji, R. & Kim, K. *Chem. Rev.* **112**, 1196 (2012).

[121] Shekhah, O., Liu, J., Fischer, R. A. & Wöll, C. *Chem. Soc. Rev.* **40**, 1081 (2011).

[122] Betard, A. & Fischer, R. A. *Chem. Rev.* **112**, 1055 (2012).

[123] Elemans, J. A. A. W., Lei, S. & De Feyter, S. *Angew. Chem., Int. Ed.* **48**, 7298 (2009).

[124] Madueno, R., Raisanen, M. T., Silien, C. & Buck, M. *Nature* **454**, 618 (2008).

[125] Decker, R. *et al.* *Appl. Phys. Lett.* **93**, 243102 (2008).

[126] Krenner, W., Klappenberger, F., Kuhne, D., Diller, K., Qu, Z. R., Ruben, M. & Barth, J. V. *J. Phys. Chem. Lett.* **2**, 1639 (2011).

[127] Kley, C. S., Cechal, J., Kumagai, T., Schramm, F., Ruben, M., Stepanow, S. & Kern, K. *J. Am. Chem. Soc.* **134**, 6072 (2012).

[128] Cokoja, C. R. B. H. W. A. K. F. E., M.; Bruckmeier. *Angew. Chem., Int. Ed.* **50**, 8510 (2011).

[129] Meyer, J. A., Baikie, I. D., Kopatzki, E. & Behm, R. J. *Surf. Sci.* **365**, L647 (1996).

[130] Hite, D. A., Kizilkaya, O., Sprunger, P. T., Howard, M. M., Ventrice, J. r., C. A., Geisler, H. & Zehner, D. M. *J. Vac. Sci. Technol. A* **18**, 1950 (2000).

[131] Caffio, M., Atrei, A., Bardi, U. & Rovida, G. *Surf. Sci.* **588**, 135 (2005).

[132] Yu, B. D. & Scheffer, M. *Phys. Rev. B* **55**, 13916 (1997).

[133] Langelaar, M. H. & Boerma, D. O. *Surf. Sci.* **395**, 131 (1998).

[134] Perkins, L. S. & DePristo, A. E. *Surf. Sci.* **319**, 225 (1994).

[135] Canepa, M., Terreni, S., Cantini, C., Campora, A. & Mattera, L. *Phys. Rev. B* **56**, 4233 (1997).

[136] Venables, J. A., Spiller, G. D. T. & Hanbucken, M. *Rep. Prog. Phys.* **47**, 399 (1984).

[137] Klettke, T., Walther, D., Schmidt, A., Gorls, H., Imhof, W. & Gunther, W. *Chem. Ber.* **129**, 1457 (1996).

[138] Braga, D. *et al.* *Organometallics* **16**, 4910 (1997).

[139] Hyla-Kryspin, I., Koch, J., Gleiter, R., Klettke, T. & Walther, D. *Organometallics* **17**, 4724 (1998).

[140] Walther, D., Dohler, T., Heubach, K., Klobes, O., Schweder, B. & Gorls, H. *Z. Anorg. Allg. Chem.* **625**, 923 (1999).

[141] Koch, J., Hyla-Kryspin, I., Gleiter, R., Klettke, T. & Walther, D. *Organometallics* **18**, 4942 (1999).

[142] Bonrath, W., Porschke, K. R., Wilke, G., Angermund, K. & Kruger, C. *Angew. Chem., Int. Ed. Engl.* **27**, 833 (1988).

[143] Rosenthal, U., Pulst, S., Kempe, R., Porschke, K. R., Goddard, R. & Proft, B. *Tetrahedron* **54**, 1277 (1998).

[144] Brune, H., Giovannini, M., Bromann, K. & Kern, K. *Nature (London)* **394**, 451 (1998).

[145] Schmid, M., Kresse, G., Buchsbaum, A., Napetschnig, E., Gritschneder, S., Reichling, M. & Varga, P. *Phys. Rev. Lett.* **99**, 196104 (2007).

[146] Becker, C. *et al.* *New J. Phys.* **4**, 75 (2002).

[147] N'Diaye, A. T., Bleikamp, S., Feibelman, P. J. & Michely, T. *Phys. Rev. Lett.* **97**, 215501 (2006).

[148] Chambliss, D. D., Wilson, R. J. & Chiang, S. *Phys. Rev. Lett.* **66**, 1721 (1991).

[149] Chambliss, D. D., Wilson, R. J. & Chiang, S. *J. Vac. Sci. Technol. B* **9**, 933 (1991).

[150] Cullen, W. G. & First, P. N. *Surf. Sci.* **420**, 53 (1999).

[151] Pandey, R., Rao, B. K., Jena, P. & Blanco, M. A. *J. Am. Chem. Soc.* **123**, 3799 (2001).

[152] BelBruno, J. J. *Surf. Sci.* **577**, 167 (2005).

[153] Grätzel, M. *Prog. Photovolt. Res. Appl.* **14**, 429 (2006).

[154] Yella, A. *et al. Science* **334**, 629 (2011).

[155] Watson, D. F. & Meyer, G. *J. Annu. Rev. Phys. Chem.* **56**, 119 (2005).

[156] Koops, S. E., O'Regan, B. C., Barnes, P. R. F. & Durrant, J. R. *J. Am. Chem. Soc.* **131**, 4808 (2009).

[157] Wu, J. *et al. Pure Appl. Chem.* **80**, 11 (2008).

[158] Grätzel, M. *Nature* **414**, 338 (2001).

[159] De Angelis, F., Fantacci, S., Selloni, A., Grätzel, M. & Nazeeruddin, M. K. *Nano Letters* **7 (10)**, 3189 (2007).

[160] Ding, X. Z., Liu, X. H. & He, Y. Z. *J. Mater. Sci. Lett.* **15**, 1789 (1996).

[161] Jamieson, J. & Olinger, B. *Miner. Notes* **54**, 1477 (1969).

[162] Gamboa, J. A. & Pasquevich, D. M. *J. Am. Ceram. Soc.* **75**, 2934 (1992).

[163] Pistorius, C. *Prog. Solid State Chem.* **II**, 1 (1976).

[164] Smith, S. J., Stevens, R., Liu, S., Li, G., Navrotsky, A., Boerio-Goates, J. & Woodfield, B. F. *Am. Miner.* **94**, 236 (2009).

[165] Ghosh, T. B., Dhabal, S. & Datta, A. K. *J. Appl. Phys.* **94**, 4577 (2003).

[166] Murray, J. L. & Wriedy, H. A. *Bull. Alloy Phase Diagr.* **8**, 148 (1987).

[167] Ertl, G. & Küppers, J. *Low Energy Electrons and Surface Chemistry.* (VHV-Wiley, Weinheim, 1985).

[168] Beltran, A., Gracia, L. & Andres, J. *J. Phys. Chem. B* **110**, 23417 (2006).

[169] Henrich, V. E. & Cox, P. A. *The Surface Science of Metal Oxides* (Cambridge University Press, Cambridge, 1994).

[170] Diebold, U., Ruzycki, N., Herman, G. S. & Selloni, A. *Catal. Today* **85**, 93 (2003).

[171] Hebenstreit, W., Ruzycki, N., Herman, G. S., Gao, Y. & Diebold, U. *Phys. Rev. B* **62**, 24 (2000).

[172] Herman, G. S., Dohnalek, Z., Ruzycki, N. & Diebold, U. *J. Phys. Chem. B* **107**, 2788 (2003).

[173] Liang, Y., Gan, S., Chambers, S. A. & Altman, E. I. *Phys. Rev. B* **63**, 235402 (2001).

[174] Thomas, A. G. *et al. Phys. Rev. B* **67**, 035110 (2003).

[175] Gong, X. . Q., Selloni, A., Batzill, M. & Diebold, U. *Nat. Mat.* **5**, 665 (2006).

[176] Walle, L., Borg, A., Johansson, E. M. J., Plogmaker, S., Rensmo, H., Uvdal, P. & Sandell, A. *J. Phys. Chem. C* **115**, 9545 (2011).

[177] Shklover, V. *et al. Chem. Mater.* **9**, 430 (1997).

[178] Lazzeri, M., Vittadini, A. & Selloni, A. *Phys. Rev. B* **63**, 155409 (2001).

[179] Oliver, P., Watson, G., Kelsey, E. & Parker, S. *J. Mater. Chem.* **73**, 56 (1997).

[180] Burdett, J. K., Hughbanks, T., Miller, G. J., Richardson, J. W. & Smith, J. V. *J. Am. Chem. Soc.* **109**, 3639 (1987).

[181] Wulff, G. *Zeitschrift für Krystallographie und Mineralogie* **34**, 449 (1901).

[182] Vittadini, A., Selloni, A., Rotzinger, F. P. & Grätzel, M. *Phys. Rev. Lett.* **81**, 2954 (1998).

[183] Ranade, M. R. *et al. Proc. Natl. Acad. Sci. USA* **99**, 6476 (2002).

[184] Hanaor, D. A. H. & Sorrell, C. C. *J. Mater. Sci.* **46**, 855 (2011).

[185] Herman, G. S., Gao, Y., Tran, T. T. & Osterwalder, J. *Surf. Sci.* **447**, 201 (1999).

[186] Herman, G. S. & Gao, Y. *Thin Solid Films* **397**, 157 (2001).

[187] Chambers, S. A., Wang, C. M., Thevuthasan, S., Droubay, T., McCready, D. E. & Lea, A. S. *Thin Solid Films* **418**, 197 (2002).

[188] Hengerer, R., Kavan, L. & Grätzel, M. *J. Electrochem. Soc.* **147**, 1467 (2000).

[189] Hengerer, R., Bolliger, B., Erbudak, M. & Grätzel, M. *Surf. Sci.* **460**, 162 (2000).

[190] Silversmit, G., Poelman, H., Fiermans, L. & De Gryse, R. *Solid State Commun.* **119**, 101 (2001).

[191] Beck, D., White, J. & Ratcliffe, C. *J. Phys. Chem.* **90**, 3123 (1986).

[192] Sanjines, R., Tang, H., Berger, H., Schmid, P. & Levy, F. *J. Appl. Phys.* **75**, 2945 (1994).

[193] Maruska, H. P. & Gosh, A. K. *Sol. Energy* **20**, 443 (1978).

[194] Deacon, G. B. & Phillips, R. J. *Coordin. Chem. Rev.* **33**, 227 (1980).

[195] Nazeeruddin, M. K., Humphry-Baker, R., Liska, P. & Grätzel, M. *J. Phys. Chem. B* **107**, 8981 (2003).

[196] Guo, Q., Cocks, I. & Williams, E. M. *J. Chem. Phys* **106**, 2924 (1997).

[197] Bates, S. P., Kresse, G. & Gillan, M. J. *Surf. Sci.* **409**, 336 (1998).

[198] Li, M., Hebenstreit, W., Diebold, U., Tyryshkin, A. M., Bowman, M. K., Dunham, G. C. & Henderson, M. A. *J. Phys. Chem. B* **104**, 4944 (2000).

[199] Pan, J. M., Maschhoff, B. L., Diebold, U. & Madey, T. E. *J. Vac. Sci. Technol. A* **10**, 2470 (1992).

[200] Hugenschmidt, M. B., Gamble, L. & Campbell, C. T. *Surf. Sci.* **302**, 329 (1994).

[201] Hebenstreit, E. L. D. *et al.* *Phys. Rev. B* **64**, 115418 (2001).

[202] Kurtz, R. L., Stockbauer, R., Madey, T. E., Roman, E. & de Segovia, J. L. *Surf. Sci.* **218**, 178 (1989).

[203] Epling, W. S., Peden, C. H. F., Henderson, M. A. & Diebold, U. *Surf. Sci.* **412/413**, 333 (1998).

[204] A., H. M., Epling, W. S., Perkins, C. L., Peden, C. H. F. & Diebold, U. *J. Phys. Chem. B* **103**, 5328 (1999).

[205] Scheiber, P. *et al.* *Phys. Rev. Lett.* **109**, 136103 (2012).

[206] Henderson, M. A. *Surf. Sci.* **419**, 174 (1999).

[207] Warschkow, O., Wang, Y., Subramanian, A., Asta, M. & Marks, L. D. *Phys.*

Rev. Lett. **100**, 086102 (2008).

[208] Thomas, A. G. *et al. Phys. Rev. B* **75**, 035105 (2007).

[209] Cheng, H. & Selloni, A. *J. Chem. Phys.* **131**, 054703 (2009).

[210] He, Y., Dulub, O., Cheng, H., Selloni, A. & Diebold, U. *Phys. Rev. Lett.* **102**, 106105 (2009).

[211] Murakoshi, K., Kano, G., Wada, Y., Yanagida, S., Miyazaki, H., Matsumoto, M. & Murasawa, S. *J. Electroanal. Chem.* **396**, 27 (1995).

[212] Mann, J. R., Gannon, M. K., Fitzgibbons, T. C., Detty, M. R. & Watson, D. F. *J. Phys. Chem. C* **112**, 13057 (2008).

[213] Patrick, C. E. & Giustino, F. *Phys. Rev. B* **84**, 085330 (2011).

[214] Hugot-Le Goff, A. & Falaras, P. *J. Electrochem. Soc.* **142**, 38 (1995).

[215] Falaras, P., Grätzel, M., Hugot-Le Goff, A., Nazeeruddin, M. & Vrachnou, E. *J. Electrochem. Soc.* **140**, 92 (1993).

[216] Haukka, M. & Hirva, P. *Surf. Sci.* **511**, 373 (2002).

[217] Sasahara, A., Pang, C. L. & Onishi, H. *J. Phys. Chem. B* **110**, 4751 (2006).

[218] Sasahara, A., Fujio, K., Koide, N., Han, L. & Onishi, H. *Surf. Sci.* **604**, 106 (2010).

[219] Mayor, L. C., Taylor, J. B., Magnano, G., Rienzo, A., Satterley, C. J., O'Shea, J. N. & Schnadt, J. *J. Chem. Phys.* **129**, 114701 (2008).

[220] Finnie, K. S., Bartlett, J. R. & Woolfrey, J. L. *Langmuir* **14**, 2744 (1998).

[221] Rensmo, H., Westermark, K., Södergren, S., Kohle, O. & Persson, P. *J. Chem. Phys.* **111**, 2744 (1999).

[222] Shklover, V., Ovchinnikov, Y. E., Braginsky, L. S., Zakeeruddin, S. M. & Grätzel, M. *Chem. Mater.* **10**, 2533 (1998).

[223] Pastore, M. & De Angelis, F. *J. Phys. Chem. Lett.* **4**, 956 (2013).

[224] Gebhardt, C. R., Tomsic, A., Schröder, H., Dürr, M. & Kompa, K. L. *Angew. Chem. Int. Ed.* **48**, 4162 (2009).

[225] Wysocki, V. H., Joyce, K. E., Jones, C. M. & Beardsley, R. L. *J. Am. Soc. Mass. Spectrom.* **19**, 190 (2008).

[226] Bier, M., Amy, J., Cooks, R., Syka, J., Ceja, P. & Stafford, G. *Int. J. Mass Spectrom. Ion Processes* **77**, 31 (1987).

[227] Watkins, M., Trevethan, T., Sushko, M. L. & Shluger, A. L. *J. Phys. Chem. C* **112**, 4226 (2008).

[228] Vanderbilt, D. *Phys. Rev. B* **41**, 7892 (1990).

[229] Giannozzi, P. *et al.* *Journal of Physics: Condensed Matter* **21**, 395502 (2009).

[230] Martyna, G. J. & Tuckerman, M. E. *J. Chem. Phys.* **110**, 2810 (1999).

[231] Schiffmann, F., VandeVondele, J., Hutter, J., Wirz, R., Urakawa, A. & Baiker, A. *J. Phys. Chem. C* **114**, 8398 (2010).

[232] Galoppini, E. *Coord. Chem. Rev* **248**, 1283 (2004).

[233] Hagfeldt, A. & Grätzel, M. *Acc. Chem. Res.* **33**, 269 (2000).

[234] Johansson, E. M. J., Hedlund, M., Odelius, M., Siegbahn, H. & Rensmo, H. *J. Chem. Phys.* **126**, 244303 (2007).

[235] Schnadt, J. *et al.* *Nature* **418**, 620 (2002).

[236] Labat, F. & Adamo, C. *J. Phys. Chem. C* **111**, 15034 (2007).

[237] Patthey, L. *et al.* *J. Chem. Phys.* **110**, 5913 (1999).

[238] Schnadt, J. *et al.* *J. Chem. Phys.* **119**, 23 (2003).

[239] Persson, P., Lunell, S., Brúhwiler, P. A., Schnadt, J. & Sódergren, S. *J. Chem. Phys.* **112**, 3945 (2000).

[240] Odelius, M., Persson, P. & Lunell, S. *Surf. Sci.* **527**, 47 (2003).

[241] Schnadt, J. *et al.* *J. Phys. Chem. B* **108**, 3114 (2004).

[242] Persson, P. & Lunnell, S. *Solar Energy Materials & Solar Cells* **63**, 139 (2000).

[243] Jug, K. & Bredow, T. *J. Comput. Chem.* **25**, 1551 (2004).

[244] Thomas, A. G. *et al.* *Surf. Sci.* **592**, 159 (2005).

[245] O'Shea, J. N. *et al.* *J. Phys. Chem. B* **105 (10)**, 1917 (2001).

[246] McFarland, E. W. & Tang, J. *Nature* **421**, 616 (2003).

[247] Mayor, L. C., Saywell, A., Magnano, G., Satterley, C. J., Schnadt, J. & O'Shea, J. N. *J. Chem. Phys.* **130**, 164704 (2009).

[248] Qiu, X. H., Nazin, G. V. & Ho, W. *Phys. Rev. Lett.* **92**, 206102 (2004).

[249] Hugot-Le Goff, A., Joiret, S. & Falaras, P. *J. Phys. Chem. B* **103**, 9569 (1999).

[250] Britton, A. J., Weston, M., Taylor, J. B., Rienzo, A., Mayor, L. C. & O'Shea, J. N. *J. Chem. Phys.* **135**, 164702 (2011).

[251] Repp, J. & Meyer, G. *Appl. Phys. A* **85**, 399 (2006).

[252] Kondo, J. *Progr. of Theor. Phys.* **32**, 37 (1964).

[253] Goldhaber-Gordon, D., Shtrikman, H., Mahalu, D., Abusch-Magder, D., Meirav, U. & Kastner, M. A. *Nature* **391**, 156 (1998).

[254] Madhavan, V., Chen, W., Jamneala, T., Crommie, M. F. & Wingreen, N. S. *Science* **280**, 567 (1998).

[255] Jarillo-Herrero, P., Kong, J., van der Zant, H. S. J., Dekker, C., Kouwenhoven, L. P. & De Franceschi, S. *Nature* **434**, 484 (2005).

[256] Parks, J. J., Champagne, A. R., Hutchison, G. R., Flores-Torres, S., Abruña, H. D. & Ralph, D. C. *Phys. Rev. Lett.* **99**, 026601 (2007).

[257] Knorr, N., Schneider, M. A., Diekhöner, L., Wahl, P. & Kern, K. *Phys. Rev. Lett.* **88**, 096804 (2002).

[258] Wahl, P., Diekhöner, L., Wittich, G., Vitali, L., Schneider, M. A. & Kern, K. *Phys. Rev. Lett.* **95**, 166601 (2005).

[259] Cheianov, V. V. *Eur. Phys. J. Special Topics* **148**, 55 (2007).

[260] Kanao, T., Matsuura, H. & Ogata, M. *J. of the Phys. Soc. of Japan* **81**, 063709 (2012).

[261] Cornaglia, P. S., Usaj, G. & Balseiro, C. A. *Phys. Rev. Lett.* **102**, 046801 (2009).

[262] Brar, V. W. *et al.* *Nat Phys* **7**, 43 (2011).

[263] Ruderman, M. A. & Kittel, C. *Phys. Rev.* **96**, 99 (1954).

[264] Dugaev, V. K., Litvinov, V. I. & Barnas, J. *Phys. Rev. B* **74**, 224438 (2006).

Acknowledgements

I would like to express my gratitude to Prof. Klaus Kern for giving me the opportunity to work in his research group. I highly appreciate his unrestricted and permanent support in all respects as well as the freedom he gave me for the research topic.

My highest gratitude goes to my supervisor Sebastian Stepanow. His broad and deep scientific knowledge combined with his guidance and continuous support provided me an ideal environment for accomplishing this thesis.

I am sincerely grateful to Prof. Michael Grätzel for stimulating discussions. I thank Prof. Romuald Houdré, Prof. Anna Fontcuberta I Morral, Prof. Harold Zandvliet and Prof. James O'Shea for being part of my PhD jury.

Special thanks to Jan Cechal, Christian Dette and Soon-Jung Jung for the time we spent together at the G-STM. I would like to thank Alexander Langner, Nasiba Abdurakhmanova and Tzu-Chun Tseng for introducing me into the world of scanning tunneling microscopy and supramolecular chemistry.

I am sincerely grateful to the ESI team Stephan Rauschenbach and Gordon Rinke. Their exceptional technique and permanent support made a major part of this thesis possible. Special gratitude goes to Gordon for the countless hours we spent together in the lab, office and outside the institute from which a deep friendship has evolved. Also thanks to Hannah Ochner for her support in many respects.

I would further like to acknowledge Frank Schramm and Mario Ruben for providing organic ligands as well as Christopher Patrick and Feliciano Giustino for performing theoretical simulations and our collaboration.

A great deal of help during the construction of the new STM was provided from our technicians Wolfgang Stiepany, Peter Andler and Andreas Koch as well as from the mechanical workshop where I particularly want to thank Thomas Frey, Werner

Bulling and Hermann Beer for their always fast help. Peter Droste (SurfaceNet GmbH) deserves thanks for providing me always very promptly with high-quality TiO_2 crystals.

I enjoyed the nice atmosphere in our department for which I thank all people working in Prof. Klaus Kern's group. I would like to thank my present and former office-mates Gordon Rinke, Rico Gutzler, Theresa Lutz, Nasiba Abdurakhmanova and Alexander Langner for the pleasant time we spent together. Special thanks goes to Eike Schäfer-Nolte, Tobias Herden, Carola Strasser, Sebastian Stepanow, Max Assig, Gordon Rinke, Christian Dette, Doris Grumelli, Sören Krotzky, Benjamin Wurster, Christoph Grosse and Sabine Abb - it was a pleasure to work and spend the spare time with you.

Especially very much I owe to my parents Noriko and Josef Kley and my brother Simon for their unflagging support in all respects. Finally I thank you - Judith - for your unconditional support, motivation and love which made this work possible.

Curriculum Vitae

Personal

Name	Christopher Seiji Kley
Date of Birth	June 14, 1983
Place of Birth	Tokyo, Japan
Nationality	German

Background

2009 - 2013	**Ph.D. in Physics** École Polytechnique Fédérale de Lausanne, Switzerland Max Planck Institute for Solid State Research, Germany *"Atomic-scale characterization and control of metal-organic templates and photosensitizers on surfaces"* Directed by Prof. Dr. Klaus Kern
2008 - 2009	**Diploma thesis** Max Planck Institute for Chemical Energy Conversion, Germany *"Femtosecond dynamics of energy and electron transfer in PS II"* Directed by Prof. Dr. Alfred Holzwarth
2003 - 2008	**Diploma studies in physics** Karlsruhe Institute of Technology, Germany
2002 - 2003	**Compulsory military service** 6. Instandsetzungsbataillon 210, Stetten a.k.M., Germany
1993 - 2002	**High School** Hebel-Gymnasium, Pforzheim, Germany

External conferences and seminars (during Ph.D.)

02/2013	DPG Spring Meeting, Regensburg, GER (talk) *"Multi-conformational binding of Ruthenium-based Photosensitizer on* TiO_2 *anatase (101)"*
04/2012	Caltech, Prof. Nathan Lewis, USA (talk) *"Steps towards artificial photosynthesis"*
04/2012	MRS Spring Meeting, San Francisco, USA (talk) *"Studying the N3 dye adsorption on* TiO_2 *anatase (101) at a molecular and supramolecular level"*
03/2011	DPG Spring Meeting, Dresden, GER (poster) *"Rational design of two-dimensional metal-organic frameworks for functional catalysis"*
10/2010	EPFL, Prof. Michael Grätzel, CH (talk) *"From photosynthetic units to artificial solar-to-fuel systems"*
10/2010	X International Conf. on Nanostr. Mater., Rome, IT (poster) *"Rational Design of two-dimensional metal-organic frameworks"*
09/2010	KFN Meeting, Bad Herrenalb, GER (talk) *"Adaptive Nanostrukturen durch hierarchische Selbstorganisation"*
08/2010	15th International Congress of Photosynthesis, Beijing, CN (n.c.)

Publications

- **C. S. Kley**, J. Cechal, T. Kumagai, F. Schramm, M. Ruben, S. Stepanow, K. Kern, "Highly adaptable two-dimensional metal-organic coordination networks on metal surfaces", *J. Am. Chem. Soc.* **134**, 6072 (2012)
- N. Abdurakhmanova, T.-C. Tseng, A. Langner, **C. S. Kley**, V. Sessi, S. Stepanow, K. Kern, "Superexchange-mediated ferromagnetic coupling in two-dimensional Ni-TCNQ networks on metal surfaces", *Phys. Rev. Lett.* **110**, 27202 (2013)
- J. Cechal, **C. S. Kley**, T. Kumagai, F. Schramm, M. Ruben, S. Stepanow, K. Kern, "Functionalization of open two-dimensional metal-organic templates through the selective incorporation of metal atoms", *J. Phys. Chem. C*, **117**, 8871 (2013)
- **C. S. Kley**, C. Dette, G. Rinke, J. Cechal, C. Patrick, S.-J. Jung, S. Rauschenbach, F. Giustino, S. Stepanow, K. Kern, "Multi-conformational binding of ruthenium-based photosensitizer on TiO_2 anatase (101)", *submitted*
- **C. S. Kley**, C. Dette, C. Patrick, J. Cechal, S.-J. Jung, F. Giustino, S. Stepanow, K. Kern, "Structural and electronic properties of the photosensitizer anchoring ligand BINA on TiO_2 anatase (101)", *in preparation*
- **C. S. Kley**, J. Cechal, F. Schramm, M. Ruben, S. Stepanow, K. Kern, "Strong molecular relaxations of a rod-like benzoic acid ligand on metal surfaces", *in preparation*
- **C. S. Kley**, J. Cechal, F. Schramm, M. Ruben, S. Stepanow, K. Kern, "Studying CO_2 activation by organic molecules on metal surfaces", *in preparation*
- N. Abdurakhmanova, T.-C. Tseng, A. Langner, **C. S. Kley**, V. Sessi, S. Stepanow, K. Kern, "Ferromagnetism in two-dimensional charge transfer networks on metal surfaces", *in preparation*